LBL--20682

DE86 006716

An Inverse Problem for *in vivo* NMR Spatial Localization

Andrew Craig Hasenfeld

(Ph.D. Thesis)

Biology and Medicine Division, Lawrence Berkeley Laboratory,
and Department of Physics,
University of California,
Berkeley, California 94720

An Inverse Problem for *in vivo* NMR Spatial Localization

Andrew Craig Hasenfeld

Biology and Medicine Division, Lawrence Berkeley Laboratory,
and Department of Physics,
University of California,
Berkeley, California 94720

Abstract

The basic physical problem of NMR spatial localization is considered. A practical use of NMR in biomedicine is the *in vivo* spectroscopic study of various "biological" nuclei located in diseased tissues in the body. In order to quantitatively study these diseased sites, one must first solve the problem of adequately localizing the NMR signal at the diseased region of interest. We formulate this as an inverse problem, in which the achievement of localized excited spin populations is the "known" goal, and one seeks to "invert" these data to find the appropriate magnetic field configurations to yield this desired result.

As the NMR Bloch equations determine the motion of nuclear spins in applied magnetic fields, a theoretical study is undertaken to answer the question of how to design magnetic field configurations to achieve these localized excited spin populations. Because of physical

constraints in the production of the relevant radiofrequency fields, the problem factors into a temporal one and a spatial one.

We formulate the temporal problem as a nonlinear transformation, called the Bloch Transform, from the rf input to the magnetization response. In trying to invert this transformation, both linear (for the Fourier Transform) and nonlinear (for the Bloch Transform) modes of radiofrequency excitation are constructed. The spatial problem is essentially a statics problem for the Maxwell equations of electromagnetism, as the wavelenths of the radiation considered are on the order of ten meters, and so propagation effects are negligible. In the general case, analytic solutions are unavailable, and so the methods of computer simulation are used to map the rf field spatial profiles.

Numerical experiments are also performed to verify the theoretical analysis, and experimental confirmation of the theory is carried out on the 0.5 Tesla IBM/Oxford Imaging Spectrometer at the LBL NMR Medical Imaging Facility. While no explicit inverse is constructed to "solve" this problem, the combined theoretical/numerical analysis is validated experimentally, justifying the approximations made.

Table of Contents

1. **Introduction**.....1

2. **The Medical Imaging Bloch Equations (MIBE)**.....6

(a) An application of NMR to biomedical imaging.....6

(b) The (relevant) theory of the rotation group.....13

(c) Phase modulation is frequency modulation.....16

3. **Slepian-Hasenfeld-rotation group-pulses (SHARP)**.....19

(a) The "time/band limited" problem.....19

(b) The Bloch Transform.....22

(c) Modulations.....24

(d) A geometric picture of the Fourier Transform.....31

(e) On gaussian pulses.....32

4. **Inhomogeneous rf Fields**.....36

(a) Basic physics according to Maxwell.....36

(b) Coils.....39

(c) Pulse sequences.....40

(d) B_1 and ΔB_o together.....45

5. Experiments.....52

(a) Numerical simulations.....52

(b) NMR phantom measurements.....58

(c) Two theorems.....66

6. Is the Bloch Tranform Invertible?.....70

(a) Motivation.....70

(b) The inverse scattering transform.....72

(c) Reformulating the Bloch Transform as a scattering problem.....75

(d) 2πN-solitons.....78

(e) On a connection between the Bloch Equations and the KdV equation.....85

(f) (Soliton) reflections.....102

7. Conclusion.....106

8. References.....110

To Mother Nature, Respectfully

Acknowledgments

First and foremost, to my advisor and friend, Alberto Grünbaum, for his inspired guidance, and the gift of a religion without guilt.

To Dr. T.F. Budinger, for posing a very practical, real world problem, and for supporting me in this research, and to each and every one of his Research Medicine Group (most notably Mark Roos for NMR expertise, Ron Huesman for computer mastery, and those unsung heroes Eva and Katherine), for providing the playful yet productive atmosphere in which this work was carried out.

To physicists:

- Eyvind Wichmann, for such visionary lessons on the rotation group, and for granting me the time and space to convince myself that quantum field theory isn't "everything",
- Erwin Hahn, Mel Klein, and other Berkeley NMR wizards, for sharing some of their insights into that mysterious world of nuclear spins,
- Gene Commins, for being Gene Commins,
- Charlie Schwartz, for his relentless concern on issues of moral principle,
- and my fellow graduate student collegues Glenn, Fred, and others, for sharing the struggle that is graduate physics at Berkeley.

1. Introduction

"The goal to be put above everything else is an open world where each nation can assert itself solely by the extent to which it can contribute to the common culture and help others with experience and resources."

N. Bohr

An important problem in NMR medical imaging, now that the first generation of machines has proven so successful, is to extend the diagnostic value of NMR in medicine to *in vivo* spectroscopic studies. A prerequisite to quantitative selective region NMR spectroscopy is the achievement of reasonable spatial localization. We consider, as a model, a patient with a small tumor deep inside his parietal cortex (Figure 1.1). The medical community would like to use NMR not only to locate the site of the diseased tissue, but also, using spectroscopic techniques, to infer the severity of the diseased state (by perhaps studying the time course of the tissue metabolism). In order to successfully apply NMR imaging methods in this case, we must first solve the problem of knowing that the NMR signal we detect really comes from the region we wish to study.

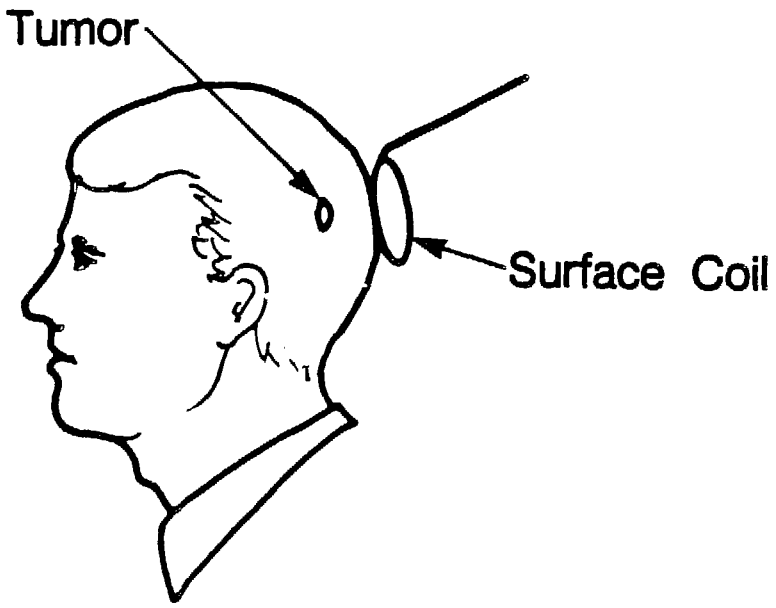

Figure 1.1:

Surface coil measurement of a brain tumor.

The quantum mechanical nature of NMR is most evident in the microscopic description of nuclear magnetic moments (spin angular momentum). It is these moments in the patient's brain tumor we wish to excite, while leaving the spins outside the region of interest at equilibrium. Thus, the problem of spatial localization in NMR comes down ultimately to the basic question: What are the nuclear spins doing?

To answer this question, we must consider the Bloch equations, a set of three coupled first order ordinary differential equations (ODE) written down by Felix Bloch in 1946[1]. These equations phenomenologically describe the motion of a magnetization vector M,

a macroscopic sum of these elementary nuclear spin moments, under applied magnetic fields. In the context of present-day NMR medical imaging equipment, we can therefore consider what possible magnetic field configurations will produce for us, in solving the Bloch equations, the desired localized excited spin populations.

As we have now stated the problem in basic physical terms, it is appropriate to consider a clever solution to a problem of a similar kind, which enabled the development of NMR biomedical image formation to begin in earnest. This problem is the one of selecting a two-dimensional planar surface through the patient in which to perform imaging experiments, and is usually referred to as the problem of slice selection (or selective excitation). A truncated $\pi/2$ sinc amplitude modulated rf pulse in the presence of a main field gradient is the well-known solution[2], and it serves well as point of departure for the present investigation.

The two assumptions made in "solving" that problem, that

(1) although the sinc function lives on the line R and not an interval [-T,T],
the tails of the sinc don't matter much

and that

(2) for a $\pi/2$ pulse in a main field gradient, solving the Bloch equations is
basically equivalent to performing a Fourier Transform[3]

are removed in this analysis. Not only does this lead to a solution of the problem for π

pulses, but in fact leads to a clear formulation of the problem in full generality. Loosely speaking, we can phrase the problem in the following way:

Is it physically possible, in a given time t_p
(experimentally on the order of a few milliseconds) to achieve any desired
final configuration of spins as a function of the relevant field strengths?

The field strengths considered are the "standard" ones of current NMR biomedical imagers, namely linear main field gradients and the rf coil field.

The ways out of (1) and (2) above both require rigourous mathematical care, but both are too "pretty" not to comment. The use of prolate spheroidal wave functions as rf field modulations is, on the one hand, just another example that demonstrates their tremendous versatility and practical importance[4]. On the other hand, as in (2), the Bloch equations are not the Fourier Transform, and their utility in this nonlinear analogue is somewhat puzzling. Likewise, the use of the rotation group, while not surprising if one accepts the Bloch equations, still poses some deep questions about symmetry and natural phenomena.

A second consideration in Figure 1.1 is the use of surface coils as rf field generators. While such coils provide a gross, first order spatial localization to the region of interest, there are also problems with such coils. In particular, in reference to the rf field contours from which one excites the spins, they are not only stronger near the coil, but also close back on the coil. Thus measurements resulting from the use of these coils are contaminated by significant surface skin and subcutaneous tissue, and so quantitative *in vivo* spectroscopy

suffers as a result. Ideally (i.e., neglecting S/N considerations), we would like to excite only nuclei at the diseased site, so that the use of localized coils clearly must be combined with other techniques, if we are to reasonably attain our goal.

The structure of our approach is now clear: after a brief description of the Bloch equations (suitably adapted for medical NMR), we treat both the problems of main field strength linear inhomogeneity and rf field strength inhomogeneity from theoretical and numerical points of view, keeping in mind that we "know" what final configurations for the *in vivo* spin populations are needed, and we wish to design the magnetic fields both temporally and spatially to achieve these goals. After constructing two set of linear modes of rf excitation, an exploration of a full answer to the question asked above will lead to the discovery of true "nonlinear modes of rf excitation" with remarkable properties. Finally, the results are then experimentally verified at the LBL NMR Medical Imaging Facility.

2. The Medical Imaging Bloch Equations (MIBE)

2(a) An application of NMR to biomedical imaging

"Profundity is the next word after the Torah."
E.L. Hahn

We are concerned with the Bloch equations in the context of medical imaging. Since we desire to only prepare localized excited spin populations for imaging/spectroscopic experiments, we shall not be concerned with the relaxation parameters T_1 and T_2. We justify neglecting these relaxation parameters on two grounds: the time required to exite the spins in the region of interest had better not take too much time, as we then wish to perform imaging and spectroscopic measurements (and so still want to have enough of a signal left to do so). The second reason is one of mathematical expediency: by neglecting the relaxation parameters, the orbit of the undamped precesing magnetization lies on the

surface of the unit sphere S^2 in R^3, and so precession can be described by rotation group operators. We therefore specifically address the physical problem of how (in theory and practice) to excite only those spins in the spatial region of interest.

We begin with a brief derivation, from quantum mechanical first principles, of the Bloch equations of NMR, as written down by Felix Bloch in 1946[1] in the component form:

$$\begin{aligned} \dot{M}_x(t,\mathbf{x}) &= \gamma(M_y\, B_z \;-\; M_z\, B_y) \;-\; \tfrac{M_x}{T_2} \\ \dot{M}_y(t,\mathbf{x}) &= \gamma(M_z\, B_x \;-\; M_x\, B_z) \;-\; \tfrac{M_y}{T_2} \\ \dot{M}_z(t,\mathbf{x}) &= \gamma(M_x\, B_y \;-\; M_y\, B_x) \;+\; \tfrac{M_0 - M_z}{T_1} \end{aligned} \tag{2.1}$$

Our derivation will recover the undamped motion of M, as the relaxation phenomena are irreversible, and thus not explicable in terms of a Hamiltonian describing free, noninteracting spins. This derivation is of interest for two reasons:

1. The behavior of nuclear spins in applied magnetic fields is indeed governed by the laws of quantum mechanics.
2. The rotation group plays a central role.

The classical energy E of a magnetic moment μ in a magnetic field B is

$$E \;=\; -\mu \cdot \mathbf{B} \tag{2.2}$$

The quantum mechanical treatment of spin angular momentum[5,6] begins with a similar Hamiltonian

$$\mathcal{H} \;=\; -\mu \cdot \mathbf{B} \tag{2.3}$$

but where $\mathcal{H}$ and μ are now operators and $\mathbf{B}$ is the scalar magnetic field.

In computing the time rate of change of the expectation value of the spin magnetic moment

$$< \mu > = \int \psi^* \, \mu \, \psi \tag{2.4}$$

we use the fact that ψ satisfies the Schrödinger equation

$$i\hbar\dot{\psi} \;=\; \mathcal{H}\psi \;=\; (-\mu \cdot \mathbf{B})\psi \tag{2.5}$$

so that ψ^* satisfies

$$-\, i\hbar\dot{\psi^*} \;=\; \psi^*\mathcal{H} \;=\; \psi^*(-\mu \cdot \mathbf{B}) \tag{2.6}$$

We thus compute (using (2.5) and (2.6))

$$\begin{aligned} < \dot{\mu} > &= \int \dot{\psi^*} \, \mu \, \psi \, + \, \int \psi^* \, \mu \, \dot{\psi} \\ &= \tfrac{1}{i\hbar} \int \psi^* \, [(\mu \cdot \mathbf{B})\mu \, - \, \mu(\mu \cdot \mathbf{B})]\psi \end{aligned} \tag{2.7}$$

But the spin magnetic moment μ is proportional to the angular momentum $\mathbf{J}$

$$\mu \;=\; \gamma \mathbf{J} \;=\; \gamma\hbar\mathbf{I} \tag{2.8}$$

(γ is the gyromagnetic ratio). The dimensionless angular momentum operators $\mathbf{I}$ generate the rotation group SO(3), and so satisfy the commutation relations

$$[I_x, I_y] \;=\; iI_z \quad (cyclic) \tag{2.9}$$

In this way, the calculation for the components (say μ_z) in (2.7) becomes

$$\begin{aligned} <\dot{\mu_z}> &= \tfrac{1}{i\hbar}\int \psi^* \, [\mu \cdot \mathbf{B}, \mu_z] \, \psi \\ &= \tfrac{-1}{i\hbar}\int \psi^* \, ([\mu_z, \mu_z]B_z \, + \, [\mu_z, \mu_y]B_y) \, \psi \\ &= \tfrac{-\gamma\hbar}{i\hbar}\int \psi^* \, (iB_z\mu_y \, - \, iB_y\mu_z) \, \psi \\ &= \gamma <\mu \, \times \, \mathbf{B}>_z \end{aligned} \tag{2.10}$$

This equation has precisely the same form as the Bloch equations (2.1) (neglecting relaxation), when we realize that the bulk magnetization **M** is realy just a "sum" of these small moments

$$\mathbf{M} \, = \frac{1}{N}\sum_{i=1}^{N} (\mu^+ \, - \, \mu^-) \tag{2.11}$$

where N is the total number of nuclei, and (μ^+, μ^-) are the number in the (ground, excited) states, respectively.

A brief historical comment is relevant here. By neglecting the relaxation parameters T_1 and T_2, the undamped Bloch equations are really Euler's equations[7] going back at least to the 1770's, and so our tradition of calling them the Bloch equations is somewhat of a misnomer. That is not to slight Felix Bloch; but his principal contribution in 1946 in developing these equations was precisely to describe the exponential decay of the NMR signal observed. It is more our analysis, in neglecting T_1 and T_2 (and so describing the evolution in terms of rotation operators), that is to blame.

While the basic magnetic field configuration of a large DC z-field B_o and an oscillating rf x-y plane field B_1 are standard components of an NMR medical imaging system[8],

there are two principal differences in medical NMR compared to the usual experimental configurations. The first is the imposition of linear gradients G in the large DC field B_o. The second difference is in the use of specially designed rf coils to produce B_1 fields with spatial inhomogeneity (we shall soon describe their purpose). We illustrate this experimental arrangement in Figure 2.1.

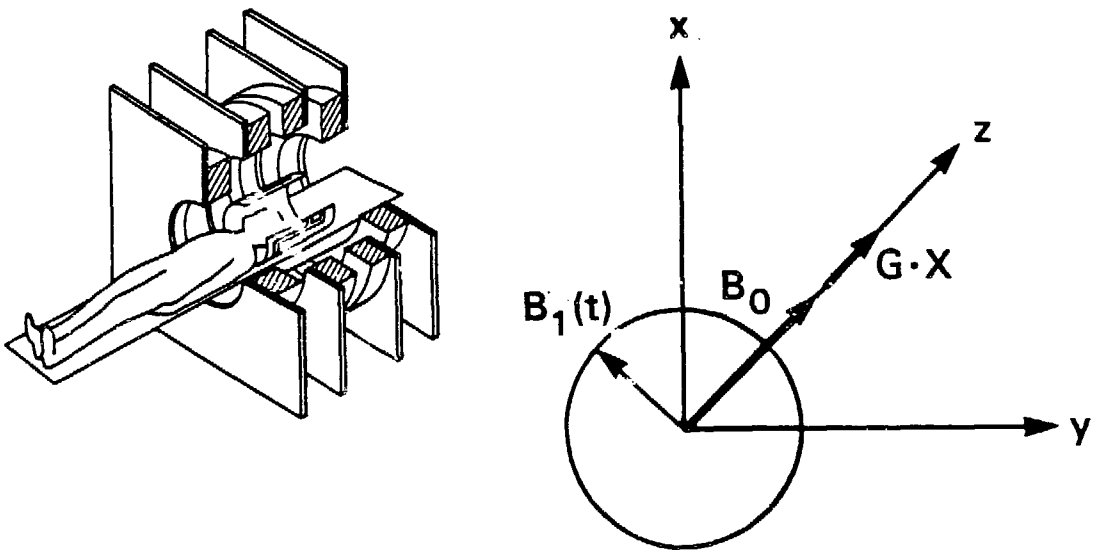

Figure 2.1:

Experimental configuration of the biomedical NMR experiment.

Therefore, from the Bloch equations (2.1), we make the modifications as follows. In addition to neglecting the relaxation terms T_1 and T_2 in (2.1), we consider a total applied field **B** of the form

$$\mathbf{B} = (B_o + \mathbf{G}\cdot\mathbf{x})\,\hat{z} + B_1(t,\mathbf{x})\,[\cos(\omega t + \phi(t))\hat{x} + \sin(\omega t + \phi(t))\,\hat{y}] \qquad (2.12)$$

(for $\mathbf{x} \in \mathrm{R}^3$) to reflect the imposition of linear gradients and the spatial modification of the rf field, assuming B_1 to be a slowly varying function of time t.

We briefly remark that the laboratory to rotating reference frame transformation[9] is equivalent to the change of variables[10]

$$\begin{aligned} M_x &= m_x \cos \omega t \; - \; m_y \sin \omega t \\ M_y &= m_x \sin \omega t \; + \; m_y \cos \omega t \end{aligned} \tag{2.13}$$

bringing us from the lab to our preferred rotating frame picture, where now the magnetic field has the form

$$\gamma \mathbf{B} \; = \; (\omega \; - \; \omega_o \; + \; \gamma \mathbf{G} \cdot \mathbf{x}) \; \hat{z} \; + \; \omega_1 \; [\cos \phi \; \hat{x} \; + \; \sin \phi \; \hat{y}] \tag{2.14}$$

and $\omega_1 = \gamma B_1$. With these modifications, and the imposition of the resonance condition ($\omega = -\gamma B_o \equiv \omega_o$), the medical imaging Bloch equations (MIBE) are written

$$\dot{\mathbf{M}} \; = \; \mathbf{M} \; \times \; \gamma \mathbf{B} \; \equiv \; \mathbf{A} \; \mathbf{M} \tag{2.15}$$

or, in components,

$$\frac{d}{dt} \begin{pmatrix} M_x \\ M_y \\ M_z \end{pmatrix} = \begin{pmatrix} 0 & \Delta\omega & -\omega_1 \sin \phi \\ -\Delta\omega & 0 & \omega_1 \cos \phi \\ \omega_1 \sin \phi & -\omega_1 \cos \phi & 0 \end{pmatrix} \begin{pmatrix} M_x \\ M_y \\ M_z \end{pmatrix} \tag{2.16}$$

where $\Delta\omega = \gamma \mathbf{G} \cdot \mathbf{x}$ is the frequency offset. What makes this set of equations not trivially solvable is the fact that the matrices in (2.16) do not commute except in special cases, such as the following.

We now explain the purpose of linear gradients in the main field B_o. If we consider the application of only the static z field B_o, we solve the Bloch equations (2.1) in this trivial case (neglecting relaxation) as

$$\begin{aligned} M_x(t) &= M_x^o \cos \omega_o t - M_y^o \sin \omega_o t \\ M_y(t) &= M_x^o \sin \omega_o t + M_y^o \cos \omega_o t \\ M_z(t) &= M_z^o \end{aligned} \tag{2.17}$$

We see therefore that the magnetization $\mathbf{M}$ precesses at the angular frequency $\omega_o \equiv -\gamma B_o$, so that frequency of precession is proportional to applied field strength. The application of linear gradients in B_o allows for spatial differentiation by the proportionality of distance to field (along the applied gradient direction), and thus to frequency. One is then able to determine the relative quantity of spins at a given position by examining the signal strength at the appropriate frequency.

The effect of inhomogeneous B_1 fields is best visualized in the case of the on-resonance rotating frame for a constant amplitude B_1 field (i.e., (2.16) with $\Delta\omega = \phi$=0 and $\omega_1(t) \equiv \omega_1$), another case that is trivially solved. The magnetization vector rotates in the y-z plane about the x-axis effective field B_1, and the total accumulated phase (flip angle) in a time t_o is just $\omega_1 t_o$. In this way, we see that the flip angle achieved is proportional to the strength of the B_1 field. As only the x-y magnetization produces observable signal, in an inhomogeneous B_1 field, one can adjust the pulse duration to achieve a $\pi/2$ flip angle in the desired spatial region (equivalently region of B_1 field strength) to obtain maximum

signal strength there.

In equation (2.12), there is a further simplification in the B_1 field dependence, which factors

$$B_1(t,\mathbf{x}) \;=\; \mathrm{g}(t)\;\mathrm{f}(\mathbf{x}) \tag{2.18}$$

The factor g(t) is called amplitude modulation, and appropriate choices here will bring us into the special class of "time/band limited" functions. The term f(x) is due to the spatial configuration of the coil windings in the rf coil, and because NMR imagers operate at MHz frequencies (so that the corresponding wavelength is roughly ten meters), the problem of designing appropriate inhomogeneous B_1 fields becomes a problem in static electromagnetism.

2(b) The (relevant) theory of the rotation group

> *"It seems best to fix the underlying general concepts with some precision beforehand, and to that end a little mathematics is needed, for which I ask your patience."*
>
> H. Weyl

We begin with a brief account of the quantum mechanics of a spin 1/2 system in a static magnetic field **B**. The Hamiltonian (equation (2.3)) is easily "solved": the two eigenstates (Φ_1, Φ_2) correspond to the (lower,higher) energies ($-\mu B, +\mu$B) where the spins are aligned (along,against) the direction of **B**. In this way, an arbitrary state of the system

Φ is described by a (complex) linear combination

$$\Phi = c_1 \Phi_1 + c_2 \Phi_2 = (a+bi)\,\Phi_1 + (c+di)\,\Phi_2 \tag{2.19}$$

restricted by the normalization

$$|\,\Phi\,|^2 = |\,c_1\,|^2 + |\,c_2\,|^2 = a^2 + b^2 + c^2 + d^2 = 1 \tag{2.20}$$

The quantum mechanical states of the system are thus naturally put in one-to-one correspondence with the points of the unit sphere S^3 in R^4.

The mathematical fact of the one-to-one correspondence between a set of four real numbers satisfying (2.20) and the group SU(2) of unitary unimodular 2×2 (complex) matrices

$$u = \begin{pmatrix} a+bi & c+di \\ -c+di & a-bi \end{pmatrix} \tag{2.21}$$

is well known[11], as are the Pauli matrices

$$\sigma_x = \begin{pmatrix} 0 & 1 \\ 1 & 0 \end{pmatrix}, \; \sigma_y = \begin{pmatrix} 0 & -i \\ i & 0 \end{pmatrix}, \; \sigma_z = \begin{pmatrix} 1 & 0 \\ 0 & -1 \end{pmatrix} \tag{2.22}$$

(the three orthonormal basis vectors for the Lie algebra su(2) of traceless hermitian 2×2 matrices which generate SU(2) are $i\sigma$).

A further elementary fact of quantum mechanics is the physical reality not of the wave function Φ but rather of its absolute square (2.20) (as the probability of the spin system to be found in the state Φ). But this implies that the state u (2.21) and the state -u both

have the same observable consequences. Hence, while the Lie group SU(2) (the quantum mechanical rotation group), and its corresponding Lie algebra su(2), are the natural choice as representation for a spin 1/2 system, it is really the group SO(3), obtained from SU(2) by identifying antipodal points on S^3, that is the rotation group of consequence in NMR. The rotation group SO(3) is also generated by a three-dimensional Lie algebra, and this algebra is precisely the set of real skew-symmetric 3×3 matrices[11].

We exhibit a standard basis for this algebra

$$I_x = \begin{pmatrix} 0 & 0 & 0 \\ 0 & 0 & 1 \\ 0 & -1 & 0 \end{pmatrix}, \; I_y = \begin{pmatrix} 0 & 0 & -1 \\ 0 & 0 & 0 \\ 1 & 0 & 0 \end{pmatrix}, \; I_z = \begin{pmatrix} 0 & 1 & 0 \\ -1 & 0 & 0 \\ 0 & 0 & 0 \end{pmatrix} \tag{2.23}$$

and immediately draw attention to equations (2.16), the MIBE.

We have now a very simple picture of the MIBE. Equations (2.16) state that the infinitesmal time rate of change of the magnetization in applied magnetic fields is just a sum of the generators of the rotation group SO(3) for the imposed field directions applied to the magnetization itself

$$\dot{\mathbf{M}} = [\Delta\omega \, I_z + \omega_1 \cos\phi \, I_x + \omega_1 \sin\phi \, I_y] \, \mathbf{M} \tag{2.24}$$

The integrated motion of this spin vector **M** is thus a rotation about the instantaneous applied magnetic field.

The powerful insight that this viewpoint (2.24) provides is best illustrated with a brief example, which exploits the knowledge of rotations of rigid bodies in three dimensions.

We choose this example not only to illustrate the usefulness of the rotation group point of view, but also because we shall, in a later section, be interested in understanding phase modulation of the rf field.

2(c) Phase modulation is frequency modulation

In considering the possibilities of phase modulation, it is important once again to review the situation vis-a-vis the Bloch equations. The rotating frame MIBE read

$$\dot{\mathbf{M}} = \mathbf{M} \times \gamma\mathbf{B} \equiv \mathbf{A}\,\mathbf{M} \tag{2.25}$$

or, in components,

$$\frac{d}{dt}\begin{pmatrix} M_x \\ M_y \\ M_z \end{pmatrix} = \begin{pmatrix} 0 & \Delta\omega & -\omega_1 \sin\phi \\ -\Delta\omega & 0 & \omega_1 \cos\phi \\ \omega_1 \sin\phi & -\omega_1 \cos\phi & 0 \end{pmatrix}\begin{pmatrix} M_x \\ M_y \\ M_z \end{pmatrix} \tag{2.26}$$

We notice, however, that since the resonance offset term $\Delta\omega$ is only a function of position $\mathbf{x}$, we can write

$$\begin{aligned} \dot{\mathbf{M}} &= \mathbf{A}\,\mathbf{M} \\ &= \mathbf{C}(\mathbf{x})\mathbf{M}(t,\mathbf{x}) + \mathbf{D}(t,\mathbf{x})\mathbf{M}(t,\mathbf{x}) \end{aligned} \tag{2.27}$$

where

$$\begin{aligned} \mathbf{C}(\mathbf{x}) &= \Delta\omega\, I_z \\ \mathbf{D}(t,\mathbf{x}) &= \omega_1(t,\mathbf{x})\,[\cos\phi(t)\, I_x + \sin\phi(t)\, I_y] \end{aligned} \tag{2.28}$$

By writing the matrix **A** as a sum in this way, we can immediately integrate the time-independent piece **C**. By defining a pseudo-magnetization

$$\mathbf{N} \equiv e^{-\mathbf{C}t}\,\mathbf{M} \tag{2.29}$$

we see that **N** satisfies

$$\begin{aligned} \dot{\mathbf{N}} &= [-\mathbf{C}e^{-\mathbf{C}t} + e^{-\mathbf{C}t}(\mathbf{C} + \mathbf{D})]\,\mathbf{M} \\ &= e^{-\mathbf{C}t}\mathbf{D}e^{\mathbf{C}t}\,\mathbf{N} \\ &\equiv \mathbf{K}\,\mathbf{N} \end{aligned} \tag{2.30}$$

But it is easily seen that

$$e^{-\mathbf{C}t} = R_z(\Delta\omega t) \tag{2.31}$$

($R_z(\alpha)$ is the operator of rotation around the z axis by angle α) so that **K** is in fact just conjugation of **D** by R_z

$$\begin{aligned} \mathbf{K} &= e^{-\mathbf{C}t}\,\mathbf{D}\,e^{\mathbf{C}t} \\ &= R_z\,\mathbf{D}\,R_z^{-1} \end{aligned} \tag{2.32}$$

Hence, because **D** is a linear combination of I_x and I_y

$$\mathbf{D} = \omega_1(t,\mathbf{x})\,[\cos\,\phi(t)\,I_x + \sin\,\phi(t)\,I_y] \tag{2.33}$$

the conjugation by R_z merely produces a phase shift

$$\Delta\phi = \Delta\omega t \tag{2.34}$$

Thus, the constant (in time) frequency modulation $\Delta\omega$ produces a linear phase shift (2.34) so that

$$\mathbf{K} = \omega_1(t,\mathbf{x})\,[\cos(\phi + \Delta\phi)\,I_x + \sin(\phi + \Delta\phi)\,I_y] \tag{2.35}$$

The general case is now clear. An arbitrary phase modulation $\phi(t)$ is the result of a frequency modulation $\Delta\omega(t)$

$$\phi(t) = \int_0^t \Delta\omega(t')\, dt' \tag{2.36}$$

(i.e., to phase modulate by $\phi(t)$ one frequency modulates by $d\phi(t)/dt$). One comment about the experimental relevance of frequency modulation: in medical NMR there are two types, one space-dependent and the other independent of position. As seen above, the imposition of linear gradients (the on-resonance MIBE) produces the linear phase distortion (2.34) at any point in the sample. The second type of frequency modulation comes from off-resonance rf irradiation (the $(\omega-\omega_o)$ term in (2.14) obtained in the transformation from lab to rotating frame) and is independent of position (neglecting rf attenuation effects).

3. Slepian-Hasenfeld-rotation group-pulses (SHARP)

3(a) The "time/band limited" problem

> *"Band-limited functions possess many properties that stem from their analyticity. However, as analyticity is fragile, not all of these persist under small perturbation. If we require that our conclusions remain stable when functions are determinable only with given precision, we are led to problems in which the time-and-frequency-limiting operator enters naturally."*
>
> H.J. Landau

The true paradox in the "time/band limited" problem arises out of a simple contradiction: on the one hand, using a square-integrable function f(t) to describe the behavior of real physical systems, one is necessarily led to believe that f is of finite duration (f has compact support) as there is no physical response when the system is inactive. On the other hand, its square-integrable Fourier Transform

$$F(\omega) = \frac{1}{\sqrt{2\pi}} \int_{-T}^{T} dt\ e^{-i\omega t}\ f(t) \tag{3.1}$$

should also be frequency limited, as physical devices - vocal chords, membranes, oscillators - all have upper limits on the rate at which they vibrate[12]. The inverse for (3.1) is thus

$$f(t) = \frac{1}{\sqrt{2\pi}} \int_{-\Omega}^{\Omega} d\omega \, e^{i\omega t} \, F(\omega) \tag{3.2}$$

The contradiction arises in considering the mathematics of the Fourier Transform, where extending t to the complex plane in (3.1), the requirement that $F(\omega)$ be bandlimited ($F(\omega) \equiv 0$ when $| \omega | \geq \Omega$) implies that f is analytic (actually entire) and hence cannot vanish on any open set without being trivially zero everywhere.

This contradiction is well known to physicists, and has been reformulated as the Heisenberg Uncertainty Principle of quantum mechanics. An elegant resolution was found by some clever people - Slepian, Pollak, and Landau - at Bell Labs in the 1960's[13-16]. Specifically, let f be an arbitrary function supported on some interval [-T,T] on the real line R. To handle the problem of concentrating its Fourier Transform Ft on the interval $[-\Omega,\Omega]$, one needs the singular value decomposition of the map

$$\mathbf{E} = \mathbf{\Omega F T} \tag{3.3}$$

(where $\mathbf{\Omega}$,$\mathbf{T}$ are the operators of restriction to their respective intervals in R). To analyze this problem, the eigenvectors of

$$\begin{aligned} \mathbf{E^* E} &= \mathbf{T F^{-1} \Omega F T} \\ \mathbf{E E^*} &= \mathbf{\Omega F T F^{-1} \Omega} \end{aligned} \tag{3.4}$$

are needed. The heuristic picture is

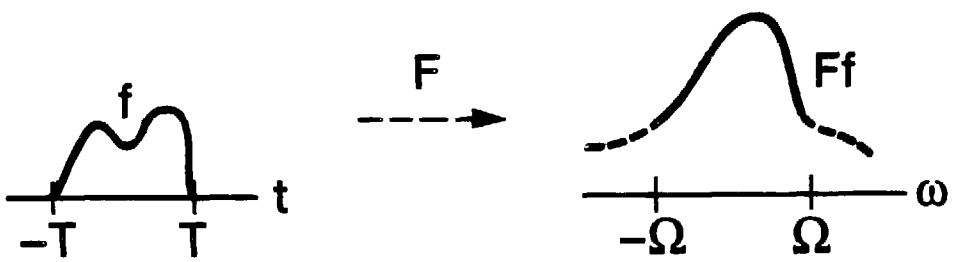

Sketch 3.1

The operator E^*E is an integral operator of convolution type

$$\mathbf{E^*E}f = \int_{-T}^{T} \frac{\sin\ \Omega(t-s)}{\pi(t-s)} f(s)ds = \lambda f(t) \tag{3.5}$$

and is the time-and-frequency-limiting operator referred to above. A mathematical "accident" occurs: a second-order differential operator

$$\mathbf{D} = \frac{d}{dt}(T^2 - t^2)\frac{d}{dt} - \Omega^2 t^2 \tag{3.6}$$

(with simple spectrum) commutes with E^*E, making the computation of the eigenvectors feasible. As the differential operator arises from separating the Helmholtz scalar wave equation in prolate spheroidal co-ordinates, the eigenfunctions are appropriately named prolate spheroidal wave functions (pswf).

This accident is very useful for explicitly evaluating the eigenfunctions, a task which we shall soon be concerned with. Since E^*E commutes with D in (3.6), and D has simple spectrum, they share the same eigenfunctions. The computation of the eigenfunctions of

D, however, is possible. When we discretize the problem, this will amount to numerically computing the eigenvectors of a particular tridiagonal matrix, and a simple numerical routine exists for precisely this task[17].

We now consider an NMR analogue to this problem, in which the two domains of time and frequency are present, although the map connecting them is no longer the Fourier Transform F, but $\mathcal{B}$, the Bloch Transform. One notices that the above prolate spheroidal wave functions satisfy two properties of real rf pulses

(1) they live on a finite interval ([-T,T] in this case)

(2) an analogue exists for a discrete version of the left side of

Sketch 3.1, and so the pswf can be found in discrete form

so that in trying to identify a class of functions to be used as amplitude and phase modulations in g(t) in equation (2.18), one should not be too suprised to find that the pswf appear[10].

3(b) The Bloch Transform

> *"We had answered questions we had not meant to ask in optics, detection and estimation theory, quantum mechanics, laser modes - to name a few."*
>
> D. Slepian

In attempting to spatially localize the NMR signal, one must take account of the finite duration of the rf signal (ω_1, ϕ). By applying a linear gradient in B_o, a linear spatial axis

(along the applied gradient direction) is made equivalent to a linear frequency axis, so that the NMR signal is spatially decoded by examining its frequency components. The gradient field defines a resonance offset

$$\Delta\omega = \gamma \mathbf{G} \cdot \mathbf{x} \tag{3.7}$$

so that in localizing the signal, one desires a certain response $\mathbf{M}(\Delta\omega)$ in some given region (or bandwidth), while in other regions (ranges of $\Delta\omega$), the magnetization should be unaffected, thereby not contributing to the detected signal. Since the rf input which disturbs the equilibrium magnetization is a finite time signal, we have the following (heuristic) picture when a linear gradient is imposed

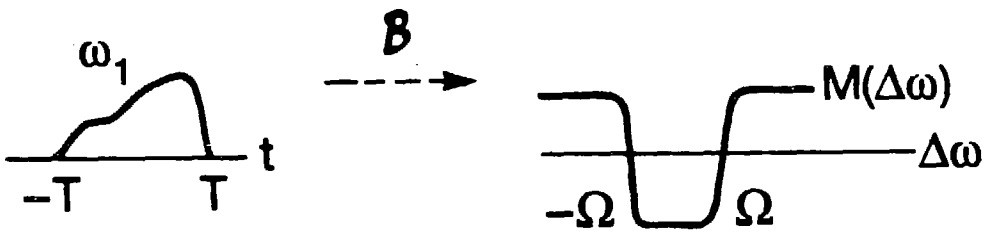

Sketch 3.2

where $\mathcal{B}$ stands for the Bloch Transform[18] (the nonlinear transformation from $B_1(t)$ to $\mathbf{M}(\Delta\omega)$), and the desired response of M is localized in space (equivalently frequency). Two points here: the first is that one desires a sharply localized response in order to achieve sharp spatial localization. The second point is that the linear part of the transformation $\mathcal{B}$ at 0 is F[18], so that the coincidence in Sketches 3.1 and 3.2 is more than accidental. As

the question of the invertibility of $\mathcal{B}$ is still an open one[18], we now proceed to describe a particular choice of $\omega_1(t)$ and $\phi(t)$.

3(c) Modulations

In the rotating frame on resonance ($\Delta\omega$=0), the rf input can be written

$$\gamma \mathbf{B}^{\mathbf{eff}} = \omega_1(t)\ [\cos\ \ \phi(t)\ \hat{x} + \sin\ \ \phi(t)\ \hat{y}] \tag{3.8}$$

where $\omega_1(t), \phi(t)$ are arbitrary finite time signals (called amplitude and phase modulations, respectively). From the analogy made above between Sketches 3.1 and 3.2, we tried pswf as input to the rf field $\omega_1(t)$ and $\phi(t)$, and numerically solved the Bloch equations to determine the response as a function of $\Delta\omega$. As the rf field experimentally is a digitally sampled function, and the numerical simulations are finite step ODE solvers (described below), we needed a discrete version of the pswf. Fortunately, one exists[19]. In this discrete case, the simultaneous concentration of a function defined on the integers Z and its dual the circle S^1 is considered, and again a heuristic picture looks like

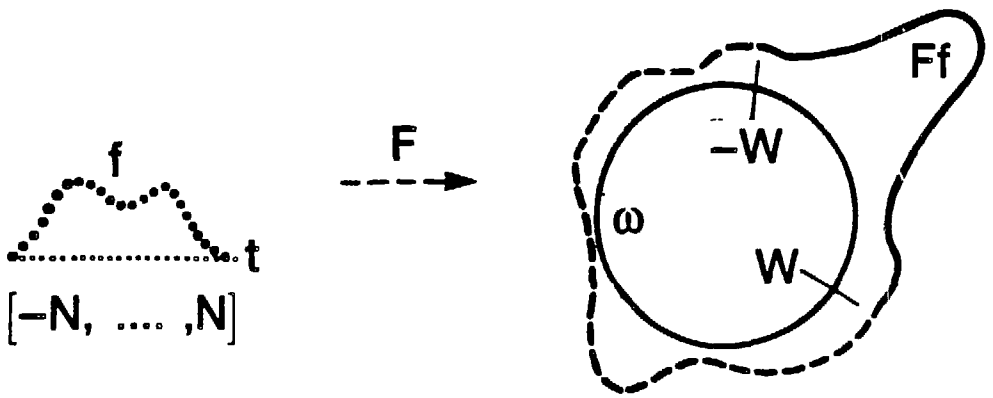

Sketch 3.3

This time a symmetric tridiagonal N×N matrix[19] $\tilde{D}$ replaces the commuting second order differential operator in (3.6)

$$\tilde{D}(N,W)_{ij} = \begin{cases} \frac{1}{2}i(N-i) & j = i-1 \\ (\frac{N-1}{2}-i)^2\cos 2\pi W & j = i \\ \frac{1}{2}(i+1)(N-1-i) & j = i+1 \\ 0 & |\, j-i \,| \geq 2 \end{cases} \tag{3.9}$$

(i,j=0,1,...,N-1) and its eigenfunctions are obtained by a fast QR diagonalization[17].

For a choice of $\omega_1(t)$ in the Bloch equations ODE solver (see chapter 5), we began with the eigenvector of [19] with the largest eigenvalue (the eigenvalues measure simultaneous concentration). The original plan was to use the pswf to design improved $\pi/2$ pulses, since the map $\mathcal{B}$ is not too nonlinear there, and so "close to" F. The surprising results for π pulses are shown in Figure 3.1. These simulations, while of real practical value in displaying the final position of the magnetization $\mathbf{M}(\Delta\omega)$, offer little insight into the dynamics of the "slice" formation. In Figure 3.2, we also show some interesting simulations of the time development of the evolving magnetization.

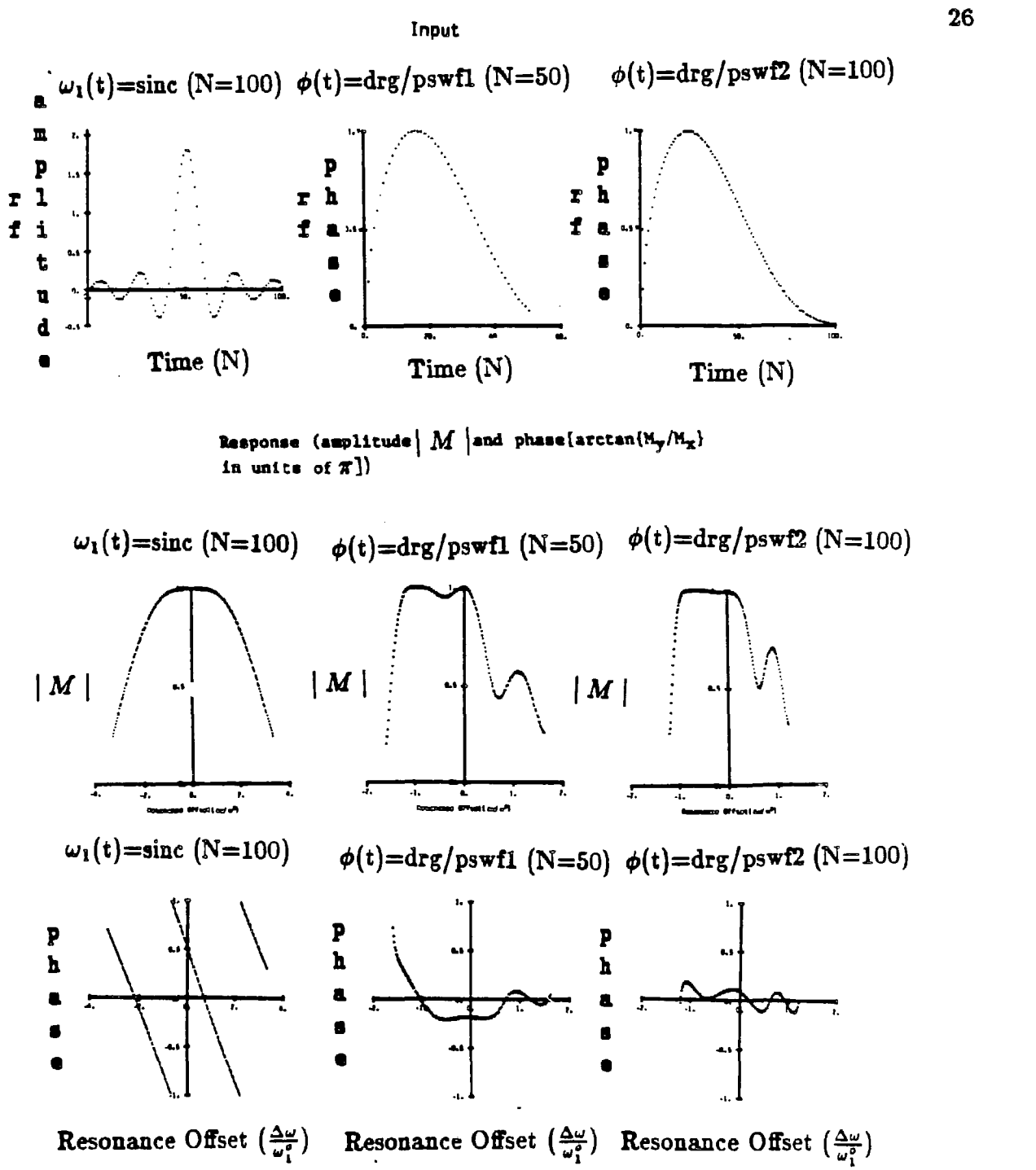

Figure 3.1: The three simulations shown (read vertically as input followed by response) compare discrete prolate spheroidal wave function (dpswf) amplitude modulated (ϕ(t)=0) π pulses to a "standard" pulse[20].

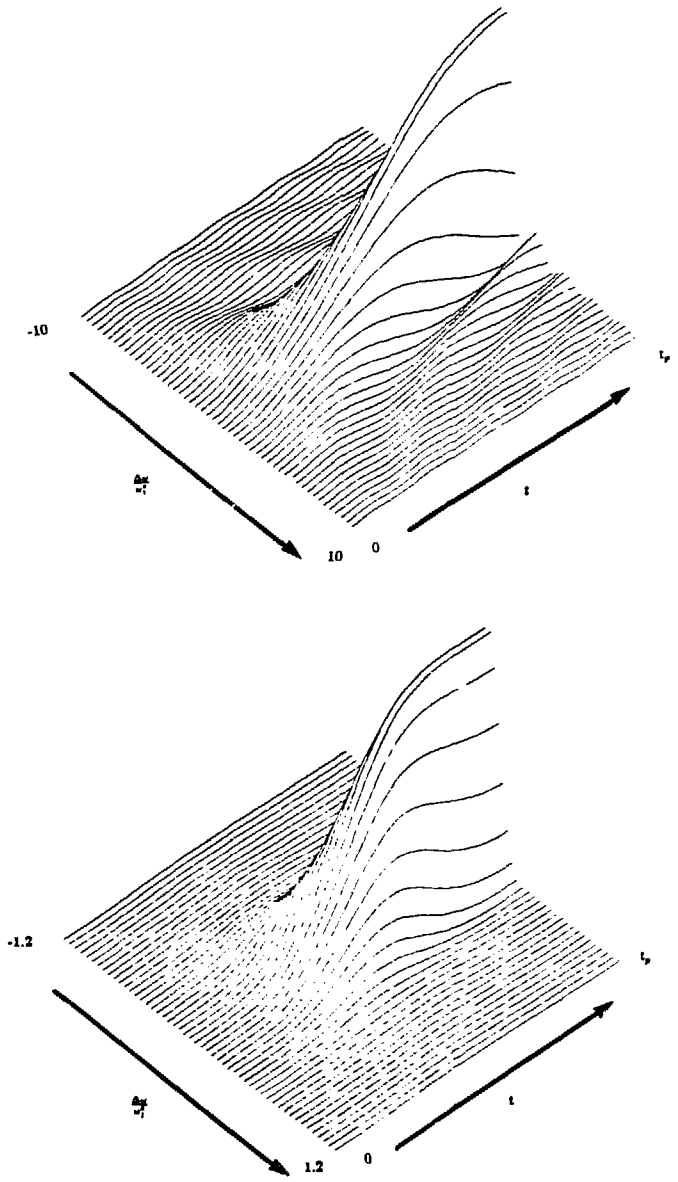

Figure 3.2: The two simulations shown compare the time development of the "slice" selected in a constant amplitude π pulse (top) and a discrete prolate spheroidal amplitude modulated π pulse (bottom). t_p is the pulse duration, and the z component of the magnetization for various times and resonance offset values is plotted, with the equilibrium value $+1$ at the bottom of each diagram.

Strengthened by this success, we proceed to another (looser) analogy based on the preceeding Sketches 3.1, 3.2, and 3.3. According to the Bloch equations (neglecting relaxation), the path described by the evolving magnetization under the influence of magnetic fields lies on the surface of the sphere S^2 in R^3. One application for the appropriately designed rf modulation is a narrowband $\pi/2$ pulse with constant phase response $(\arctan(M_y/M_x))$. From the viewpoint of evolving paths on S^2, the desired response is for all the paths to terminate around a point in the x-y plane. The one-parameter family of paths is indexed by the resonance offset $\Delta\omega$, whereas all the paths start at the north pole (identified with the equilibrium configuration, independent of $\Delta\omega$).

The results of Slepian, Landau, and Pollak have been extended to the sphere[21]. For our case, we take the "frequency domain" space to be the rotation group SO(3) (with the sphere S^2 sitting inside) while the "time domain" becomes the non-negative integers Z_+. The domains of concentration are [0,...,L] and the polar cap in S^2 of "radius" b (i.e., $b \leq \cos\theta \leq 1$). The analogue for NMR is not quite orthodox, in that while we do take [0,...,L] to be the domain of a finite time rf digital signal, we do not consider the simultaneous concentration of a corresponding function on S^2. Instead, the polar cap is viewed as the locus of the end-points of the paths mentioned earlier (an equivalent description is to consider the polar cap as an ϵ-ball in SO(3) around the fixed rotation of $\pi/2$ around the x axis $R_x(\pi/2)$). We have the following (heuristic) picture

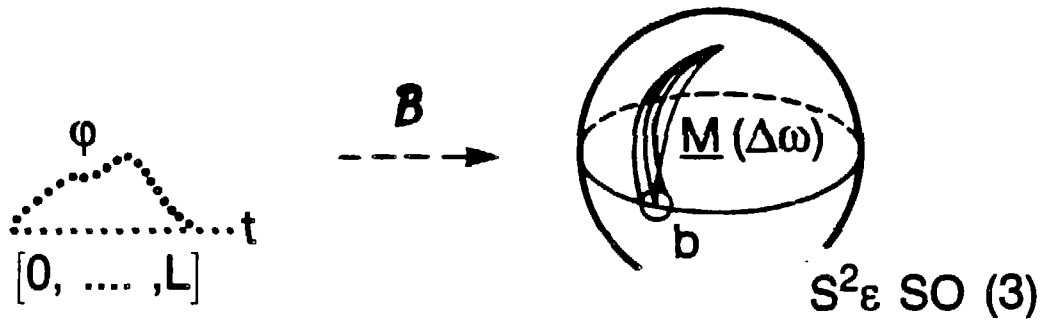

Sketch 3.4

Again a tridiagonal matrix $\tilde{D}$ is exhibited

$$\tilde{D}(L,b)_{ij} = \begin{cases} \alpha_i b & i = j = 1, ..., L+1 \\ \gamma_j & j = 1, ..., L \\ 0 & |\, j - i \,| \geq 2 \end{cases} \tag{3.10}$$

where

$$\alpha_i = -i(i-1) \ , \ \gamma_i = i\frac{i^2 - (L+1)^2}{\sqrt{4i^2 - 1}} \tag{3.11}$$

and the eigenvectors are taken as the phase modulation $\phi(t)$ ($\omega_1(t) \equiv$ constant) in (3.8). The eigenvector with largest eigenvalue produces the desired constant phase magnetization response shown in Figure 3.3.

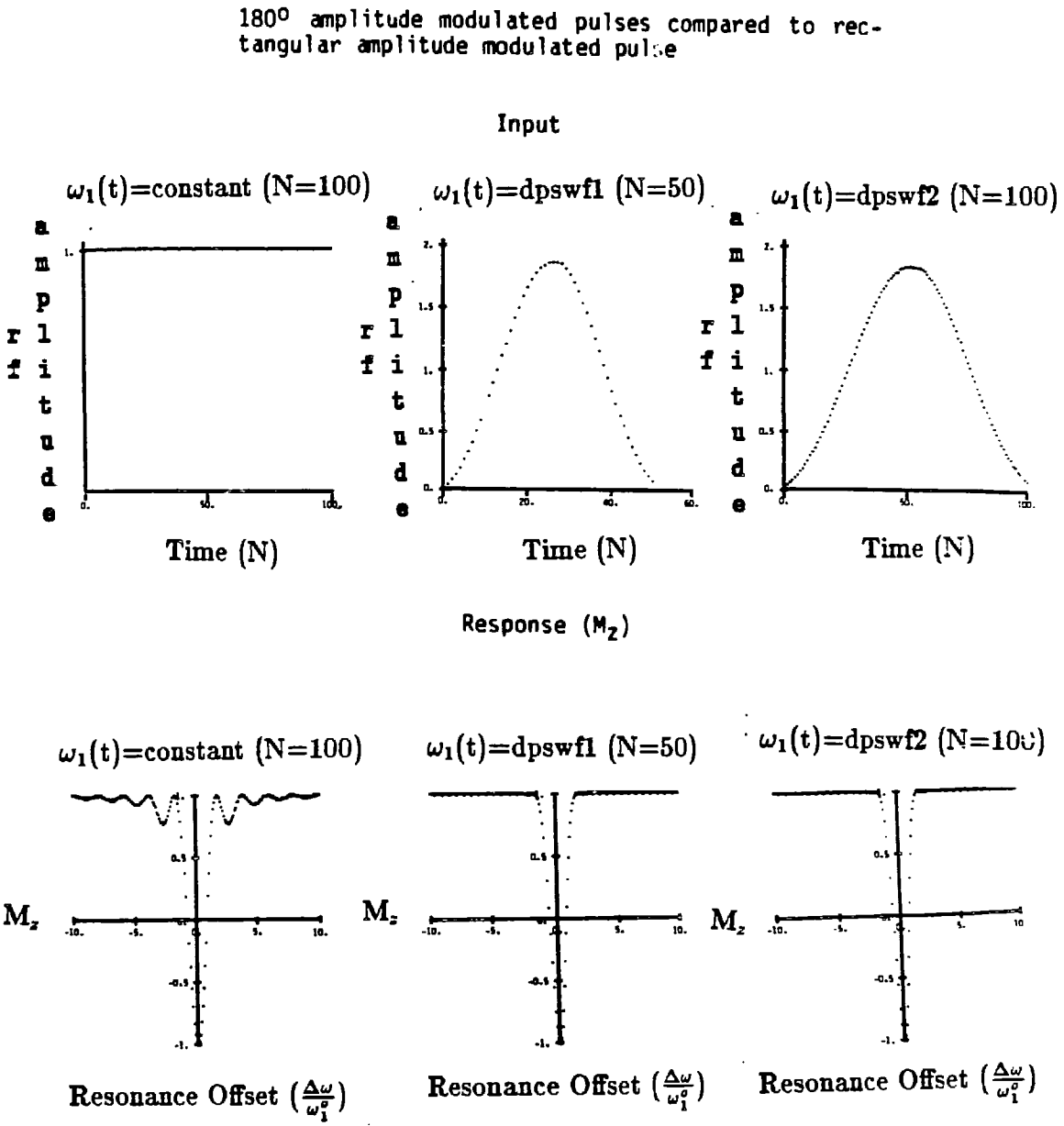

Figure 3.3: The three simulations shown (read vertically as input followed by response) compare discrete rotation group prolate spheroidal wave function (drg/pswf) phase modulated (ω_1(t)=constant) $\pi/2$ pulses to a "standard" pulse[20].

3(d) A geometric picture of the Fourier Transform

For the preceeding example Sketches, there is a rigourous mathematical treatment that justifies these heuristic analogies. We briefly describe this group representational point of view for Sketch 3.3, to illustrate the mathematics behind these simple pictures.

Considering the (square-integrable) function f defined on the circle S^1 (i.e., $f \in L^2(S^1)$), we can Fourier decompose it into the sum

$$f(\theta) = \sum_{m=-\infty}^{\infty} \hat{f}(m) e^{im\theta} \tag{3.12}$$

where $\hat{f}(m)$ are the Fourier coefficients in the usual way[22]. The function f is thus decomposed into its one-dimensional "pieces" $\hat{f}(m)e^{im\theta}$, each "piece" lying in the subspace spanned by $e^{im\theta}$, and so labeled by the integer m. In mathematical language, the circle group S^1 is said to have unitary irreducible representations labeled by the m in Z (the integers), where $e^{im\theta}$ form the basis functions for the vector spaces on which f is represented. Thus this geometric view of the Fourier Transform (that it takes functions in L^2 into its unitary irreducible pieces) is basically a fact about the geometry of L^2, which is a separable Hilbert space. In Sketch 3.3, then, the other side of the diagram (i.e., the integers Z) are precisely these integers m, so that sitting above the m^{th} "dot" is really a projection operator onto the irreducible subspace spanned by the m^{th} eigenfunction. In the case of S^1, all of these representations are one-dimensional, but for example, for S^2 in Sketch 3.4, these subspaces are 2L+1-dimensional, corresponding to the subspaces spanned by the spherical

harmonics (i.e., the Y_{lm}, for m unrestricted and fixed l=L).

The paradox of "time/band limiting" thus has a very natural geometric interpretation: restricting the Fourier Transform of a function f to live in a subspace of L^2 spanned by only a finite number of unitary irreducible representations (by setting $\hat{f}(m) \equiv 0$ for $| m | \geq M$, how well can one concentrate f? For example, in order to absolutely concentrate a function on the circle S^1, we want

$$f(\theta) \equiv \delta(\theta) = \sum_{m=-\infty}^{\infty} e^{im\theta} \tag{3.13}$$

so that we need all the integers m in Z. But how well can we do if we only allow $| m | \leq$ M=50? The answer is given by the prolate spheroidal wave function in Sketch 3.3 with the largest eigenvalue, which is the only eigenvector of the 50×50 matrix supplied in (3.9) with no changes in sign (and which we numerically compute using the QR algorithm in [17]).

3(e) On gaussian pulses

> *"Gaussian pulses should prove useful for the majority of applications of frequency-selective excitation."*
>
> C. Bauer, et. al.

In considering amplitude modulation in the rotating frame, a tempting relationship between the Fourier Transform and the Bloch equations (with regard to the amplitude of $B_1(t)$) is usually constructed. A major motivation for the development here of prolate

spheroidal modulated pulses is indeed based on this fact. Nevertheless, one should not rely solely on this (assumed) Fourier conjugacy between time and frequency, as in fact, the NMR system is inherently nonlinear, and these linear attempts towards approaching a solution to the modulation problem obscure its true nature.

In particular, there are some simple realities of pulse NMR that conspire to force a re-evaluation of the relevance of the linear and continuous approaches. Recall that the rf pulses used in the laboratory are finite digital signals, not infinite continuous ones. If the modulation problem really was time/band limiting in the Fourier sense, then gaussians[23] (in the infinite interval case) and prolate spheroidal wave functions (in the finite interval case) would be the right functions to use. The virtue of the use of prolate spheroidal functions over gaussians is to be found in specifically answering two of these restrictions, namely finiteness and discreteness of the rf temporal waveforms. We are still left at this point with addressing the nonlinearity.

In the actual use of these functions in NMR, the simulations and experiments are ultimately the deciding factor. As the time development obeys the Bloch equations, and is not the Fourier Transform, one should not expect that either the gaussian or the prolate spheroidal functions should work optimally, if at all. The fact that they both do well in simulation, however, suggests that the prolate spheroidal functions would be preferred, as no additional problems of sampling and truncation are introduced.

We illustrate the comparison in Figure 3.4. We use a nonlinear χ^2 fit[24] of a gaussian

to the top prolate spheroidal N=32 wave function, and compare the inversions obtained. One can see that the dpswf (discrete pswf) offer a slightly sharper response, and so the considerations of finiteness and digital nature of the rf temporal waveforms are meaningful. We also invite the reader to compare the experiments in Figure 5.3 on page 59.

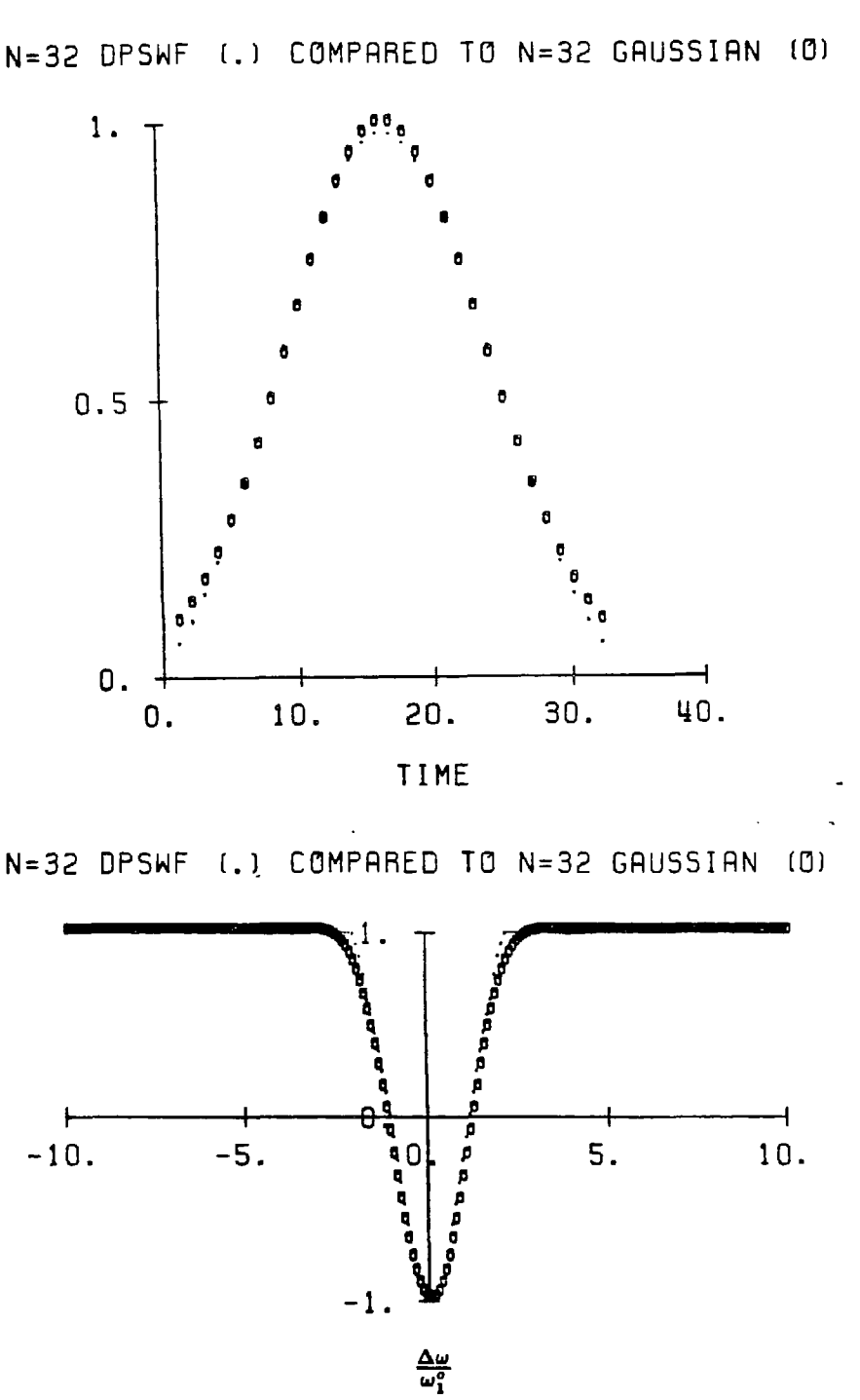

Figure 3.4: A comparison of N=32 point temporal waveforms. The gaussian obtained using the Marquardt algorithm is compared to the discrete prolate spheroidal wave function both as a time domain signal and as an rf amplitude modulated π pulse, where M_x is plotted versus $\frac{\Delta\omega}{\omega_1^\circ}$.

4. Inhomogeneous rf Fields

4(a) Basic physics according to Maxwell

> *"It required the genius of J.C. Maxwell, spurred on by Faraday's observations, to see the inconsistency in [the static] equations and to modify them into a consistent set which implied new physical phenomena, at that time unknown but subsequently verified in all details by experiment."*
>
> J.D. Jackson

We consider here the factor f(x) in equation (2.18), the spatial dependence of the B_1 field. The purpose of this chapter is to design rf coils which produce a small volume of homogeneous field, and a rapidly divergent field in other regions. In this way (recalling the argument given in section 2(a)), one can obtain a spatially selective region of optimal $\pi/2$ flip angle, while other regions of the sample placed in the coil will not contribute significantly to the acquired signal. However, there are two important considerations to be kept in mind here: one is the reciprocity argument[25] stating that the signal produced in the coil from a given region is proportional to the B_1 field in that region (so that, by

scaling $\theta = \gamma B_1 t_p$, the signal scales like $\theta \sin\theta$, where the factor $\sin\theta$ is due to the sinusoidal dependence of the signal on flip angle). The other is that the source-free Maxwell equations do not support local maxima for the static fields **E** and **B** used in this approximation.

The demonstration of these two facts is made by simple application of the Maxwell equations[26,27]. For the reciprocity argument, we want to show that the flux induced in a coil from a precessing moment **m** is proportional to the magnetic field at the moment's location due to a unit current in the coil

$$\int_S \mathbf{B_m}(\mathbf{x}) \cdot \hat{\mathbf{n}}\, da \sim \int_C \frac{\mathbf{l} \times (\mathbf{x} - \mathbf{x_l})}{|\,\mathbf{x} - \mathbf{x_l}\,|^3} \tag{4.1}$$

where $\mathbf{x_l}=(x_l, y_l, z_l)$ labels the coil describing curve C and the curve C spans a surface S. But the vector potential for the magnetic moment **m** is just

$$\mathbf{A}(\mathbf{x}) = \int_C \frac{\mathbf{m} \times (\mathbf{x} - \mathbf{x_l})}{|\,\mathbf{x} - \mathbf{x_l}\,|^3} \tag{4.2}$$

so that, using Stokes' Theorem,

$$\begin{aligned} \textstyle\int_S \mathbf{B_m}(\mathbf{x}) \cdot \hat{\mathbf{n}}\, da &= \textstyle\int_S \nabla \times \mathbf{A}(\mathbf{x}) \cdot \hat{\mathbf{n}}\, da \\ &= \textstyle\int_C \mathbf{A}(\mathbf{x}) \cdot \mathbf{l} \\ &= \textstyle\int_C \frac{\mathbf{m}\times(\mathbf{x}-\mathbf{x_l})}{|\mathbf{x}-\mathbf{x_l}|^3} \cdot \mathbf{l} \\ &= -\textstyle\int_C \frac{\mathbf{l}\times(\mathbf{x}-\mathbf{x_l})}{|\mathbf{x}-\mathbf{x_l}|^3} \cdot \mathbf{m} \end{aligned} \tag{4.3}$$

This computation shows that the closer the spins are to the coil, the more they couple to it (i.e., induce a larger current), as would be expected from intuition.

The second fact, that the Maxwell equations do not support local maxima in B (away from currents), comes from another feature of the Maxwell equations, namely that they lead to inhomogeneous wave equations; for example

$$\nabla^2\mathbf{B} - \frac{1}{c^2}\frac{\partial^2}{\partial t^2}\mathbf{B} = \frac{4\pi}{c}\mathbf{J} \tag{4.4}$$

For source-free regions, we thus obtain a homogeneous wave equation

$$\nabla^2\mathbf{B} = \frac{1}{c^2}\frac{\partial^2}{\partial t^2}\mathbf{B} \tag{4.5}$$

However, the right hand side vanishes, since we make the quasi-static approximation (recall that the wavelengths of interest are an order of magnitude larger than the objects of interest, and so propagation is neglected). Thus B is a harmonic function in the source-free region, and hence obeys the maximum principle[28], namely that B attains its maximum value on the boundary of the source-free region. Thus away from the current sources, no local maxima can exist.

As a result of these two important considerations, only a small region of homogeneity in which B_1 has a local minimum can be expected. Thus we must use other techniques, such as designing pulse sequences sensitive to rf inhomogeneity or using phase-cycling to eliminate high flux signals, to cancell regions in which the magnetic field B_1 although divergent is larger in magnitude. In addition, although the Maxwell equations completely describe the magnetic fields produced by current sources, in general there will be no analytic formula for the magnetic fields produced from a given configuration of coil windings, so that numerical

methods must be used to map out the fields.

4(b) Coils

"Let that sucker fly!"
T.F. Budinger

The basic calculation used to determine the magnetic field produced by a wire with constant current j (recall propagation effects are neglected since the relevant wavelengths are long) is beased on the Biot-Savart Law

$$\mathbf{B}(\mathbf{x}) = \mathrm{j} \int_C \frac{\mathbf{l} \times (\mathbf{x} - \mathbf{x}_\mathbf{l})}{|\,\mathbf{x} - \mathbf{x}_\mathbf{l}\,|^3}\, d\mathbf{l} \tag{4.6}$$

where C is the loop of wire containing the current j=| **J** |. There are some coils for which this integral can be done analytically, but for reasons of both computational simplicity and practical utilty, we have used digital computations.

The simplest example is one of a single turn loop. While an analytic solution exists (in terms of K and E, complete elliptic integrals of the first and second kind[29]), not only are these functions typically unavailable in digital form, but also, given the finite resolution of the display screen used to show the two-dimensional slices, the discrete line element approximation to the loop works just as well. There is another simplifying feature in the calculation of the B_1 field profiles, which is that there is a cross-product in the Bloch equations, so that one is only interested in the components of B_1 perpendicular to the B_o field.

Again, we emphasize here that, as a result of the physical limitations imposed in order to be in agreement with the Maxwell equations, the best we can achieve in coil design is a resonably well defined region of minimum **B** field. This then has the disadvantage that, as the signal scales linearly with field strength, the signal will be low. Moreover, the "hot" spots in the field will necessarily be close to the current sources, and as the coil is placed close to the body surface, a means to eliminate these regions of high surface signal must be found.

4(c) Pulse sequences

We illustrate the simulations developed with some examples. In particular, we simulate the three-dimensional spatial sensitivity of three coil geometries, represented by slices taken at several displacements from the coil axis. The three geometries depicted in Figure 4.1 are:

(1) a circular surface coil[30,31]

(2) a pair of coils

(3) a coil constructed of straight wire segments called a "baseball" [32]
(due to its similarity in shape to the seam on a baseball).

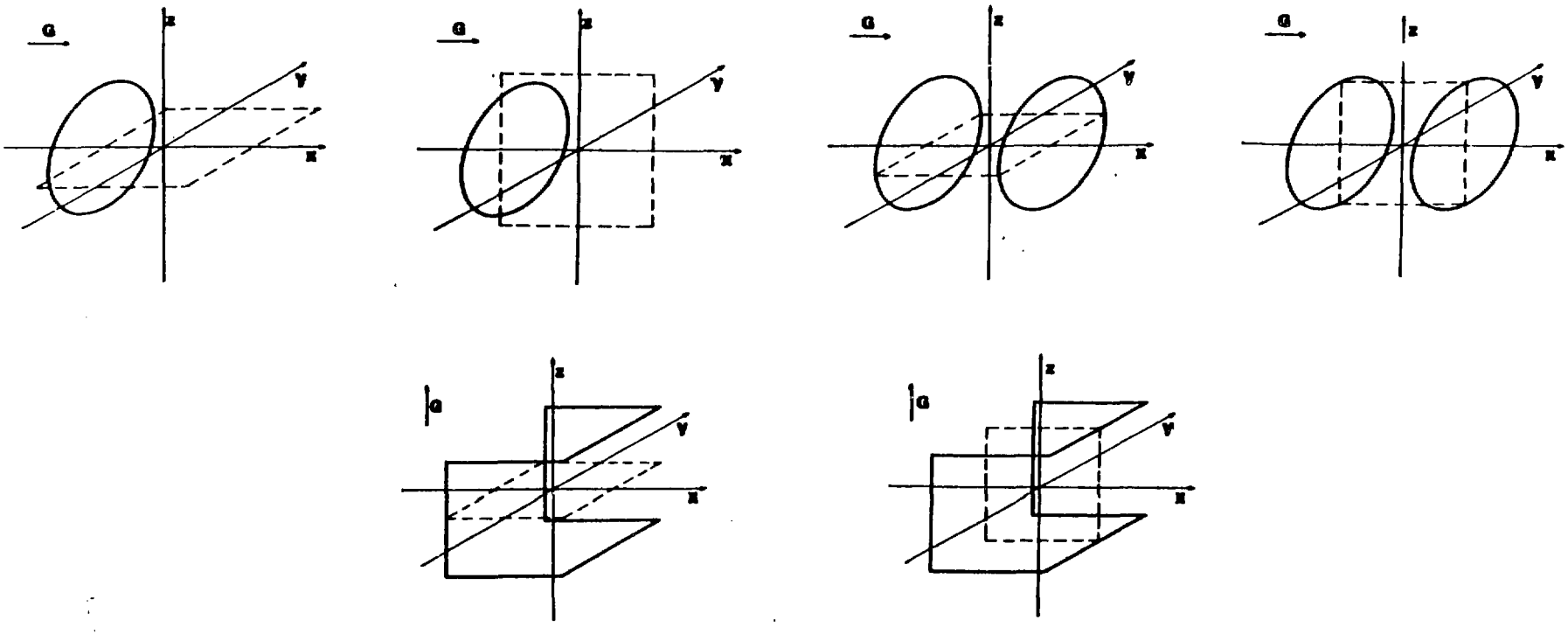

Figure 4.1: The three coil geometries, as well as the planes on which the B_1 field is evaluated are diplayed. The one-turn coil is at the top left, the pair of coils is at the top right, and the "baseball" coil is below.

The calculation of the components of B_1 perpendicular to the B_o field in free space uses the quasi-static approximation of the Biot-Savart Law (it is obvious from the Bloch equations that only the perpendicular components matter). The circular current loop was approximated by 360 current elements and the field computed using the Biot-Savart law. The integral was evaluated once on a two dimensional rectangular grid containing the coil axis and the result stored, allowing maps through any plane to be constructed by simple rotation and interpolation. The B_1 field for the straight sided "baseball" is easily evaluated analytically. The projection of the B_1 field vector onto the x-y plane was evaluated on a 101×101 point grid for display and calculation of sensitivity maps.

As mentioned previously, one cannot violate the Maxwell equations, and therefore the signal induced in the pickup coil will be strongest on the boundary of the source-free region, namely at the coil windings. One way to eliminate the high signals produced near the coil currents is to use pulse sequences sensitive to rf field strength. In the rf field strength-sensitive phase-cycled pulses of Bendall and Gordon[33], the "high flux" signals are cancelled by averaging a number of NMR experiments, each performed with a different rf phase (the ϕ in equation (2.16)).

Once one has the effective rf field strength on a co-ordinate grid for the slice of interest, one can simulate various pulse sequences sensitive to such rf inhomogeneities. The example of the Bendall-Gordon phase-cycled method is suitable to modification using SHARP (chapter 3), while another family of rf sensitive "composite" phase pulses[34] has been

simulated, but cannot be implemented with SHARP[20], as we shall soon see.

To illustrate some of the potential of depth pulses in the three coil geometries, we show in Figure 4.2 maps of the B_1 field, the response to a single wide bandwidth pulse, and the response to one of the pulse sequences developed by Bendall[35]. The depth pulse sequence simulated is denoted:

$$2\theta\ [\pm x];\ (2\theta\ [\pm x, \pm y])_2;\ acquire\ . \tag{4.7}$$

[± x] and [± x,± y] denote phase cycling and the subscript 2 indicates that the last pulse is repeated. The acquired signals are summed (or subtracted in the case of an odd number of ± phases) until the entire phase cycle is complete. The response to the depth pulse is proportional to

$$-\theta\ cos\ 2\theta\ sin^4\ \theta\ [\ 2sin\ \frac{2}{3}\theta\ +\ sin\ \frac{4}{3}\theta]/3\ . \tag{4.8}$$

This rather complicated sequence provides excellent suppression of signals from regions having flip angles near 270 degrees. Useful results with less complete suppression of the 270 degree region may be obtained with shorter sequences.

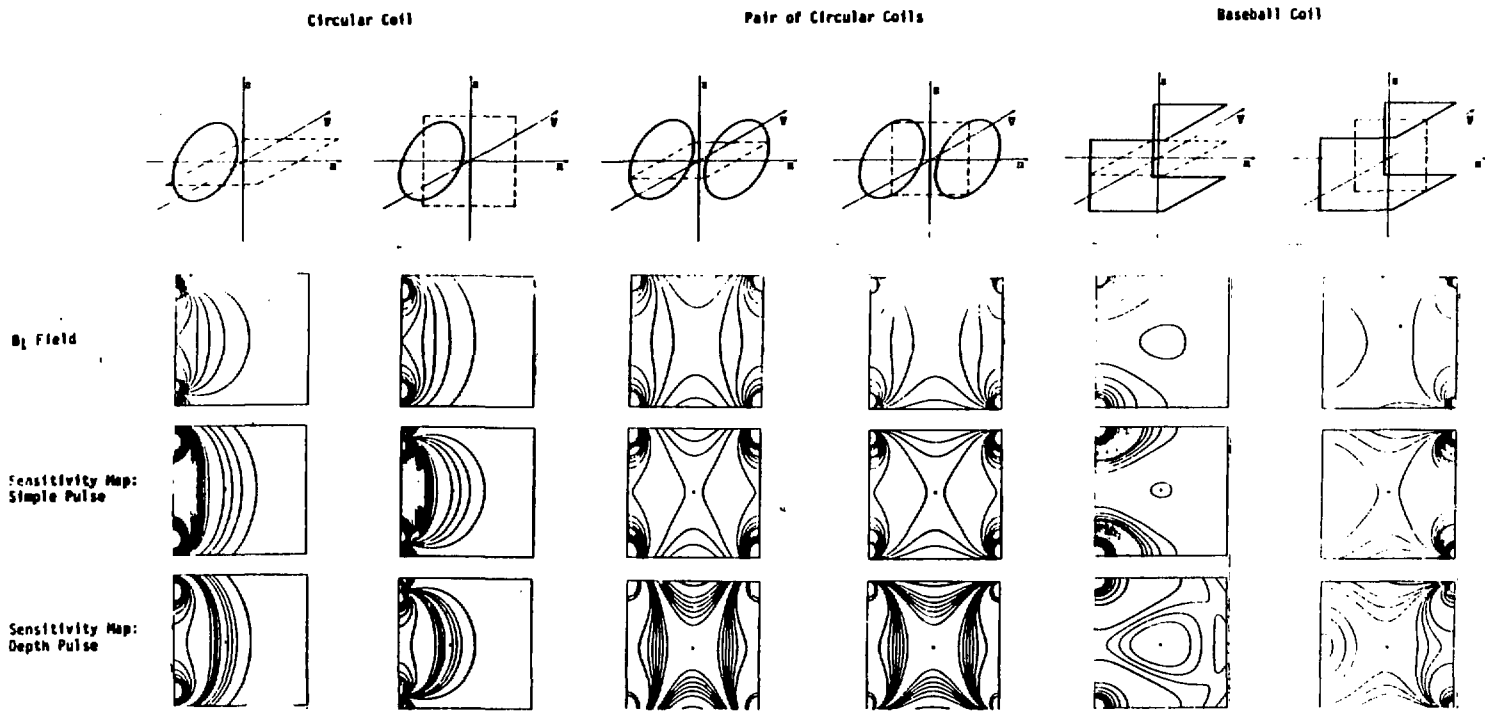

Figure 4.2: Simulations of the three representative geometries chosen are shown[36]. The B_1 field is scaled to produce a flip angle of 90° one radius away from the surface coil on its axis. The signal induced in the coil from each volume element after a simple hard pulse is proportional to $\theta \sin \theta$. (Volume elements contributing positive and negative signals are coded with solid and dotted lines, respectively).

4(d) B_1 and ΔB_o together

The two (temporal and spatial) aspects of the problem so far have been separated by some simple restraints concerning the production of the rf field (see equation (2.18)). In addition, the relevant field strengths in this approach to these two parts of the spatial localization problem are distinct (i.e., for the temporal problem, one is interested in the behavior of the magnetization as a function of the linear main field strength B_o inhomogeneity, while the spatial problem is one of coil geometry to provide rf field inhomogeneity). It is thus quite natural to ask whether the "solutions" to these two problems can be combined. The particular division of the problem we have chosen makes the combination possible.

In particular, recall that in our approach to the temporal problem, we ask that a certain response be achieved in a single rf pulse. On the other hand, for the coil problem, we find that one can improve the rf inhomogeneity sensitivity profile by averaging a number of experiments. We can therefore combine these two approaches by tailoring the rf pulses in a given experiment, and then averaging. We can thus see the difficulty of combining SHARP with other, "composite" pulse schemes, since these methods rely on a single, phase-modulated pulse.

But the interesting feature here is that the two different pulse schemes, SHARP and phase-cycled depth pulses of Bendall and Gordon, are sensitive to different field strengths, main field B_o linear inhomgoneity for SHARP and B_1 rf inhomogeneity for depth pulses.

Hence the natural combination of these two, provided that the experiments take place in the combined fields of linear B_o gradients and an inhomogeneous B_1 rf field.

The imposition of gradients in the B_o field and use of rf coils producing B_1 field inhomogeneity provide two "degrees of freedom" for the spatial sensitivity problem. A class of amplitude and phase modulated pulses called SHARP (chapter 3) have been designed for narrowband excitation in the presence of a gradient. We simulate the signal obtained from an inversion-recovery T_1 measurement, in which the FIDs from the experiments θ_2-acquire and $\theta_1 - \tau - \theta_2$-acquire are subtracted, where θ_1 is an amplitude modulated selective inversion pulse and θ_2 is a simple pulse. A gradient is applied during θ_1 so that inversion occurs at the same point as θ_2=90 degrees. Away from the region of interest the θ_1 pulse has little effect, so that the signals cancel in subtraction. If the purpose is not a T_1 measurement, τ may be made as close to zero as the gradient settling time will allow. (Ordidge has proposed a similar method[37]).

The method utilizes the spatial B_1 field maps developed above, but now, at each point in the spatial domain of the coil, values for both the main field strength and rf field strength are calculated ($\Delta\omega$ and ω_1, respectivelv) A signal surface table is generated on a grid of $\Delta\omega$ and ω_1 values with the Bloch ODE solver, and this table is then correlated with the particular pair of magnetic field strength values at each site in the spatial ΔB_o-B_1 map by linear interpolation to produce the selective slice sensitivity maps. The signal surface table for an amplitude modulated π pulse is shown in Figure 4.3, and the sensitivity maps

are presented in Figure 4.4 with a linear B_o gradient imposed along the axis of a surface coil and for the two coil case; the coil diameter is 10 cm and the gradient is 1 gauss/cm for all cases. The simulations assume τ=0.

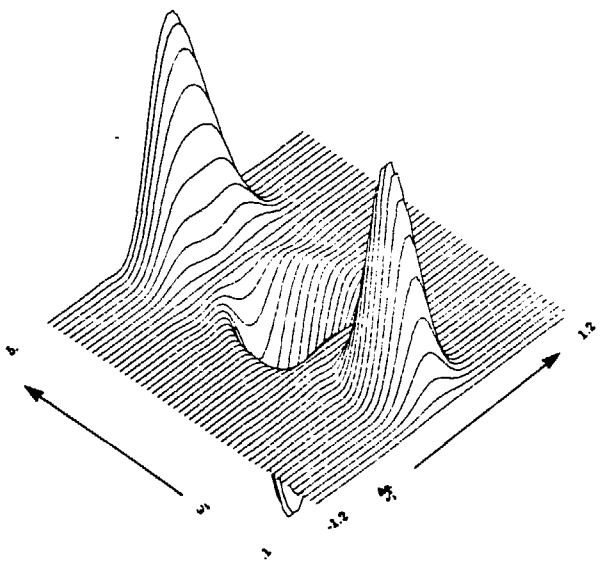

Figure 4.3: The spin signal surface produced by subtracting the FID obtained from selective π pulse followed by a broadband $\pi/2$ pulse from the FID obtained from a broadband $\pi/2$ pulse (i.e., we compute s=sin θ - M_z sin θ). M_z is the final z component after the selective π pulse. The true signal is then by reciprocity proportional to θ·s. Both rf and gradient values are in gauss.

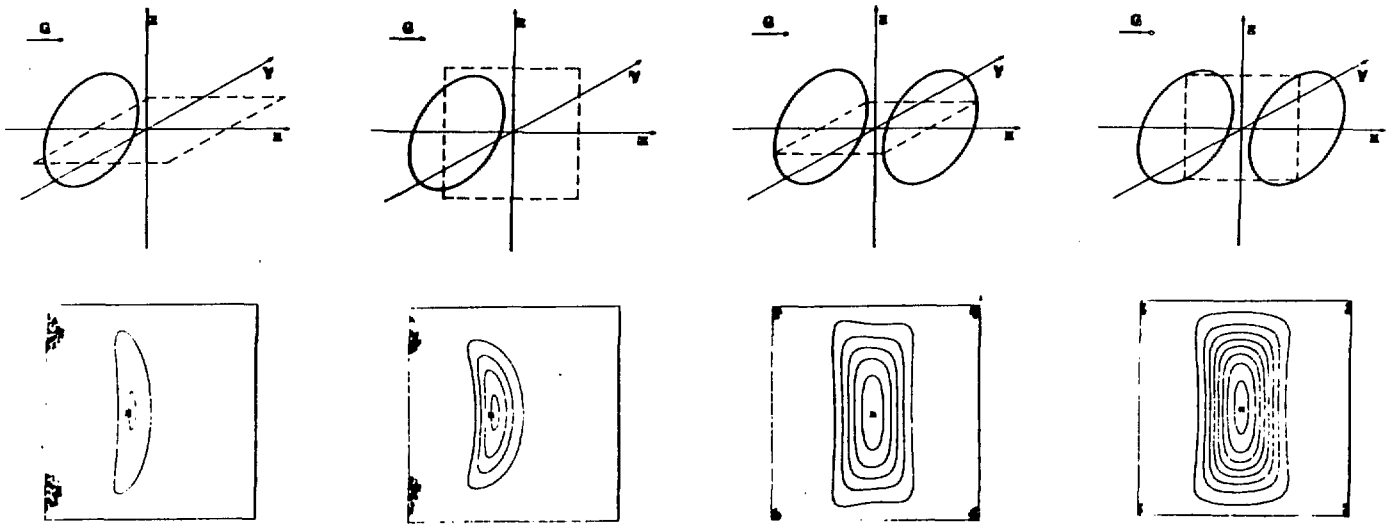

Figure 4.4: Selective excitation in the presence of a gradient: the response from a selective amplitude modulated π pulse is simulated (bottom row) for the two geometries shown (top row)[36].

In the depth pulse case, the rf (flip angle) selectivity is achieved by phase cycling a number of repeated experiments. SHARP, however, achieves frequency selectivity by temporally profiling a single pulse. The two methods can thus be combined, as is shown in Figure 4.5 for the baseball coil with a linear B_o gradient in the z direction. We subtract the accumulated FID's from the experiments:

$$\begin{aligned} &\theta_1[\pm x];\ (2 \times \tfrac{2}{3}\theta_2 + \tfrac{4}{3}\theta_2);\ (2\theta_2[\pm x, \pm y])_2;\ \textit{acquire} \\ &(2 \times \tfrac{2}{3}\theta_2 + \tfrac{4}{3}\theta_2);\ (2\theta_2[\pm x, \pm y])_2;\ \textit{acquire} \end{aligned} \tag{4.9}$$

where the gradient is turned off after the amplitude modulated selective inversion pulse θ_1 and the θ_2 pulses are broadband and scaled so that θ_2 is 90 degrees in the region of interest. The simulations indicate that the combination of selective excitation and depth pulses allows an isolated sensitive region to be defined, which is not possible with depth pulses alone for these coil designs.

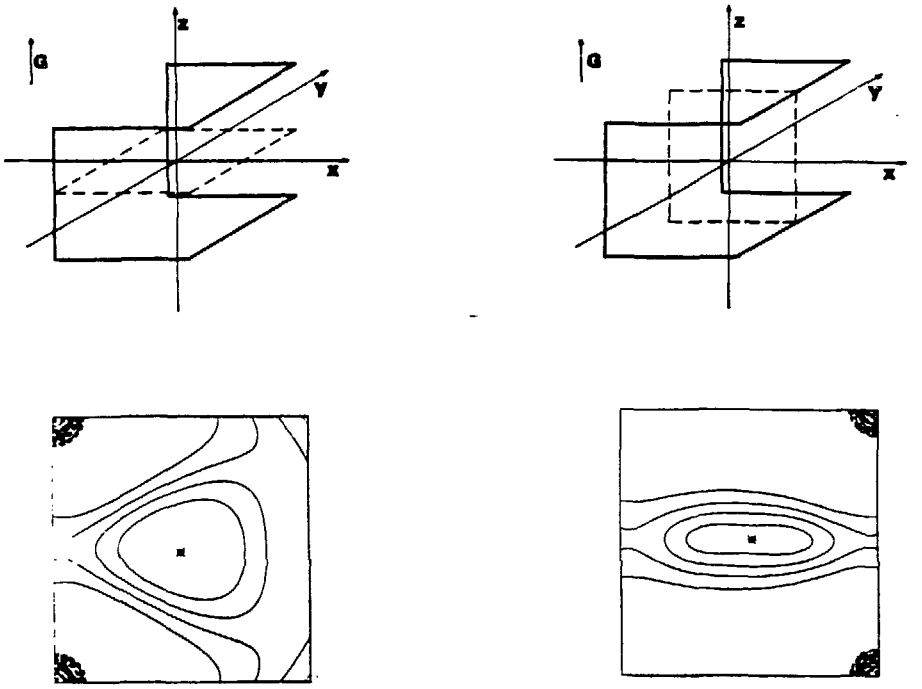

Figure 4.5: Combination of SHARP with depth pulses: the resulting sensitivity maps should be compared to Figure 4.1, in which a simple broadband pulse is simulated[36]. Significant improvement in spatial localization is seen.

5. Experiments

5(a) Numerical simulations

"Scientific laws are now being viewed as algorithms."
S. Wolfram

The numerical simulations concern basically two physical calculations: the first is the step-wise integration of the Bloch equations (2.16), while the second is a finite-element Biot-Savart computation (equation (4.1)). In both cases, the approximation of the continuous problem is checked with analytical results evaluated at the same (x,y,z) points.

As mentioned in chapter 3, the prolate spheroidal wave functions of interest are represented as discrete point values. To generate them, an efficient QR algorithm[17] is used, which specifically handles the eigenvalue/eigenvector computation for symmetric tridiagonal matrices. As the matrices provided in [19,21] are of this special form, we have the waveforms of interest as the eigenvectors of these matrices. We then assume that the modulations are these piece-wise constant functions, so that a fixed step ordinary differential

equations (ODE) integrator is needed.

We briefly describe the ODE solver for the Bloch equations. Neglecting relaxation, the Bloch equations (2.16) are written as a set of three first order coupled ordinary differential equations

$$\dot{\mathbf{M}}(t) = \mathbf{A}(t)\mathbf{M}(t) \tag{5.1}$$

where A(t) is the matrix of time-varying magnetic field components, containing the rf modulations of interest. If we approximate the time variation of the rf as a series of broken piece-wise constant steps h_j, over a given time step $\mathbf{A}(h_j)$ is constant. We immediately integrate (5.1)

$$\mathbf{M}(h_{j+1}) = e^{h_j \mathbf{A}(h_j)}\, \mathbf{M}(h_j) \tag{5.2}$$

The ODE solver for the Bloch equations is then a subroutine which computes the matrix $e^{h\mathbf{A}}$ at each step and, in applying this matrix to the magnetization position at the start of the step h, obtains the position of M at the end of the step.

The computation of $e^{h\mathbf{A}}$ at each step involves a well-known identity from rotation group theory

$$e^{h\mathbf{A}} = \mathbf{I} + (h\mathbf{A})^2 \frac{(1-\cos\,\theta)}{\theta^2} + h\mathbf{A}\frac{\sin\,\theta}{\theta} \tag{5.3}$$

where θ is the angle of rotation (about the rotating frame effective magnetic field (2.14)) with

$$\theta = h\,\sqrt{(\omega_1)^2 + (\gamma \mathbf{G}\cdot\mathbf{r})^2} \tag{5.4}$$

In this way, because A=B·I (where B is the applied magnetic field and I are the generators of SO(3) (2.23)), it is easy to compute

$$e^{hA} = \begin{pmatrix} b_1^2 + (b_2^2 + b_3^2)\cos\theta & b_1 b_2(1-\cos\theta) - b_3\sin\theta & b_1 b_3(1-\cos\theta) + b_2\sin\theta \\ b_1 b_2(1-\cos\theta) + b_3\sin\theta & b_2^2 + (b_1^2 + b_3^2)\cos\theta & b_2 b_3(1-\cos\theta) - b_1\sin\theta \\ b_1 b_3(1-\cos\theta) - b_2\sin\theta & b_2 b_3(1-\cos\theta) + b_1\sin\theta & b_3^2 + (b_1^2 + b_2^2)\cos\theta \end{pmatrix} \tag{5.5}$$

where

$$\mathbf{B} = \begin{pmatrix} b_1 \\ b_2 \\ b_3 \end{pmatrix} = \frac{1}{\sqrt{(\omega_1)^2 + (\Delta\omega)^2}} \begin{pmatrix} \omega_1 \cos\phi \\ \omega_1 \sin\phi \\ \Delta\omega \end{pmatrix} \tag{5.6}$$

and θ is obtained from (5.4).

From (5.5) we have an analytical expression for the response to a constant rf pulse. As the simulations assume for the initial position

$$\begin{pmatrix} M_x \\ M_y \\ M_z \end{pmatrix} = \begin{pmatrix} 0 \\ 0 \\ 1 \end{pmatrix} \tag{5.7}$$

we are able to compare the analytical expression for the (i=3,j=3) element in (5.5) to the simulated response for $M_z(\Delta\omega)$ at the end of a constant amplitude rf pulse.

For the coil computations, we demonstrate two cases. The simple loop in Figure 5.1 (of radius a and current j in the x-y plane) is approximated by 360 unit-length current

elements

$$\mathbf{l} = \begin{pmatrix} -a \sin \theta_i \\ a \cos \theta_i \\ 0 \end{pmatrix} \tag{5.8}$$

so that the integral (4.6) becomes the sum

$$\mathbf{B} = \mathrm{j} \sum_{i=1}^{360} \frac{1}{(\sqrt{(x - a \cos\theta_i)^2 + (y - a \sin\theta_i)^2 + z^2})^3} \begin{pmatrix} za \cos\theta_i \\ za \sin\theta_i \\ a^2 - xa \cos\theta_i - ya \sin\theta_i \end{pmatrix} \tag{5.9}$$

where we neglect the z component (along B_o). This is to be compared with the analytical formulas in [29].

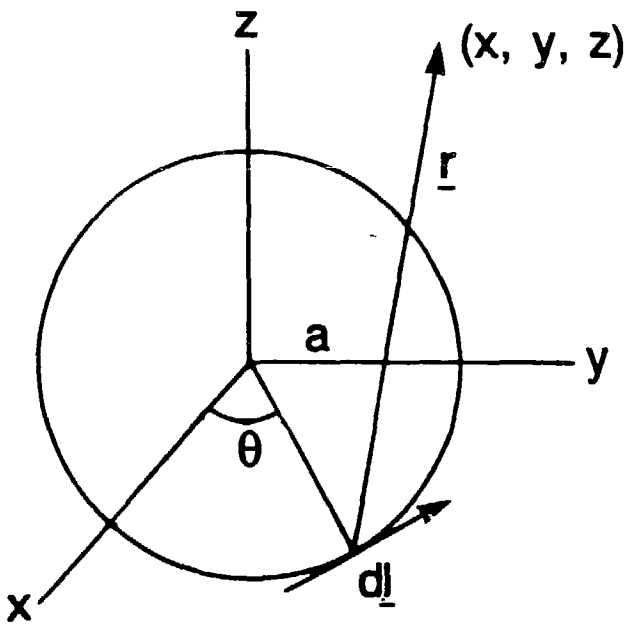

Figure 5.1:

The Biot-Savart Law integration for a coil in the x-y plane.

In the case where a coil can be constructed of line-segments, the magnetic field from a straight line current (of length 2L along $\hat{x}$) is easily computed in closed form: we have from Figure 5.2

$$\begin{aligned} d\mathbf{B} &= \mathrm{j}\ \tfrac{\mathrm{l}\times(\mathbf{x}-\mathbf{x}_\mathrm{l})}{|\mathbf{x}-\mathbf{x}_\mathrm{l}|^3} \\ &= \mathrm{j}\ \tfrac{r\ d\theta}{\sin\ \theta}\tfrac{r}{r^3}\sin\ \theta \\ &= \mathrm{j}\ \tfrac{d\theta}{r} \end{aligned} \tag{5.10}$$

so that, with R=$\sqrt{y^2+z^2}$ and r=$\sqrt{R^2+(x+L)^2}$,

$$\begin{aligned} \mathbf{B} &= \int d\mathbf{B} \\ &= \mathrm{j}\int_{\theta_1}^{\theta_2}\tfrac{d\theta}{r} \\ &= \tfrac{\mathrm{j}}{R}\int_{\theta_1}^{\theta_2}\sin\ \theta\ d\theta \\ &= \tfrac{\mathrm{j}}{R}(\cos\ \theta_1 - \cos\ \theta_2) \end{aligned} \tag{5.11}$$

where cos θ_1 and cos θ_2 are the geometric ratios

$$\cos\ \theta_1 = \frac{x+L}{\sqrt{(x+L)^2+y^2+z^2}},\ \cos\ \theta_2 = \frac{x-L}{\sqrt{(x-L)^2+y^2+z^2}} \tag{5.12}$$

Notice that the field has only components perpendicular to the wire segment; in this example

$$\mathbf{B} = \begin{pmatrix} 0 \\ \tfrac{\mathrm{j}}{R}(\cos\ \theta_1 - \cos\ \theta_2)\tfrac{z}{R} \\ \tfrac{\mathrm{j}}{R}(\cos\ \theta_1 - \cos\ \theta_2)\tfrac{y}{R} \end{pmatrix} \tag{5.13}$$

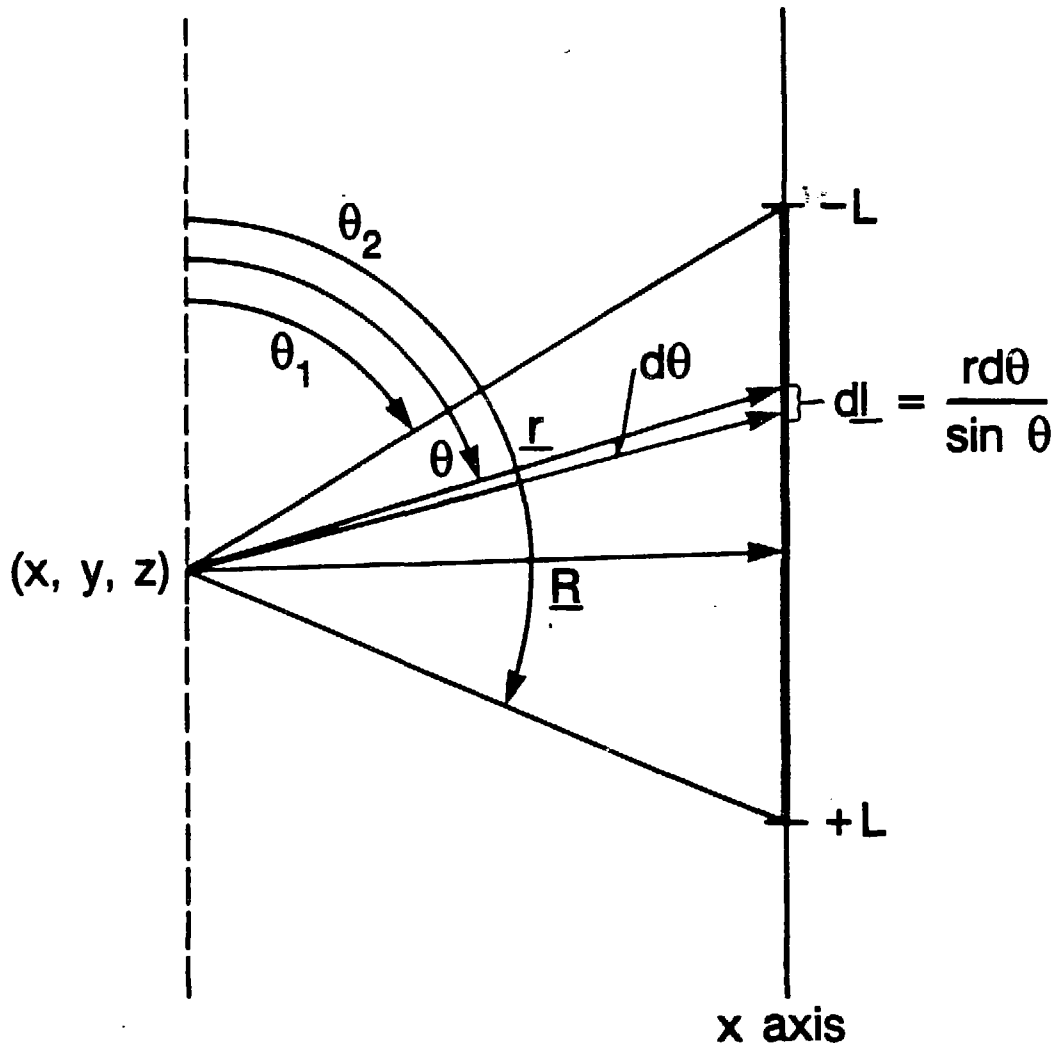

Figure 5.2:

The Biot-Savart Law integration for a wire segment along the x axis.

In both computations, a grid is then set up on which these subroutines run: for the pswf, one calculates the entire pulse for a range of resonance offset ($\Delta\omega$) values; for the spatial B_1 maps, a planar grid is placed in a simple geometric relation to the coil. Using

the integration (5.9), the values for the single coil were tabulated once on a fine mesh in a quarter plane perpendicular to the plane of the coil. Simple rotations of this quarter plane produced values near the sites of the desired image planar grid. In cases where the tabulated point values did not match the spatial map locations, linear interpolation was done on the four nearest point values in the table.

5(b) NMR phantom measurements

"Phenomenology is everything!"
M.P. Klein

Experiments were done on phantom samples to determine the degree of validity of the assumptions made above. The first set of experiments was done in collaboration with M.R. Bendall at Oxford Research Systems in England. The same experimental ideas were then implemented on the 0.5 Tesla NMR imager at LBL. The basic philosophy is to use a simple slice phantom to image the sensitive volume of various coil geometries. For the rf temporal modulations, a long sample (20 cm .1 mM $MgCl_2$ doped water filled test tube) was placed along a static gradient and, after selective excitation, the z component of the magnetization was interrogated with a hard (broadband) 50/100 μsec 90°/180° echo combination.

The measurements for discrete prolate spheroidal wave function amplitude modulated π pulses are shown in Figures 5.3 and 5.4. On the IBM/Oxford imager at LBL, the z gradient was 0.2 Gauss/cm, and a 5 msec dephasing delay was used prior to echo formation.

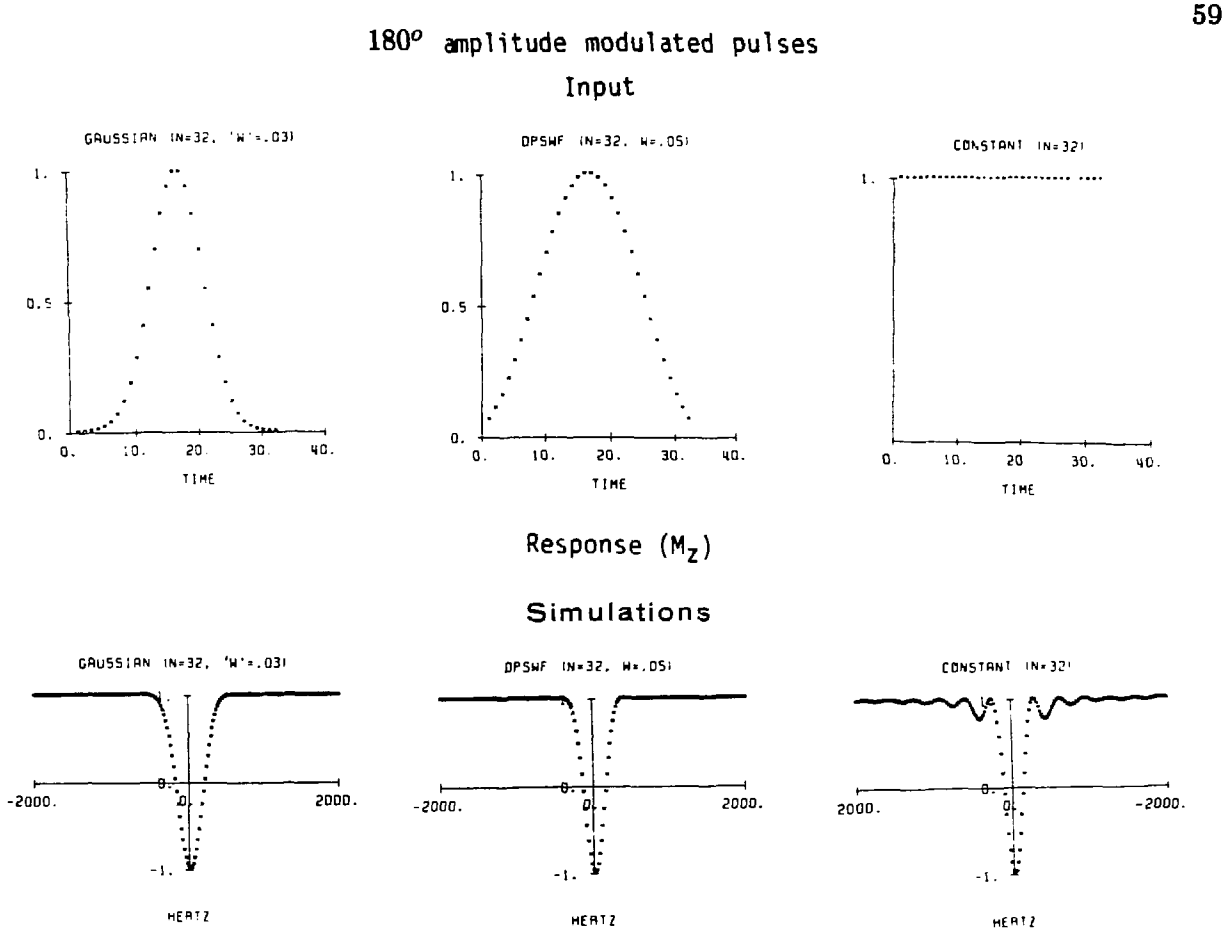

Figure 5.3: Experimetal comparison of three N=32 point temporal waveforms as π pulses. The use of the discrete pswf as π amplitude modulations, both in simulation and in measurement, is seen to be preferred to the use of either the gaussian on the left or the constant on the right (in columns).

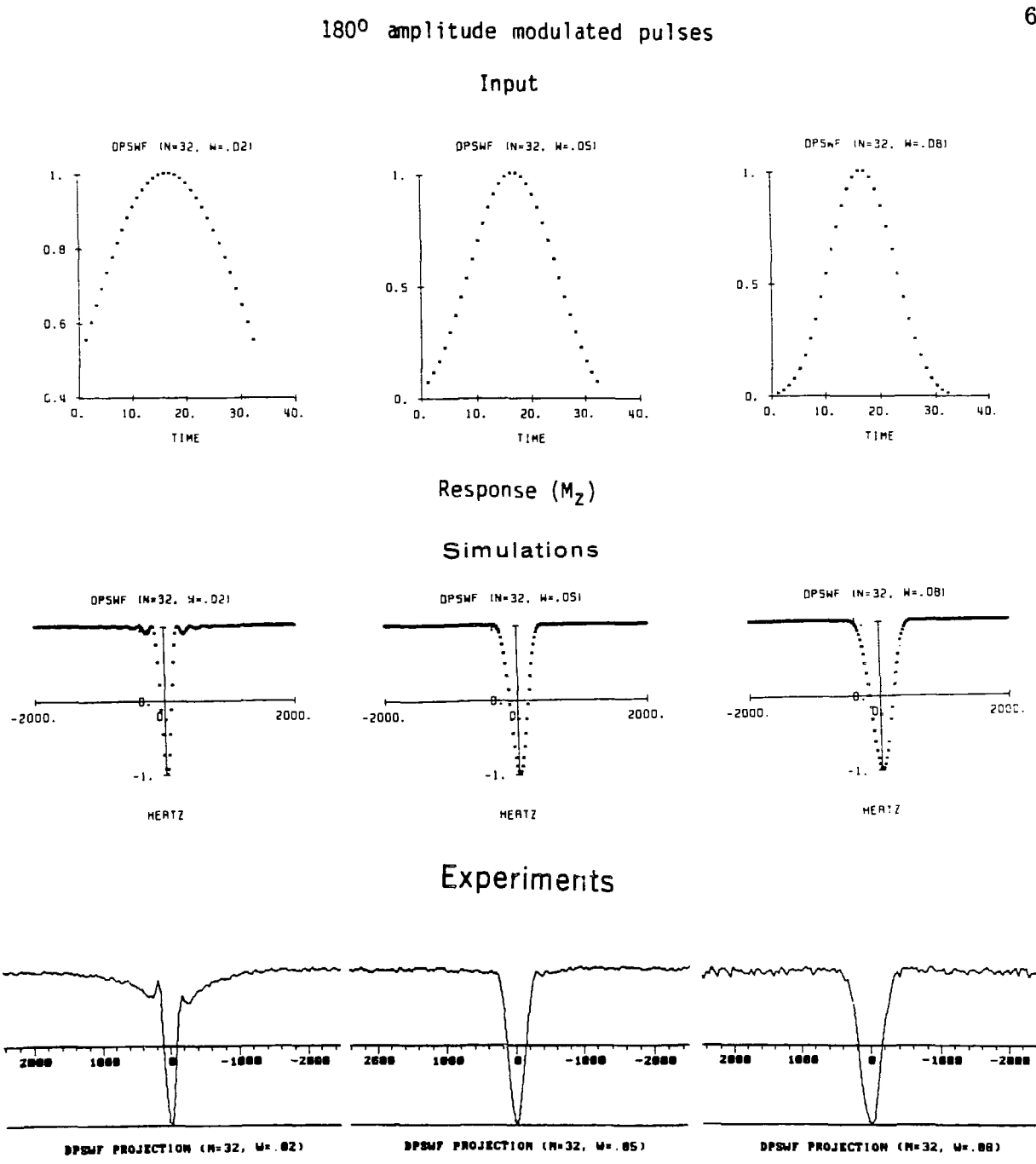

Figure 5.4: Further verification for the dpswf theory. As W (the frequency concentration variable) varies from .02 (left) to .05 (center) to .08 (right), the inversion bandwidth is seen to increase.

The sensitive volume of a square "baseball" coil was imaged at ^{31}P frequencies using a slice phantom of concentrated H_3PO_4 and a procedure employed at Oxford Research Systems which may be written schematically

$$\theta \; ------ \tau \; -------- \; 2\theta \; ------ \tau \; ------ \qquad (5.14)$$

incremented y gradient, and x gradient — acquisition x gradient

(The x gradient is adjusted to ensure that the top of the spin-echo occurs halfway through signal acquisition). The square "baseball" coil was constructed out of 3.2 mm diameter copper wire to a side length of 8.7 cm. A round slice phantom of diameter 11.8 cm and thickness 1.0 cm was used. As the diagonal length of the coil is 12.3 cm, the phantom fits just inside the limits of the coil wire. A θ pulse length in the range of 250 to 450 μsec was used at approximately 100 watts pulse power.

The scheme above would determine the sensitive volume for the depth pulse $\theta; 2\theta\ [\pm x, \pm y]$. The phase-cycling for the 2θ refocussing pulse is unnecessary for a homogeneous phantom when using pulsed field gradients[38,39]. For the depth pulse

$$(2\theta\ [\pm x])_2;\ \theta\ ;\ 2\theta\ [\pm x, \pm y], \qquad (5.15)$$

the sensitive volume was imaged by replacing θ in the imaging sequence by $(2\theta\ [\pm x])_2;\ \theta$. This depth pulse produces a signal from each volume element proportional to

$\theta \cos^2 2\theta \sin^3 \theta$, and so does not suppress the 270^o signal (as in the simulation shown above)[35,38,39]. Simulations and experimental results are shown in Figure 5.5.

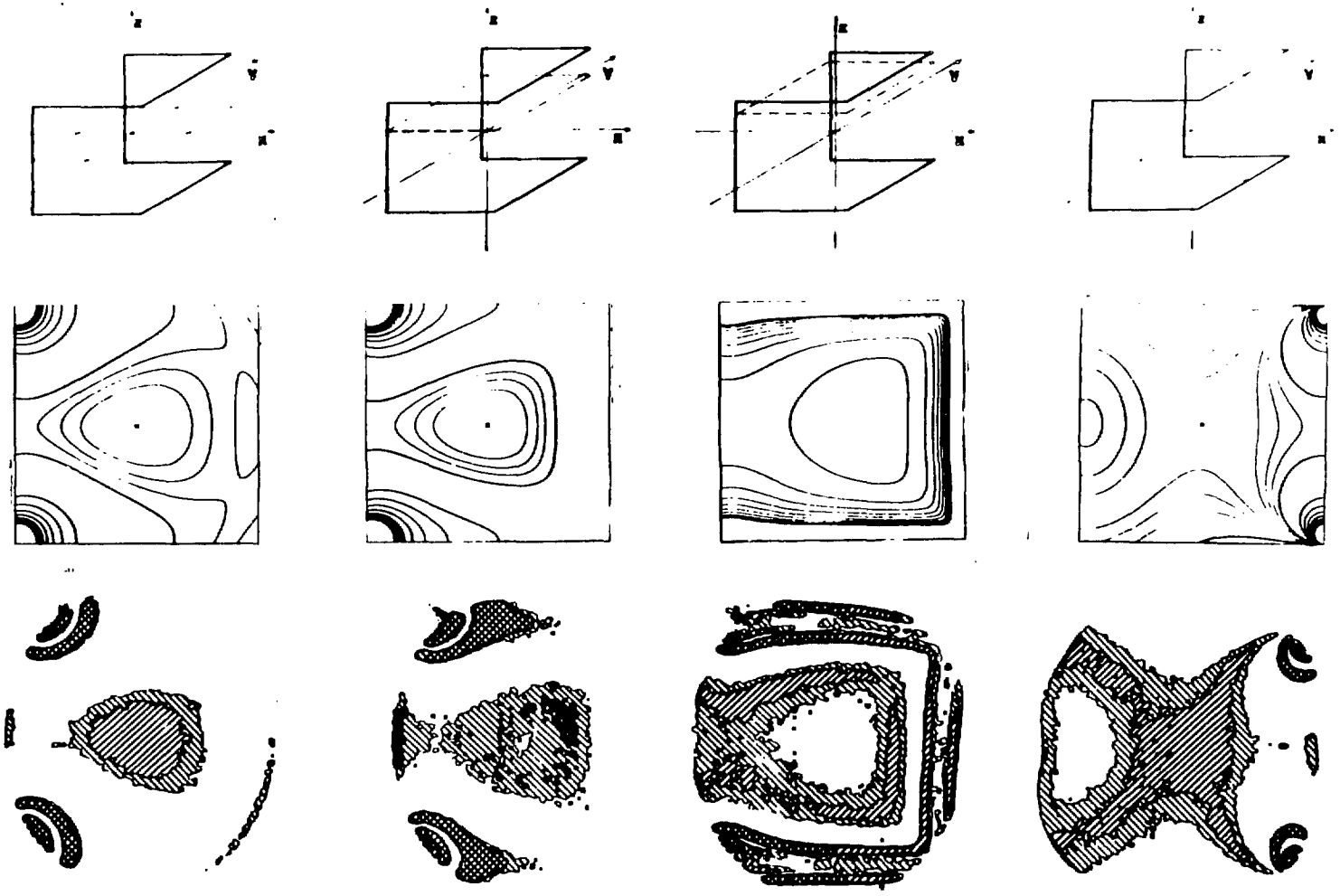

Figure 5.5: The magnitude of the signal induced by each volume element is shown for the simulations and experiments[36]. For the depth pulse $2\theta[\pm x]_2; \theta; 2\theta[\pm x, \pm y]$, the top row shows the location of the slice, the middle row the calculated sensitivity, and the bottom row the measured sensitivity. The experiments were done at Oxford Research Systems in England.

A 15 cm × 15 cm × .5 cm H_2O square slice phantom was built to map the field of a 10 cm diameter surface coil in the Oxford/IBM .5 T whole body magnet.[1] The coil was wound into a single turn of $\frac{1}{8}$ inch copper tubing, and the experiment utilized a 2DFT imaging sequence similar to (5.14), except that the 2θ echo pulse was replaced by an x gradient reversal. Figure 5.6 compares the measurement with a simulation.

[1]Thanks to Mirko Hrovat of IBM Instrumenmts, Inc.

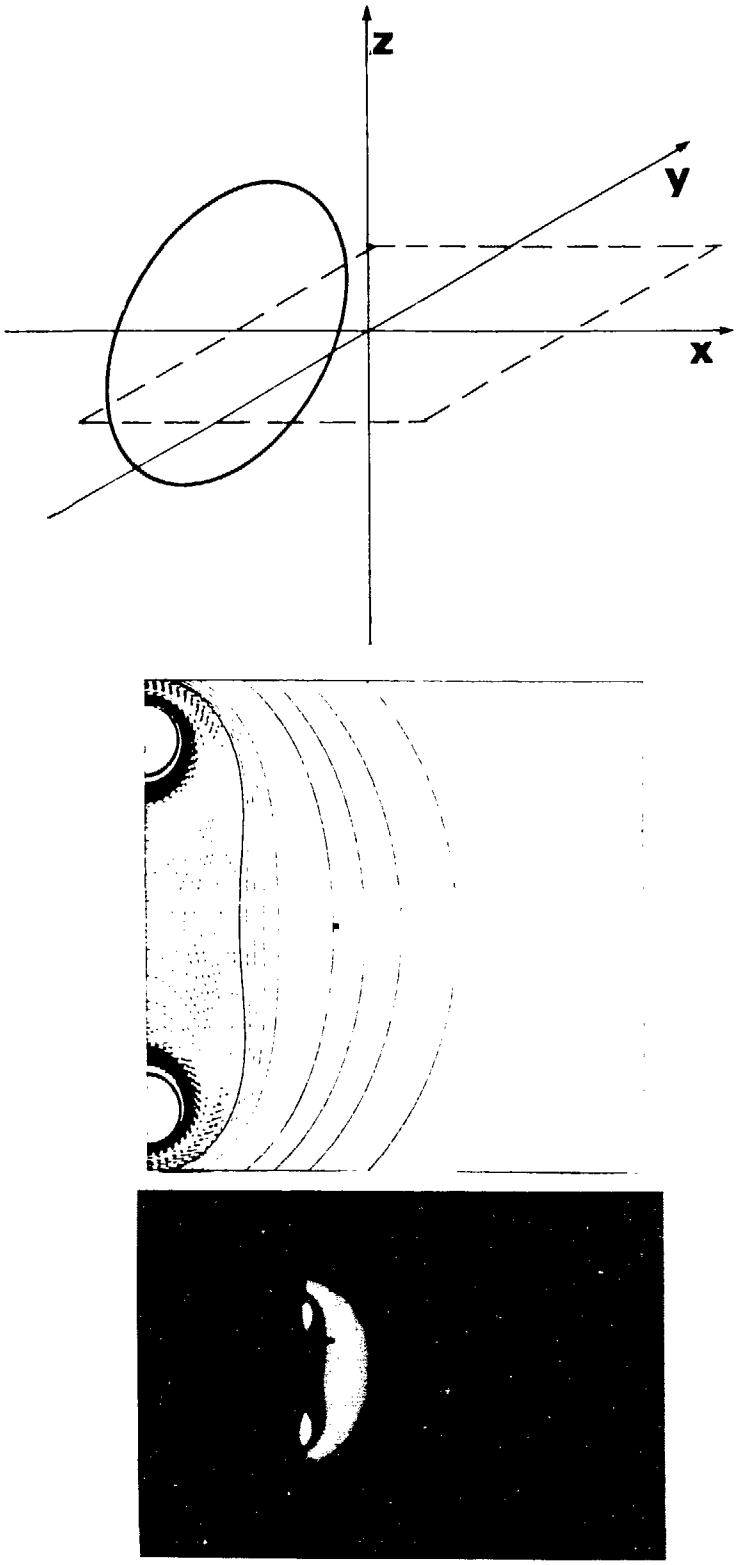

Figure 5.6: Experimental results of spatial maps of surface coil (similar to Figure 5.5) is displayed. The geometry is at the top, followed by a contour plot, and finally a photo of the 2D experimental image.

5(c) Two theorems

"It all goes back to Gauss."
F.A. Grünbaum

In performing numerical simulations of the MIBE, some regularities in the results were apparent. We now state these as theorems in regard to our method of integration. Both concern amplitude modulated pulses, so that the matrix in (5.5) simplifies to

$$e^{hA} = \begin{pmatrix} b_1^2 + b_3^2\cos\theta & -b_3\sin\theta & b_1 b_3(1-\cos\theta) \\ b_3\sin\theta & (b_1^2+b_3^2)\cos\theta & -b_1\sin\theta \\ b_1 b_3(1-\cos\theta) & b_1\sin\theta & b_3^2 + b_1^2\cos\theta \end{pmatrix} \tag{5.16}$$

In the first case, we noticed that the response $M_x(\Delta\omega)$ is symmetric for $b_3 = \pm\Delta\omega$. As our simulations approximate $\omega_1(t)$ by an N-piecewise constant curve, the Bloch evolution becomes a product of rotation matrices applied to $\mathbf{M}(t=0,\Delta\omega)$ in (5.7). The second theorem concerns the final position of $M_x(\Delta\omega)$ obtained from the two pulses $\omega_1(t)$ and $\omega_1(T-t)$, for $t \in [0,T]$, and is called the Backward Pulse Theorem [2]

We now state, and then prove, these two theorems.

Theorem 1 $< e, R_N^+ R_{N-1}^+ ... R_1^+ e > = < e, R_N^- R_{N-1}^- ... R_1^- e >$

where e denotes the initial condition (5.7), the bracket <> denotes inner product, and

$$R_j^+ = e^{h_j(\omega_1^j\ I_x + \Delta\omega\ I_z)}\ ,\ R_j^- = e^{h_j(\omega_1^j\ I_x - \Delta\omega\ I_z)} \tag{5.17}$$

[2] I am indebted to Arnold Lent of Technicare, Inc. for helpful advice.

with ω_1^j the j^{th} point value of ω_1 and h_j the j^{th} "time step".

Theorem 2 $< e, R_N R_{N-1} ... R_1 e > = < e, \tilde{R}_N \tilde{R}_{N-1} ... \tilde{R}_1 e >$

where

$$R_j = e^{h_j(\omega_1(t)\ I_z + \Delta\omega\ I_z)}\ ,\ \tilde{R}_j = e^{h_j(\omega_1(T-t)\ I_z + \Delta\omega\ I_z)} \tag{5.18}$$

Proofs of both of these statements follow directly from properties of the rotation matrices R_j. To prove Theorem 1, we notice that

$$R_j^+ = X^{-1} R_j^- X \tag{5.19}$$

where

$$X = \begin{pmatrix} -1 & 0 & 0 \\ 0 & 1 & 0 \\ 0 & 0 & 1 \end{pmatrix} = X^{-1} \tag{5.20}$$

Thus, we compute

$$\begin{aligned} < e, R_N^+ R_{N-1}^+ ... R_1^+ e > &= < e, X^{-1} R_N^- X X^{-1} R_{N-1}^- X ... X^{-1} R_1^- X e > \\ &= < Xe, R_N^- R_{N-1}^- ... R_1^- X e > \\ &= < e, R_N^- R_{N-1}^- ... R_1^- e > \end{aligned} \tag{5.21}$$

Q.E.D.

For Theorem 2, we first prove a lemma about rotations

Lemma 1 *Let $R(\mathrm{u},\theta)$ be the rotation of angle θ about* u. *Let u', u'' be any two vectors perpendicular to* u *such that*

$$\mathrm{R}(\mathbf{u},\tfrac{\theta}{2})\ u' = u''$$

Then

$$\mathrm{R}(\mathbf{u},\theta) = \mathrm{M}(u')\mathrm{M}(u'')$$

where $M(u')\mathbf{x} = \mathbf{x}\text{-}2(u'\cdot\mathbf{x})u'$ *(i.e., R can always be expressed as a product of reflections in the plane spanned by* $(u', u' \times u'')$ *or* $(u'', u' \times u'')$*, and denoted by* $M(u')$ *or* $M(u'')$*).*

Proof Consider the case $\mathbf{u}=\hat{z}$. Then u', u'' are vectors in the x-y plane

$$\mathbf{u}' = \begin{pmatrix} 1 \\ 0 \end{pmatrix}, \ \mathbf{u}'' = \begin{pmatrix} \cos(\frac{\theta}{2}) \\ \sin(\frac{\theta}{2}) \end{pmatrix} \tag{5.22}$$

so

$$M(\mathbf{u}') = \begin{pmatrix} -1 & 0 & 0 \\ 0 & 1 & 0 \\ 0 & 0 & 1 \end{pmatrix}, \ M(\mathbf{u}'') = \begin{pmatrix} -\cos\theta & -\sin\theta & 0 \\ -\sin\theta & \cos\theta & 0 \\ 0 & 0 & 1 \end{pmatrix} \tag{5.23}$$

and so that

$$M(\mathbf{u}')M(\mathbf{u}'') = \begin{pmatrix} \cos\theta & -\sin\theta & 0 \\ \sin\theta & \cos\theta & 0 \\ 0 & 0 & 1 \end{pmatrix} = R(\hat{z},\theta) \tag{5.24}$$

The general case $\mathrm{R}(\mathbf{w},\theta)$ is now obtained by conjugation of the matrix $\mathrm{R}(\mathbf{u}\times\mathbf{w},\cos^{-1}(\mathbf{u}\cdot\mathbf{w}))$.

Q.E.D.

We can now use this lemma to prove Theorem 2. Since in (5.18) the matrix R_j is a rotation about an axis in the x-z plane, we can always choose $u'=\hat{y}$ so that

$$R_j = M(\mathrm{u}'')M(\hat{y}) \equiv M_1 M_2 \tag{5.25}$$

But as $(M_2)^2$=I,

$$R_j^{-1} = M_2 M_1 (M_2)^2 = M_2 R_j M_2 \tag{5.26}$$

and

$$M_2 = \begin{pmatrix} 1 & 0 & 0 \\ 0 & -1 & 0 \\ 0 & 0 & 1 \end{pmatrix} \tag{5.27}$$

so that

$$R_j^{-1} = \begin{pmatrix} 1 & 0 & 0 \\ 0 & -1 & 0 \\ 0 & 0 & 1 \end{pmatrix} R_j \begin{pmatrix} 1 & 0 & 0 \\ 0 & -1 & 0 \\ 0 & 0 & 1 \end{pmatrix} \equiv M_2 R_j M_2 \tag{5.28}$$

We thus compute

$$< e, R_N R_{N-1} ... R_1 e > = < R_1^T ... R_{N-1}^T R_N^T e, e > \tag{5.29}$$

but as R_j is unitary

$$\begin{aligned} < R_1^T ... R_{N-1}^T R_N^T e, e > &= < R_1^{-1} ... R_{N-1}^{-1} R_N^{-1} e, e > \\ &= < M_2 R_1 M_2 ... M_2 R_{N-1} M_2 M_2 R_N M_2 e, e > \\ &= < R_1 ... R_{N-1} R_N M_2 e, M_2 e > \\ &= < \tilde{R}_N \tilde{R}_{N-1} ... \tilde{R}_1 e, e > \end{aligned} \tag{5.30}$$

Q.E.D.

6. Is the Bloch Transform Invertible?

6(a) Motivation

One of the essential features of biomedical NMR is the use of linear gradients in the main field B_o to encode spatial information. In chapter 3, we have formulated a transformation (the Bloch Transform, denoted $\mathcal{B}$) that, under conditions of an applied linear gradient, relates the rf waveform in the time domain to the final position of the magnetization after the pulse. As the final desired position of $\mathbf{M}(\Delta\omega)$ is known *a priori*, if we could invert the Bloch Transform, we would be able to find the needed rf modulation.

The basic problem, however, is that the Bloch Transform represents integration of the nonlinear Bloch equations (2.16), and so is a nonlinear mapping. We therefore try to reformulate the inversion problem for the Bloch Transform in terms of a better studied one. Specifically, we will attempt to turn this NMR inverse problem for the Bloch Transform into an inverse problem in the quantum theory of scattering. We choose to study a particular nonlinear evolution equation called the Korteweg-de Vries equation (KdV), in which a

series of mathematical arguments leads to the solution of this nonlinear problem[40]. The relevance to the Bloch inverse problem is then found by rewriting the Bloch equations in a form similar to the time-independent Schrödinger equation, which enters in the solution of the KdV equation.

An important complementary aspect of this Bloch inverse problem should be mentioned. We have already noted that real rf pulses are finite digital signals. In developing a general theory of rf excitation for *in vivo* NMR, it would be useful to generate the pulses from a suitable family of functions (preferably spanning $L^2([0,t_p])$ - the space of square integrable functions on the interval $[0,t_p]$) representing the harmonics present. Indeed, we have devoted section 3(e) to this topic, and in that comparison of gaussians to the pswf, one of the strengths of the prolate spheroidal wave functions is this property. But the pswf come from linear Fourier theory, whereas the problem really deals with the nonlinear Bloch equations, and so one would really like to find the appropriate nonlinear modes within which to express the desired localized response. Since solitons are naturally nonlinear modes, one should not be surprised to find solitons appearing in the solution, as discussed later.

6(b) The inverse scattering transform

> *"As a working physicist, I am acutely aware of the fact that the marriage between mathematics and physics, which was so enormously fruitful in past centuries, has recently ended in divorce."*
>
> F.J. Dyson

The recent revolution in mathematics known as soliton (or inverse scattering) theory, in addition to having inspired the development of some sophisticated and elegant tools for theorists, offers some real insights into the nonlinear behavior of simple physical systems. This series of discoveries has been paralleled by many observations of physical phenomena that are well described by these nonlinear evolution equations. We face here a nonlinear evolution problem, called the Bloch Transform inverse problem, and it is natural to ask whether these recent developments are applicable to our biomedically motivated inverse problem. In particular, the phenomenon of self-induced transparency[41], which involves the coupled Bloch-Maxwell equations, can be well described by some of this machinery[42].

The purpose of this section is to give a quick review of the inverse scattering transform which will be adequate for our purposes. For more detailed accounts one can consult [43-45]. In the next section we will indicate how the inversion of the Bloch Transform can be expressed in terms of the material in this section. We will be using only the Korteweg-de Vries equation in an exploration of the properties of the direct Bloch Transform. For this reason we limit our discussion below to the way in which the inverse scattering transform handles the KdV equation.

The solution of the KdV equation

$$q_t + 6qq_x + q_{xxx} = 0 \tag{6.1}$$

involves treating the function q as the potential in a time-independent Schrödinger equation

$$\psi_{xx} + (\lambda^2 + q(x,t))\psi = 0 \tag{6.2}$$

(the time variable in the Schrödinger equation is a separate parameter from the time t in the KdV equation) with stationary potential V(x)=-q(x,t) and energy $E=\lambda^2$. One asks the question: how do the eigenvalues $\lambda(t)$ and eigenfunctions $\psi(x,t)$ evolve if the potential satisfies the KdV equation (6.1)? By explicit computation, the discrete eigenvalues ($-\lambda_n^2 < 0$, n=1,...,N) for the bound eigenstates ($\lambda_n = -i\lambda$ so that $\lambda_n > 0$ is real and positive)

$$\begin{aligned} \psi_n &\sim e^{\lambda_n x} \qquad as\ x \to -\infty \\ &\sim b_n(t)e^{-\lambda_n x} \quad as\ x \to \infty \end{aligned} \tag{6.3}$$

are constants of the motion, and imposing on the scattering states ψ (i.e., $\lambda^2 > 0$) the boundary conditions

$$\begin{aligned} \psi &\sim e^{-i\lambda x} \qquad\qquad\qquad as\ x \to -\infty \\ &\sim a(\lambda,t)e^{-i\lambda x} + b(\lambda,t)e^{i\lambda x} \quad as\ x \to \infty \end{aligned} \tag{6.4}$$

one finds that $a(\lambda,t)$ and $b(\lambda,t)$ obey the trivial evolutions

$$a(\lambda,t)_t = 0\ ,\ b(\lambda,t)_t = 8i\lambda^3 b(\lambda,t) \tag{6.5}$$

The boundary conditions (6.4) have a standard interpretation in quantum physics as corresponding to a scattering problem in which a wave of amplitude a is incident from x=∞ on the potential V(x). The wave is transmitted to $-\infty$ with an amplitude of unity, and is reflected with amplitude b. The reflection and transmission coefficients for this scattering problem (6.4) are just

$$R_r(\lambda) = \frac{b(\lambda)}{a(\lambda)}, \; T_r(\lambda) = \frac{1}{a(\lambda)} \tag{6.6}$$

(the subscript r denotes an incident wave from the right) so that using (6.5) we find that the transmission coefficient is a constant of the motion and the reflection coefficient evolves by merely changing its phase linearly with time. The solution of the KdV equation at time t is then found by inverting the scattering data to find the potential $\sqrt{(x)}$ at time t, a problem which involves a linear integral equation (the Gel'fand-Levitan-Marchenko equation). Schematically, we denote this "change of variables" from potential to scattering data S=$\{(\lambda_n, b_n)_1^N; R_r(\lambda), \lambda \text{ real}\}$ and back as

$$\begin{array}{ccc} q(x,0) & \xrightarrow{\text{direct transform}} & S(0) \\ & & \Big\downarrow \text{time evolution of sc. data} \\ q(x,t) & \xleftarrow{\text{inverse transform}} & S(t). \end{array}$$

We shall rewrite the Bloch equations in (quasi)-Schrödinger form, and so, by relating the final position of the magnetization M($\Delta\omega$,T) to the reflection and transmission coefficients (6.6), would like to use this set-up to invert the Bloch Transform. Other nonlinear

evolutions besides the KdV can be handled in the same way, by an appropriate change of the time evolution of the scattering data.

One point on notation: from here on, we shall overscore the KdV variables $(\bar{x}, \bar{t})$ to remind the reader to separate the KdV evolution from the Schrödinger evolution in (x,t).

6(c) Reformulating the Bloch Transform as a scattering problem

> *"Nonlinear ordinary and partial differential equations do not, in general, admit explicit solutions, because the solutions of the typical nonlinear equation are so wildly irregular that they could not possibly be represented by known functions. Conversely, nonlinear equations with very well-behaved solutions should be expected to have uncommon properties."*
>
> H. Flaschka and A.C. Newell

From the MIBE for pure amplitude modulation

$$\frac{d}{dt}\begin{pmatrix} M_x \\ M_y \\ M_z \end{pmatrix} = \begin{pmatrix} 0 & \Delta\omega & 0 \\ -\Delta\omega & 0 & \omega_1(t) \\ 0 & -\omega_1(t) & 0 \end{pmatrix}\begin{pmatrix} M_x \\ M_y \\ M_z \end{pmatrix} \tag{6.7}$$

describing the motion of a 3-vector **M** under the applied magnetic field

$$\gamma\begin{pmatrix} B_x \\ B_y \\ B_z \end{pmatrix} = \begin{pmatrix} \omega_1 \\ 0 \\ \Delta\omega \end{pmatrix} \tag{6.8}$$

and with $\mathbf{M}(\Delta\omega,0)=(0,0,-1)^T$, we would like to find the appropriate rf waveform $\omega_1(t)$ to achieve a given final configuration of $\mathbf{M}(\Delta\omega,T)$, after a finite pulse (i.e., $t \in [0,T]$). In particular, one would like to explain the phenomenon observed using the complex secant pulse of Silver, Joseph, and Hoult[46]. An explanation might be possible by generalizing the results of this chapter, which considers only amplitude modulation, to frequency-modulated pulses.

Because the length of $\mathbf{M}$ is preserved

$$M_x^2 + M_y^2 + M_z^2 = 1 \tag{6.9}$$

the time development of $\mathbf{M}$ is a path on the sphere S^2. By defining ϕ to be the stereographic projection of $\mathbf{M}$ onto the y-z plane from the positive x-axis (1,0,0), we find using (6.7) that

$$\phi(\Delta\omega,t) = \frac{M_z + iM_y}{M_x - 1} \tag{6.10}$$

satisfies a Riccati equation[47]

$$\dot{\phi} = i\omega_1\phi + \frac{i\Delta\omega}{2}(\phi^2 - 1) \tag{6.11}$$

where ω_1 is the unknown rf field amplitude modulation.

The change of variables[48]

$$g(\Delta\omega,t) = e^{\frac{-i}{2}\int_{-\infty}^{t}(\Delta\omega\phi(\Delta\omega,t') + \omega_1(t'))\,dt'} \tag{6.12}$$

in (6.11) yields the second order differential equation

$$\ddot{g} + \frac{1}{4}(\Delta\omega^2 + \omega_1^2 + 2i\dot{\omega}_1)\,g = 0 \tag{6.13}$$

in Schrödinger (Liouville) form.

By viewing t as a position variable $\bar{x}$, equation (6.13) has the form of a "time-independent" Schrödinger equation

$$\frac{d^2}{d\bar{x}^2}g + (\lambda^2 - V)g = 0 \tag{6.14}$$

where the potential V contains the unknown field modulation ω_1 and its first derivative

$$V = -\frac{1}{4}(\omega_1^2 + 2i\dot{\omega}_1) , \lambda = \frac{\Delta\omega}{2} \tag{6.15}$$

The formulation is now clear from the standpoint of inverse scattering: the conditions under which the potential V in (6.14) can be reconstructed from asymptotic scattering data of g (i.e., reflection and transmission coefficients plus bound states and normalization constants) are known, starting from the work of Gel'fand-Levitan; for a recent account see [49]. Our original problem of finding ω_1 to yield a desired M($\Delta\omega$,T) can thus be solved using the techniques of inverse scattering if the asymptotic scattering data of g can be related to the known desired response M($\Delta\omega$,T), as we can then reconstruct V in (6.15), and thus obtain ω_1.

We therefore consider g in (6.12). (NB: we identify the Bloch evolution variable t in (6.7) with the spatial parameter $\bar{x}$ in the KdV equation (6.1). We further overscore the KdV parameters to remind the reader, and state that we are replacing the interval [0,T] here with $[-\infty, \infty]$.) The initial condition is that the spin population is at equilibrium, M_z=-1, and so, using (6.9) and (6.10), ϕ=1. Consequently, since the potential V $\rightarrow$ 0 as $\bar{x}(= t) \rightarrow -\infty$, g$\sim e^{-i\lambda t}$. Likewise, as t $\rightarrow \infty$ again V $\rightarrow$ 0, so that the passage of the

pulse $\omega_1(t)$ amounts to g from (6.12) becoming a linear combination

$$g(\lambda,t) \sim a(\lambda)\, e^{-i\lambda t} + b(\lambda)\, e^{i\lambda t} \tag{6.16}$$

and so, in general, the NMR observables will be left ringing at frequency λ. Hence, the inverse problem for the Bloch Transform is closely related to the scattering problem for ψ in (6.4).

But as t $\rightarrow \infty$,

$$g(\lambda,t) \sim e^{-i\lambda \int_{-\infty}^{t} \phi(\lambda,t')dt'} e^{\frac{-i}{2}\int_{-\infty}^{\infty} \omega_1(t')\ dt'} \tag{6.17}$$

The second factor is known, as $\int_{-\infty}^{\infty} \omega_1$ is just the total desired flip angle (i.e., typically a $\pi/2$ or π pulse).

Therefore the asymptotics of g(λ,t) for large t can be obtained from the function

$$\int_{-\infty}^{t} \phi(\lambda,t')\ dt' \tag{6.18}$$

One could thus use (6.16) to recover a(λ) and b(λ) if one knew ϕ(λ,t) for all t. However, since only $\mathbf{M}(\Delta\omega,\mathrm{T})$ is available, it is clear that this approach cannot be used directly to achieve the inversion of the Bloch Transform. See, however, section 6(f).

6(d) 2πN-solitons

Although this formulation of the inverse problem for the Bloch Transform would appear useless in view of the comments at the end of the previous section, we can use it to suggest

interesting inputs to the direct problem. In particular, we notice from (6.9) and (6.10) that the condition M_z=-1 is equivalent to ϕ=1 (independent of t!). Thus, using (6.12) g$\sim e^{-i\lambda t}$ even as t $\rightarrow \infty$, implying from (6.16) that b(λ)=0. Thus in this case of reflectionless potentials[50], one can use the ansatz (assumption arising from (6.15))

$$\omega_1(t) = \sqrt{V(x)} \tag{6.19}$$

and take for V a "pure soliton potential". We proceed to numerically integrate equations (6.7) according to the procedure introduced in section 5(a). The results shown in Figures 6.1-6.3 display some remarkable properties.

The surprising feature of the simulations is that in this case of N-soliton pulses one has control over the inverting properties obtained, even though the Bloch Transform is nonlinear in the regime where population inversions are effected. In the cases when the flip angle (6.26) are 2π and 6π, one achieves localized inversions for different ranges of $\Delta\omega$, and in the 4π case, complete return to equilibrium is obtained independent of $\Delta\omega$! One can say that these N-soliton pulses are thus nonlinear modes of rf excitation.

We briefly outline the computation of the N-soliton potential. We begin by computing the determinant of the matrix

$$A_{ij} = \delta_{ij} + \frac{b_i}{\lambda_i + \lambda_j} e^{-(\lambda_i+\lambda_j)x} \tag{6.20}$$

The potential V(x) is then computed from

$$\begin{aligned} V(x) &= \tfrac{-2}{a^2}(a\tfrac{d^2a}{dx^2} - (\tfrac{da}{dx})^2) \\ &= -2\tfrac{d^2 ln\ det(A)}{dx^2} \end{aligned} \tag{6.21}$$

where a=det(A). The time dependence is then put in using (6.5). For the case N=2, we find

$$V_{up} \equiv \lambda_2^2 \cosh(2\lambda_1\overline{x} - 8\lambda_1^3\overline{t} + \phi_1 - \phi_2) + \lambda_1^2 \cosh(2\lambda_2\overline{x} - 8\lambda_2^3\overline{t} + \phi_1 + \phi_2) + \lambda_2^2 - \lambda_1^2 \tag{6.22}$$

and

$$V_{down} \equiv \frac{\lambda_2 - \lambda_1}{\lambda_2 + \lambda_1} \cosh((\lambda_2+\lambda_1)\overline{x} - 4(\lambda_2^3+\lambda_1^3)\overline{t} + \phi_1) + \cosh((\lambda_2-\lambda_1)\overline{x} - 4(\lambda_2^3-\lambda_1^3)\overline{t} + \phi_2) \tag{6.23}$$

so that

$$V(\overline{x},\overline{t}) = -4\frac{(\lambda_2 - \lambda_1)V_{up}}{(\lambda_2 + \lambda_1)V_{down}^2} \tag{6.24}$$

where ϕ_1, ϕ_2 are the (free) parameters

$$\phi_1 = \frac{1}{2} ln\ \frac{\lambda_1\lambda_2}{b_1 b_2} + ln\ 2\frac{\lambda_1 + \lambda_2}{\lambda_1 - \lambda_2}\ ,\ \phi_2 = \frac{1}{2} ln\ \frac{\lambda_1 b_2}{b_1 \lambda_2} \tag{6.25}$$

See [40] for details.

Narrative for Figures 6.1, 6.2, and 6.3

We begin with the top diagram in each Figure. From (6.24), we have an explicit form for the N=2 soliton potential. We evaluate this expression for V on a 50×50 $(\bar{x}, \bar{t})$ grid, thus computing the 50 vectors $V(\bar{x}), \bar{t}$=constant.

According to the ansatz (6.19), we then use each of these 50 wave profiles in a Bloch ODE solver[20], numerically integrating (6.7). As the output of the ODE simulation is the vector **M** after the pulse, we display in the bottom figure the excited z component as a function of $\Delta\omega$. For convenience we display $-M_z$. The 50 waveforms are each separately scaled so that the flip angle is

$$\int_{-\infty}^{\infty} \omega_1(t)\, dt \;=\; 2\pi k \quad (k = 1, 2, 3) \tag{6.26}$$

The bottom figure therefore simulates the result of 50 independent NMR experiments labelled by the parameter $\bar{t}$.

The only differences between Figures 6.1, 6.2, and 6.3 are:

1. In Figures 6.2 and 6.3, we run in KdV time out to $\bar{t} = \pm\ .4$, and
2. we scale the waveforms in Figures 6.1, 6.2, and 6.3 using (6.26) to be $2\pi, 4\pi$, and 6π, respectively.

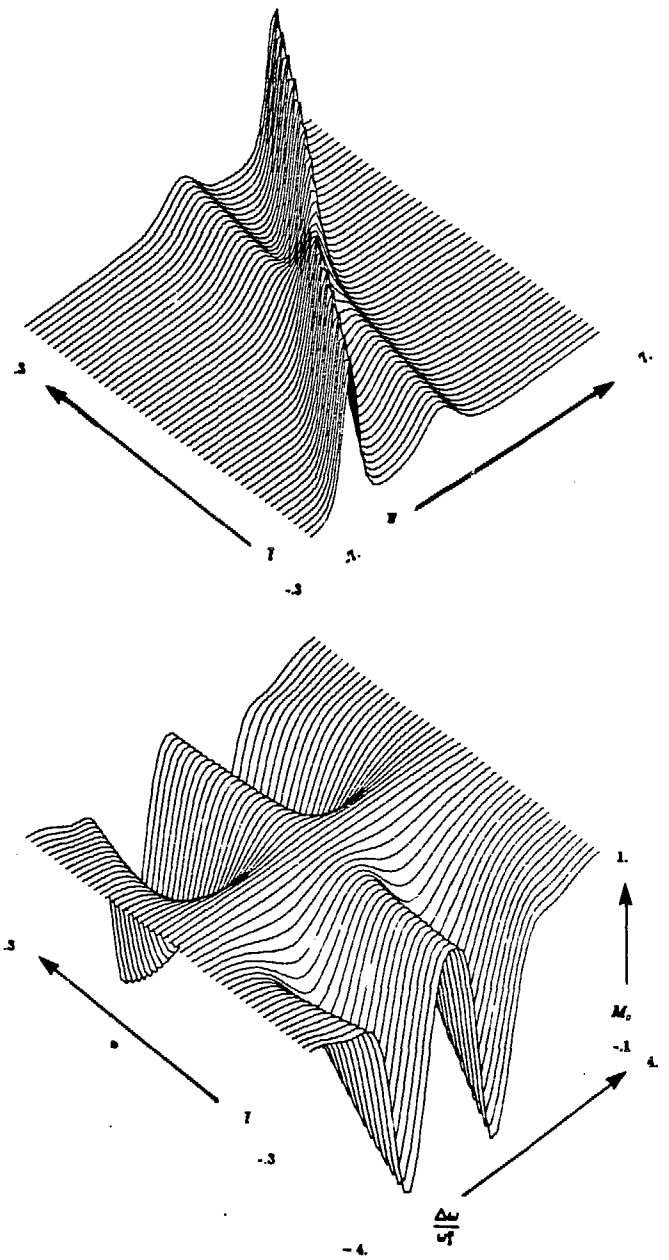

Figure 6.1: The case N=2. Each of the 50 wave profiles in the two soliton solution $V(\bar{x})$, $\bar{t}$=constant in the top plot is used as an amplitude modulated $\underline{2\pi}$ pulse in the bottom plot, where the z component of the magnetization is displayed as a function of $\frac{\Delta\omega}{\omega_1^o}$ after the pulse[51].

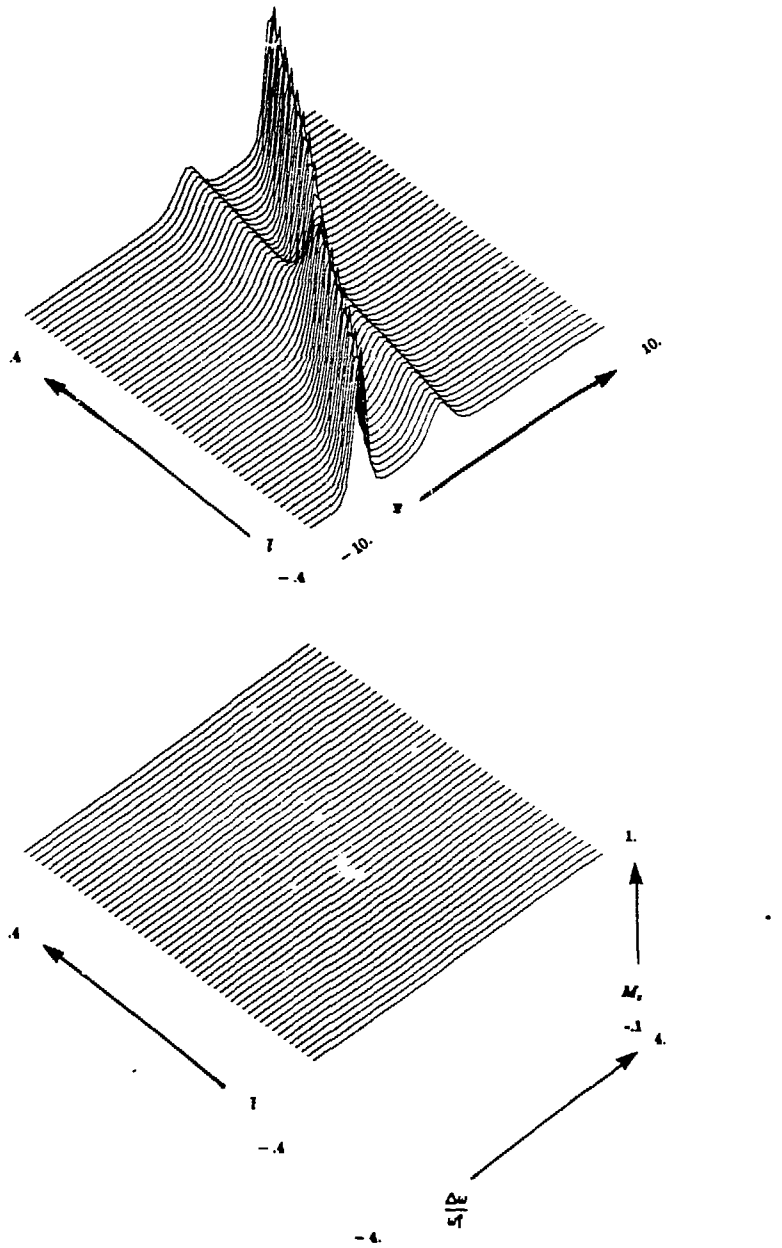

Figure 6.2: The case N=2. Each of the 50 wave profiles in the two soliton solution $V(\tau)$, $\bar{t}$=constant in the top plot is used as an amplitude modulated $\underline{4\pi}$ pulse in the bottom plot, where the z component of the magnetization is displayed as a function of $\frac{\Delta\omega}{\omega_1^0}$ after the pulse[51].

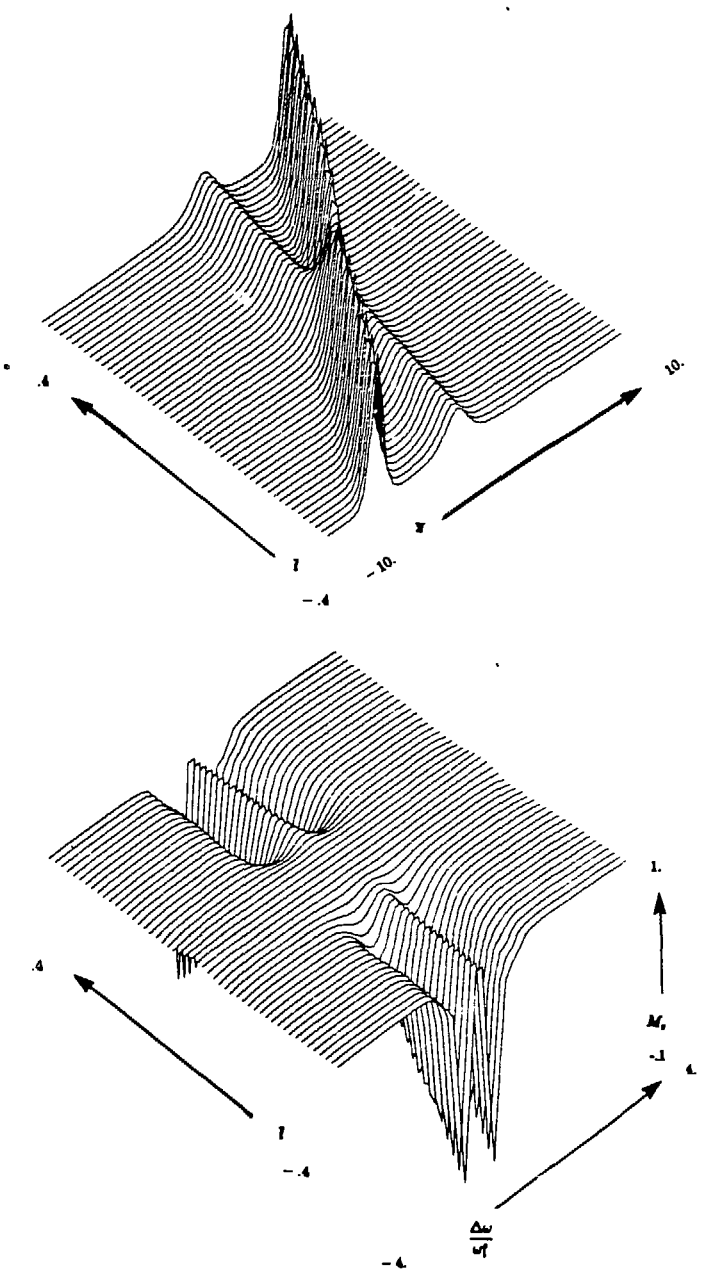

Figure 6.3: The case N=2. Each of the 50 wave profiles in the two soliton solution $V(\bar{x})$, $\bar{t}$=constant in the top plot is used as an amplitude modulated $\underline{6\pi}$ pulse in the bottom plot, where the z component of the magnetization is displayed as a function of $\frac{\Delta\omega}{\omega_1^o}$ after the pulse[51].

6(e) On a connection between the Bloch Equations and the KdV equation

Computer simulations have been a useful tool in developing rf temporal waveforms, by determining their performance in numerical integrations of the Bloch equations. In chapter 3, we described not only a specific input to the Bloch Transform (i.e., prolate spheroidals), but also an algorithm for computing the time development of the magnetization in the presence of time-varying rf magnetic fields. In this chapter, we have utilized that algorithm to compute what happens if we use N-soliton amplitude-modulated rf pulses. In this section, we will further explore the connection between the undamped Bloch equations and the KdV equation. By varying two parameters in the solution (6.19), we shall find a deep connection between solutions of the KdV equation and the Bloch equations.

One way of seeing the KdV phenomenon is to return to the derivation of V in (6.20) and (6.21). Observe that the pure soliton potential V depends in general on 2N parameters (the eigenvalues λ_i and the normalization constants b_i), while the energy levels depend only on λ_i. Hence, one obtains the N-parameter iso-spectral (i.e., constant eigenvalue) deformation of the KdV solution as the b_i move along $\bar{t}$ according to (6.5).

In the last section, we made a specific choice, namely λ_i=i and ϕ_i=0, to generate a particular solution of the KdV equation (6.1). As there is no *a priori* reason to make this choice (from which we obtained the V used in Figures 6.1-6.3), the eigenvalues λ_i would

appear to be unconstrained parameters. The justification for the choice λ_i=i for the KdV potential is based on the fact that these specific potentials have the property that

$$V(\bar{x},0) \;=\; N(N+1)\; sech^2(\bar{x}) \tag{6.27}$$

so that in view of (6.19), the $\bar{t}$=0 2π pulse is the miraculous pulse of self-induced transparency[41], and so produces the response $M_z \equiv$-1, as is seen in Figure 6.1 on page 80.

Having computed in (6.24) the N=2 soliton potential for arbitrary values of the λ_i, we next evaluate V allowing these values to vary. Starting from the Figures 6.4, 6.5, and 6.6, one is tempted to believe that the excited spin population can be moved around in the field of a linear main field gradient simply by changing the eigenvalues in the N=2 2π exitation pulse off of the special values λ_i=i (i=1,2). In particular, one is struck by the smooth excitation contours in these three Figures.

This suggests a method might be developed for simultaneously selecting multiple regions, which can be varied in position, for acquisition of chemical shift or image data. These data form a set similar to that obtained from coded aperature imaging. The image restoration process involves another inversion consisting of simple subtraction or reconstruction imaging[52].

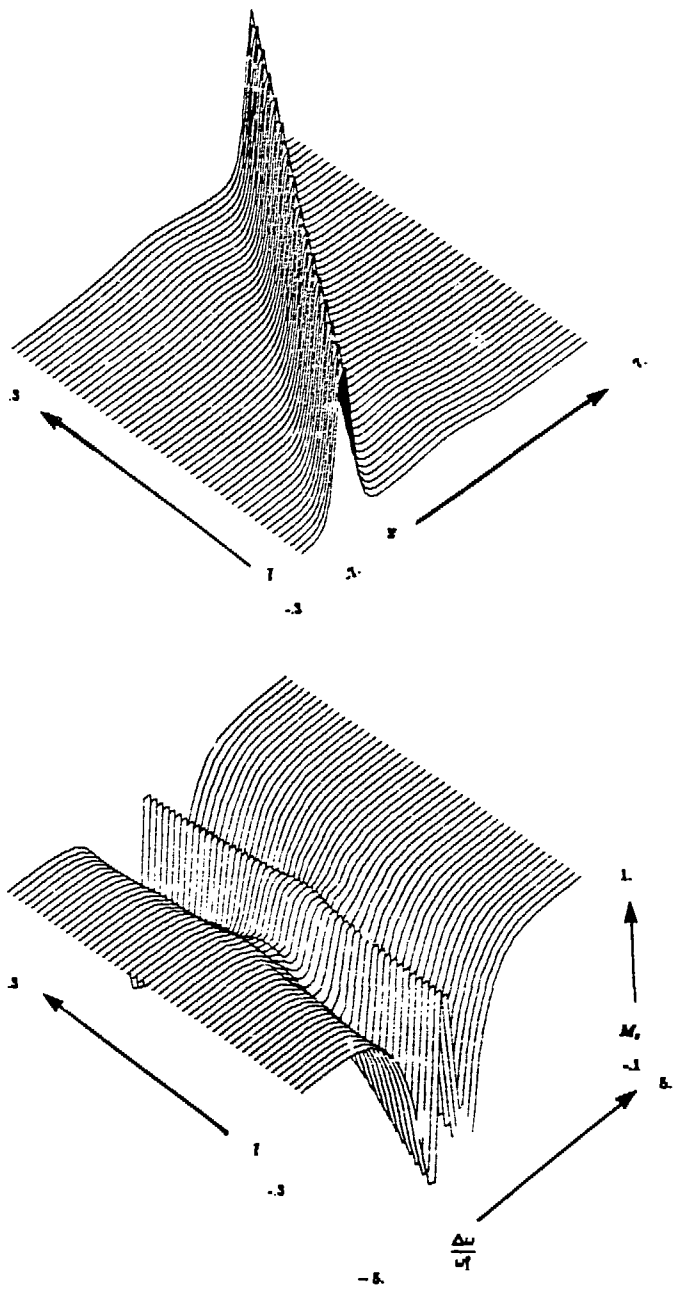

Figure 6.4: The case N=2. Each of the 50 wave profiles in the two soliton solution $V(\bar{x})$, $\bar{t}$=constant in the top plot is used as an amplitude modulated 2π pulse in the bottom plot, where the z component of the magnetization is displayed as a function of $\frac{\Delta\omega}{\omega_1^0}$ after the pulse. The eigenvalues for V in this case are λ_1=0.5 and λ_2=2. (Consult the Narrative on page 81)[53].

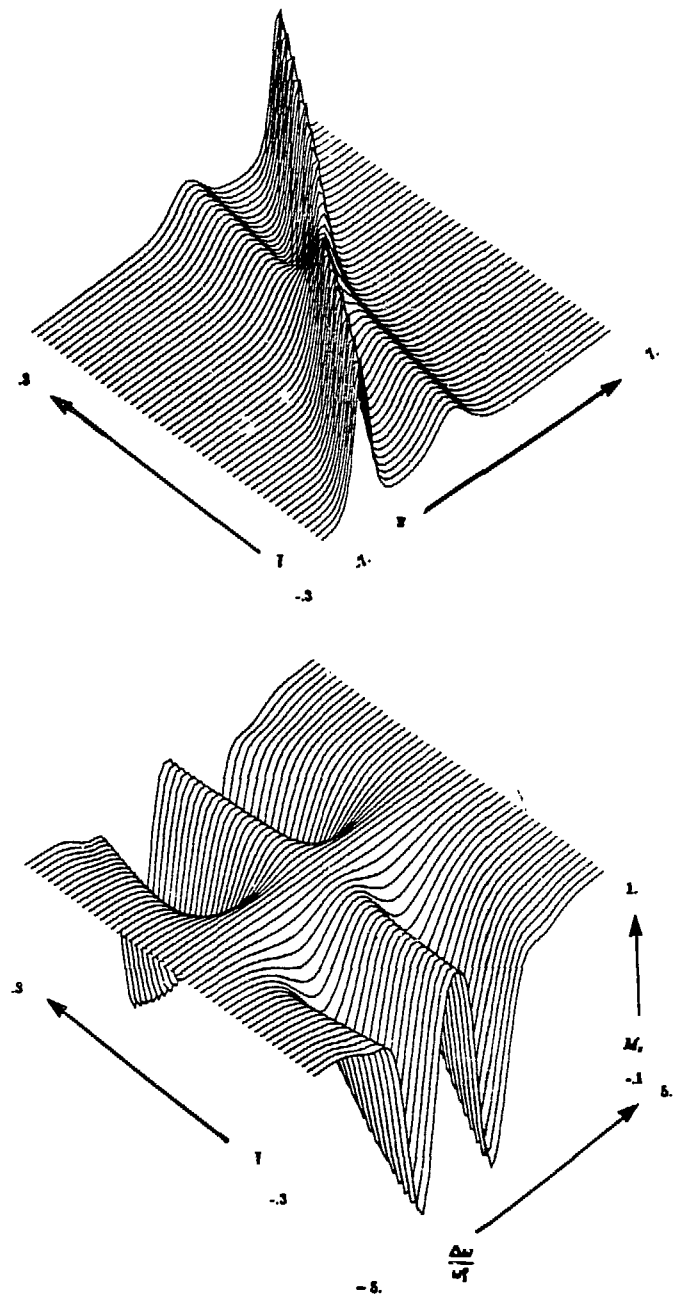

Figure 6.5: The case N=2. Each of the 50 wave profiles in the two soliton solution in the top plot is used as an amplitude modulated 2π pulse in the bottom plot, where the z component of the magnetization is displayed as a function of $\frac{\Delta\omega}{\omega_1^o}$ after the pulse. The eigenvalues for V in this case are λ_1=1 and λ_2=2[53].

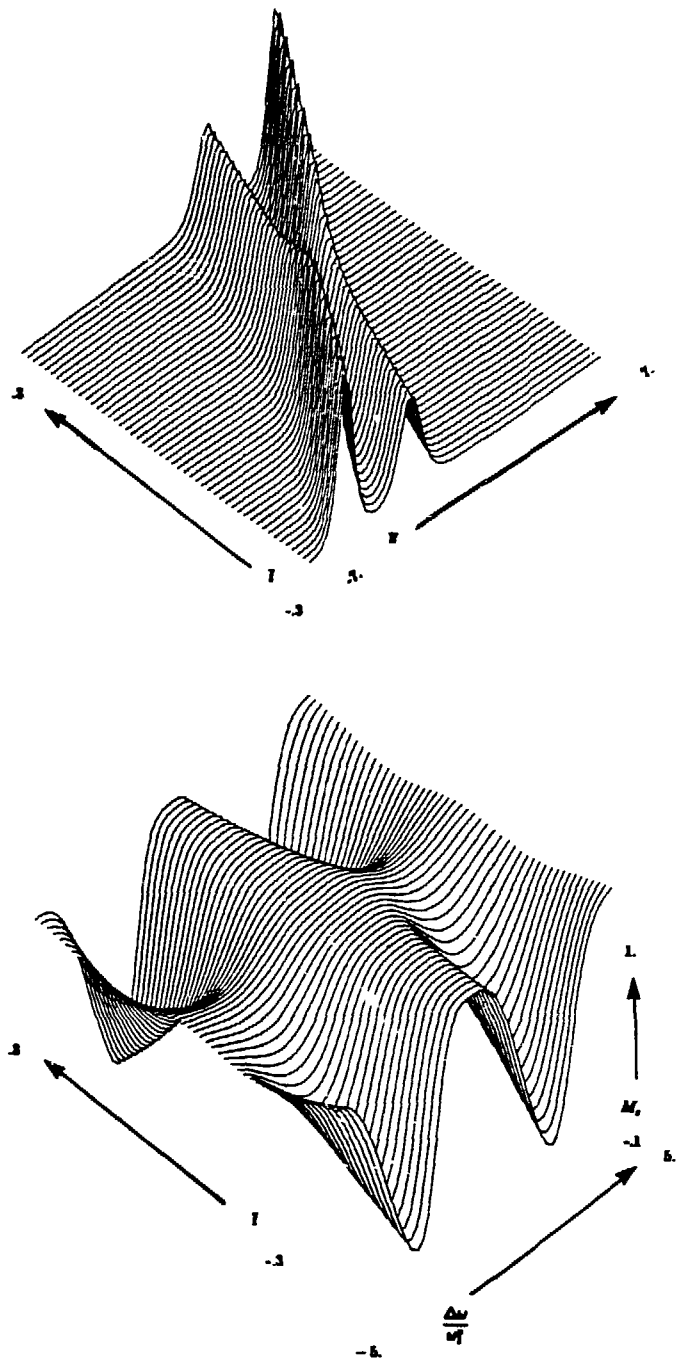

Figure 6.6: The case N=2. Each of the 50 wave profiles in the two soliton solution in the top plot is used as an amplitude modulated 2π pulse in the bottom plot, where the z component of the magnetization is displayed as a function of $\frac{\Delta\omega}{\omega_1^0}$ after the pulse. The eigenvalues for V in this case are λ_1=1.5 and λ_2=2[53].

This is indeed the case. In Figures 6.7-6.9, we show both numerical and experimental results that indicate one aspect of the special relationship between the Bloch equations and the KdV equation. In using the N=2 solutions of the KdV equation as 2π amplitude modulated rf pulses, we see from (6.24) that an apparent 2-parameter set of free variables in these solutions, at least as far as NMR amplitude modulations is concerned, is given by letting the λ_i float. Experimentally we find good agreement with these numerical results, and conclude that one can use these soliton amplitude modulations to reduce the nonlinear excitation problem to a linear geometric one, using the intersection of "planar" volumes perpendicular to the applied gradient in order to image a given spatial volume.

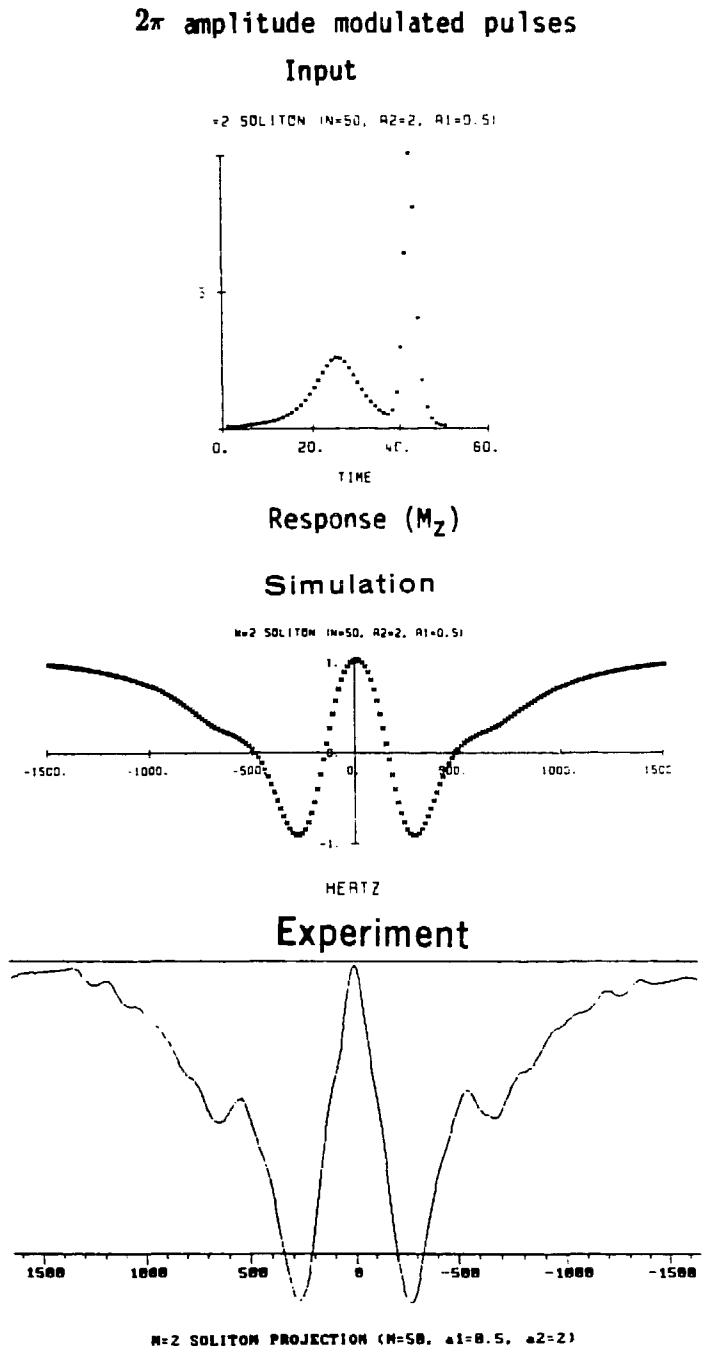

Figure 6.7: Experimental measurements and numerical simulations are compared. The comparison is read vertically as input followed by response. The larger eigenvalue λ_2 is kept constant, while the smaller eigenvalue λ_1 has the value 0.5[53]. In these three Figures 6.7-6.9, $a_i \equiv \lambda_i$.

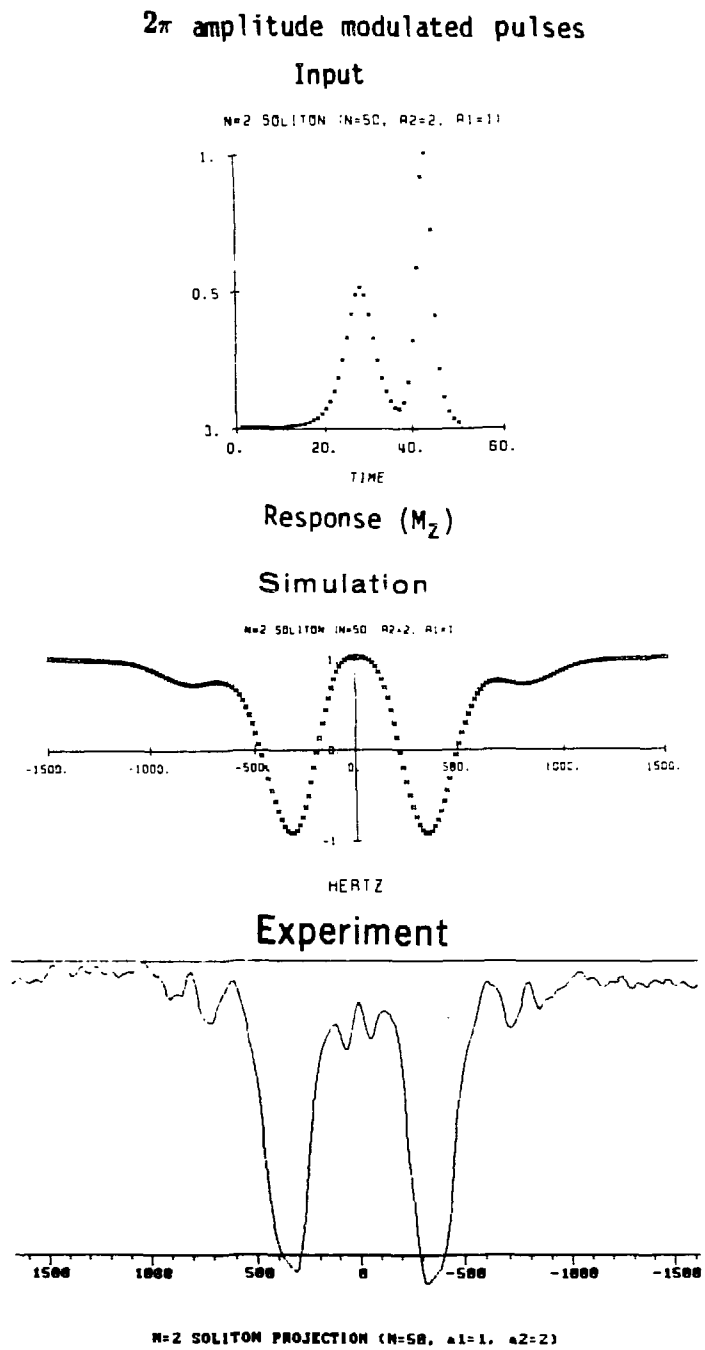

Figure 6.8: Experimental measurements and numerical simulations are again compared. The only difference with Figure 6.7 is the choice of the lower eigenvalue λ_1 for V, which is now 1[53].

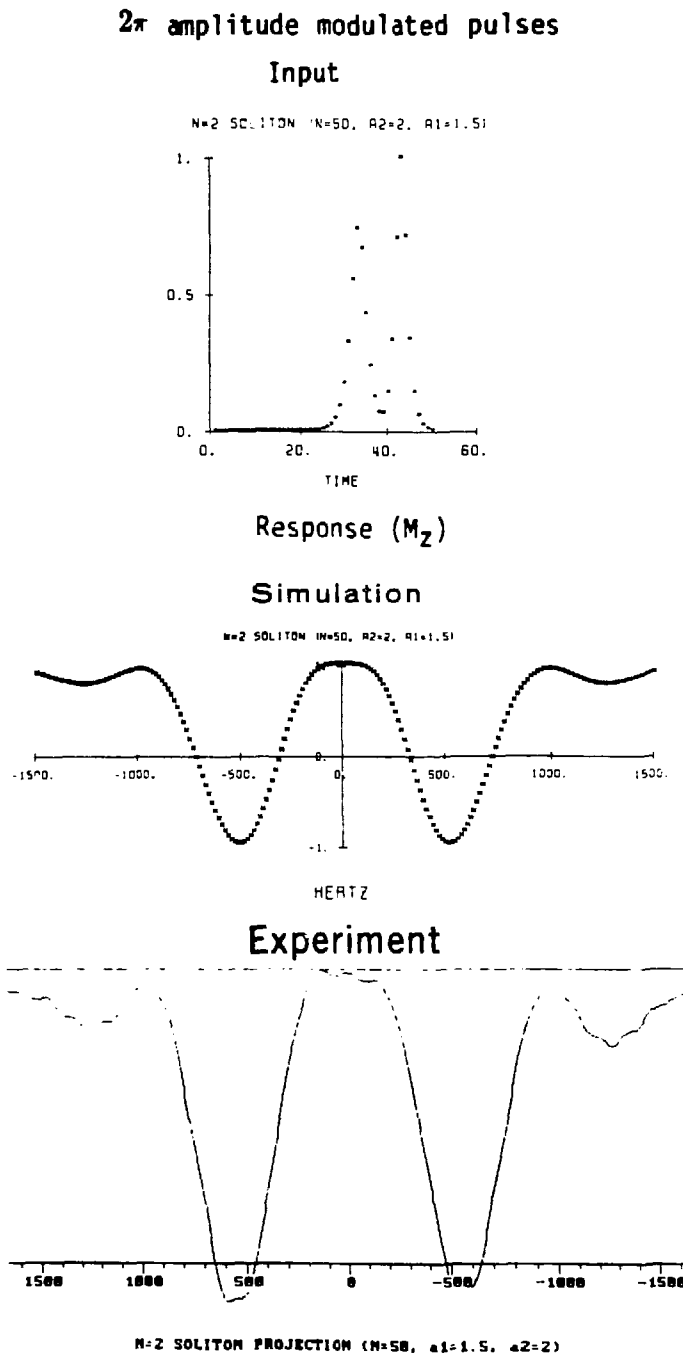

Figure 6.9: Experimental measurements and numerical simulations are again compared. The only difference with Figures 6.7 and 6.8 is the choice of the lower eigenvalue λ_1 for V, which is now set to 1.5[53].

We return to the first parametric variation (6.26), only now using the N=3 soliton solution (obtained using the procedure given in (6.20)-(6.25)). Explicitly, by choosing λ_i=i and again ϕ_i=0 (i=1,2,3), we find that

$$\begin{aligned} V_{up} = & \quad 180\cosh(6\bar{x}-72\bar{t}) + 480\cosh(4\bar{x}-208\bar{t}) + 120\cosh(8\bar{x}-224\bar{t}) \\ & + 1620\cosh(2\bar{x}-56\bar{t}) + 300\cosh(2\bar{x}-152\bar{t}) + 960\cosh(4\bar{x}-64\bar{t}) \\ & + 360\cosh(6\bar{x}-216\bar{t}) + 12\cosh(10\bar{x}-280\bar{t}) + 600\cosh(2\bar{x}-8\bar{t}) \\ & + 1512 \end{aligned} \tag{6.28}$$

and

$$V_{down} = \cosh(6\bar{x}-144\bar{t}) + 10\cosh(72\bar{t}) + 15\cosh(2\bar{x}-80\bar{t}) + 6\cosh(4\bar{x}-136\bar{t}) \tag{6.29}$$

so that

$$V(\bar{x},\bar{t}) = -60\frac{V_{up}}{V_{down}^2} \tag{6.30}$$

Exactly analogous to Figures 6.1-6.3, we show in Figures 6.10-6.12 the response obtained from 2π, 4π, and 6π N=3 soliton amplitude modulated rf pulses. We begin to see, by using these λ_i=i (i=1,...,N) solutions of the KdV equation as 2πN amplitude modulated rf pulses, a second feature of this connection between the KdV equation and rotations.

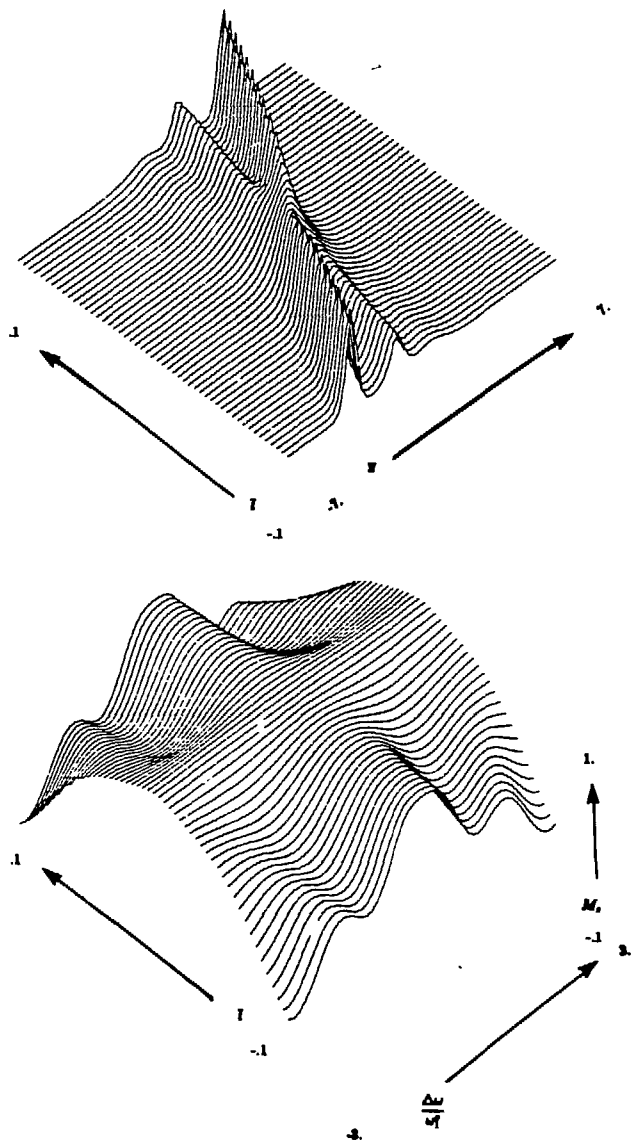

Figure 6.10: The case N=3. Each of the 50 wave profiles in the three soliton solution $V(\bar{x})$, $\bar{t}$=constant in the top plot is used as an amplitude modulated $\underline{2\pi}$ pulse in the bottom plot, where the z component of the magnetization is displayed as a function of $\frac{\Delta\omega}{\omega_1^o}$ after the pulse[53].

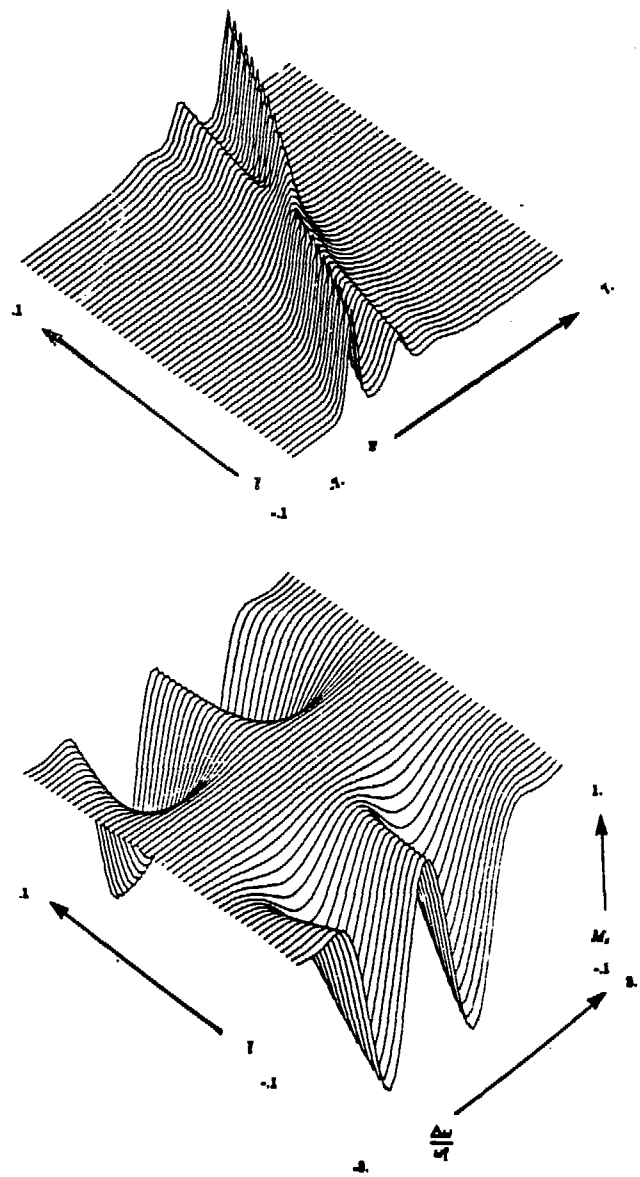

Figure 6.11: The case N=3. Each of the 50 wave profiles in the three soliton solution $V(\bar{x})$, $\bar{t}$=constant in the top plot is used as an amplitude modulated $\underline{4\pi}$ pulse in the bottom plot, where the z component of the magnetization is displayed as a function of $\frac{\Delta\omega}{\omega_1^o}$ after the pulse[53].

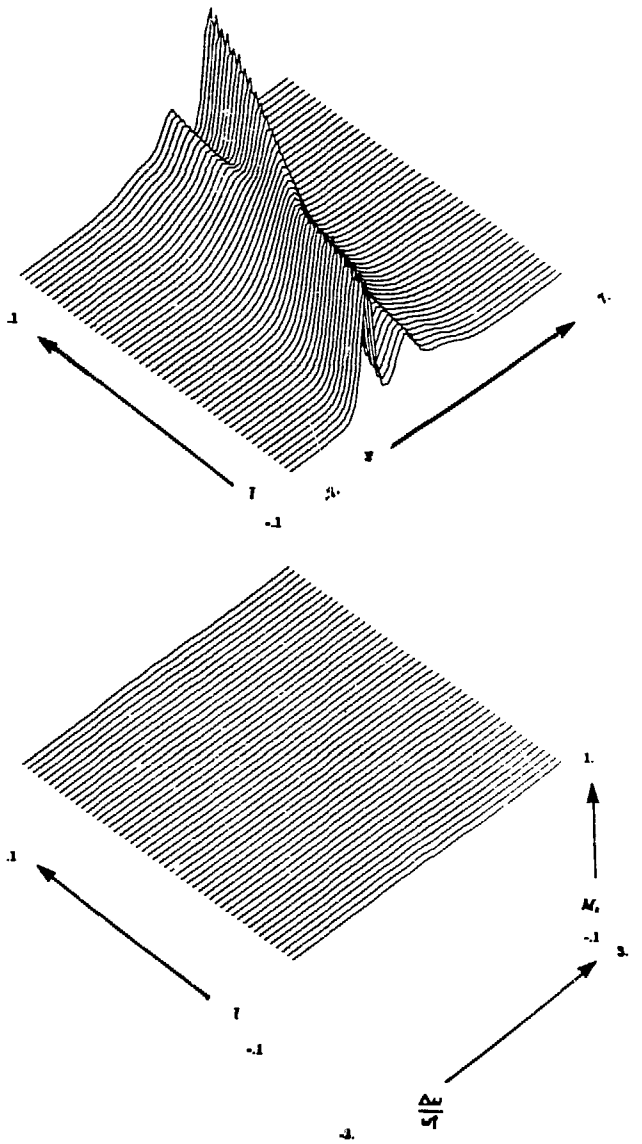

Figure 6.12: The case N=3. Each of the 50 wave profiles in the three soliton solution $V(\bar{x})$, $\bar{t}$=constant in the top plot is used as an amplitude modulated $\underline{6\pi}$ pulse in the bottom plot, where the z component of the magnetization is displayed as a function of $\frac{\Delta\omega}{\omega_1^o}$ after the pulse[53].

In case you have any doubts about all this, we continue with the N=4 soliton potential. A laborious computation [1] yields

$$
\begin{aligned}
V_{up} = \; & 980\cosh(18\bar{x}-792\bar{t}) + 17640\cosh(16\bar{x}-736\bar{t}) \\
& + 61740\cosh(14\bar{x}-584\bar{t}) + 88200\cosh(14\bar{x}-728\bar{t}) \\
& + 548800\cosh(12\bar{x}-576\bar{t}) + 54880\cosh(12\bar{x}-288\bar{t}) \\
& + 196000\cosh(12\bar{x}-720\bar{t}) + 326200\cosh(10\bar{x}-280\bar{t}) \\
& + 326200\cosh(10\bar{x}-520\bar{t}) + 1543500\cosh(10\bar{x}-568\bar{t}) \\
& + 220500\cosh(10\bar{x}-664\bar{t}) + 1234800\cosh(8\bar{x}-224\bar{t}) \\
& + 3322480\cosh(8\bar{x}-512\bar{t}) + 112000\cosh(8\bar{x}-272\bar{t}) \\
& + 480200\cosh(6\bar{x}-72\bar{t}) + 5078640\cosh(6\bar{x}-216\bar{t}) \\
& + 283500\cosh(6\bar{x}-456\bar{t}) + 1200500\cosh(6\bar{x}-360\bar{t}) \\
& + 1715000\cosh(6\bar{x}-504\bar{t}) + 2242240\cosh(4\bar{x}-64\bar{t}) \\
& + 12348000\cosh(4\bar{x}-160\bar{t}) + 2609600\cosh(4\bar{x}-208\bar{t}) \\
& + 196000\cosh(4\bar{x}-304\bar{t}) + 2609600\cosh(4\bar{x}-448\bar{t}) \\
& + 24500\cosh(2\bar{x}+232\bar{t}) + 16420880\cosh(2\bar{x}-8\bar{t}) \\
& + 2283400\cosh(2\bar{x}-56\bar{t}) + 15435000\cosh(2\bar{x}-152\bar{t}) \\
& + 2283400\cosh(2\bar{x}-296\bar{t}) + 1543500\cosh(2\bar{x}-440\bar{t}) \\
& + 2401000\cosh(288\bar{t}) + 5488000\cosh(144\bar{t}) \\
& + 15934800
\end{aligned}
\tag{6.31}
$$

[1] Impossible without the help of vaxima, the Vax version of the symbolic manipulation program MACSYMA!

and

$$
\begin{aligned}
V_{down} = \; & 7\cosh(10\bar{x} - 400\bar{t}) \;\; + 70\cosh(8\bar{x} - 392\bar{t}) \\
& + 315\cosh(6\bar{x} - 336\bar{t}) \;\; + 490\cosh(4\bar{x} - 184\bar{t}) \\
& + 245\cosh(2\bar{x} + 112\bar{t}) \;\; + 350\cosh(4\bar{x} - 328\bar{t}) \\
& + 1225\cosh(2\bar{x} - 176\bar{t}) + 50\cosh(120\bar{t})
\end{aligned}
\tag{6.14}
$$

so that

$$
V(\bar{x}, \bar{t}) = -4200\frac{V_{up}}{V_{down}^2} \tag{6.15}
$$

This time we will skip all the 2πk (k=1,2,3) pulses, and just show in Figure 6.13 the N=4 8π amplitude modulation.[2] In case you can't see 4 solitons in the top plot in Figure 6.13, we compute the N=4 solution out to a longer time ($\bar{t} = \pm .1$) in Figure 6.14. I hope we all agree now that the $\underline{2\pi N}$ amplitude modulation (6.19) is the proper NMR generalization of the 2π hyperbolic secant pulse of self-induced transparency[41].

[2]The N=3 and N=4 soliton evaluations were performed on a Cray X-MP computer, thanks to helpful assistance from Ron Huesman and Bernard Mazoyer.

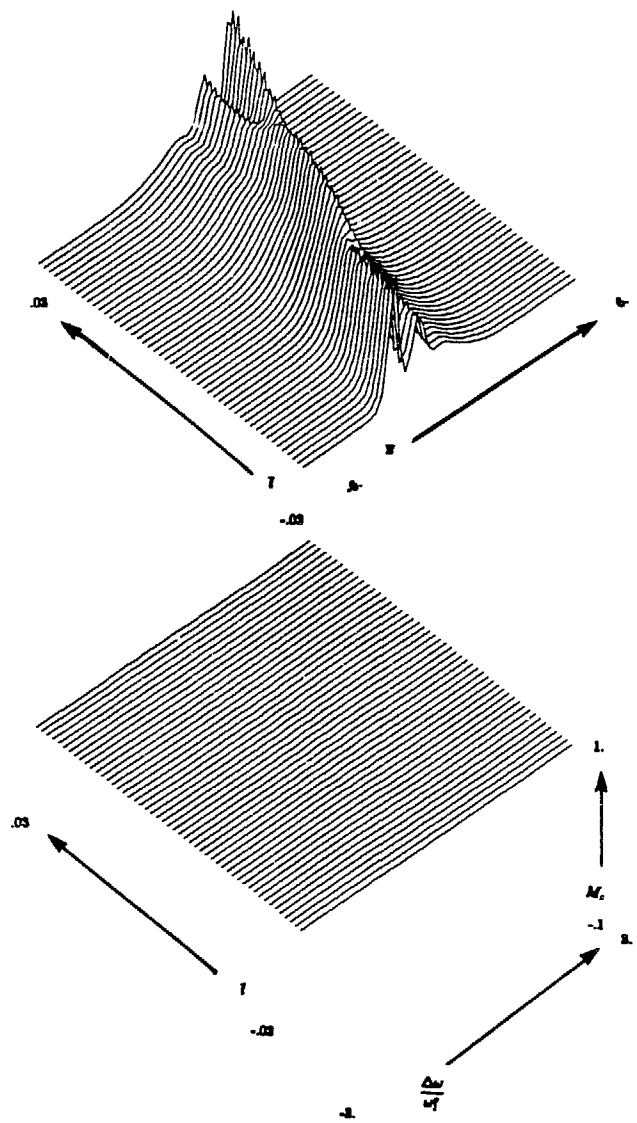

Figure 6.13: The case N=4. Each of the 50 wave profiles in the four soliton solution $V(\bar{x})$, $\bar{t}$=constant in the top plot is used as an amplitude modulated $\underline{8\pi}$ pulse in the bottom plot, where the z component of the magnetization is displayed as a function of $\frac{\Delta\omega}{\omega_1^o}$ after the pulse.

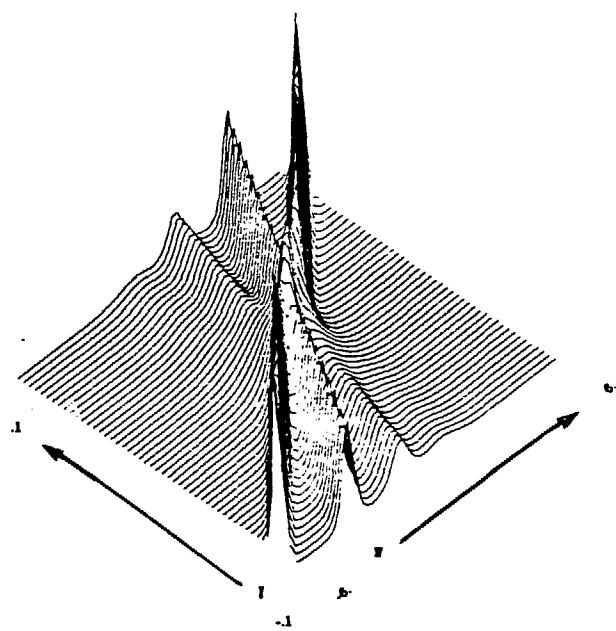

Figure 6.14: The case N=4. Each of the 50 wave profiles in the four soliton solution $V(\bar{x})$, $\bar{t}$=constant is computed out to a longer (KdV) time $\bar{t} = \pm .1$. One clearly sees four solitons.

6(f) (Soliton) reflections

In trying to understand the KdV-Bloch connection, some recent discoveries have been made. In particular, one of these discoveries will now be described in detail, since it will not only resolve some of the difficulties apparent in the previous sections of this chapter, but can also *a posteriori* help everyone understand how the connection was made in the first place. For this, I have to thank all of those who were willing to lend a critical ear to my exhortations in the past few months.

Let us recall the goal. We would like to find an inverse for the Bloch Transform $\mathcal{B}$, since we would then be able to specify the necessary temporal rf pulse profile to achieve a given final magnetization profile versus resonance offset, and hence, via rotating frame arguments, spatial position. In trying to find a suitable candidate for $\mathcal{B}^{-1}$, and simultaneously answering the question of why the linear theory worked so well (see chapter 3) for this nonlinear map $\mathcal{B}$, a way of rewriting the Bloch equations in second order form (similar, by replacing t with $\bar{z}$, to a "time-independent" Schrödinger equation) appeared. At this point, the KdV-Schrödinger connection became visible, as well as the hope of using this scheme to invert $\mathcal{B}$.

A second consideration was the remarkable fact about the 2π hyperbolic secant pulse of self-induced transparency[41], and so eventhough one should really solve the Riccati equation implied in (6.15) to get ω_1 from V, one really wants to neglect the imaginary part of V because of (6.27). Moreover, neglecting the imaginary part of V side-steps the issue

of complex potentials, and so non-conservation of probability, and all that this implies (a point we shall soon return to).

The crucial observation is that one should be looking at $\frac{\dot{g}}{g}$, not g, for t large in (6.17).[3] Therefore, on the one hand

$$\frac{\dot{g}}{g} \sim -i\frac{\Delta\omega}{2}\phi\,(-1)^k \tag{6.34}$$

(for ω_1 a 2πk pulse), but also, from (6.16), one has that

$$\frac{\dot{g}}{g} \sim -i\lambda\frac{ae^{-i\lambda t} - be^{i\lambda t}}{ae^{-i\lambda t} + be^{i\lambda t}} \tag{6.35}$$

Hence, using the definition of ϕ in (6.10),

$$\phi = \frac{M_x + iM_y}{M_z - 1} \sim \frac{ae^{-i\lambda t} - be^{i\lambda t}}{ae^{-i\lambda t} + be^{i\lambda t}} \tag{6.36}$$

and so one really can write the reflection and transmission coefficients in terms of $\mathbf{M}(\Delta\omega,\mathrm{T})$.

A moment's reflection reveals that, for large t, the magnetization components obey

$$\begin{aligned} M_x(t) &= \tfrac{m_x}{2}\left(e^{i(2\lambda t+\alpha)} + e^{-i(2\lambda t+\alpha)}\right) \\ M_y(t) &= \tfrac{m_y}{2i}\left(e^{i(2\lambda t+\alpha)} - e^{-i(2\lambda t+\alpha)}\right) \\ M_z(t) &= m_z \end{aligned} \tag{6.37}$$

for arbitrary phase factor α. Thus using (6.36)

$$\begin{aligned} \phi &\sim \frac{m_x + \frac{m_y}{2}\left(e^{i(2\lambda t+\alpha)} - e^{-i(2\lambda t+\alpha)}\right)}{\frac{m_x}{2}\left(e^{i(2\lambda t+\alpha)} + e^{-i(2\lambda t+\alpha)}\right) - 1} \\ &\sim \frac{ae^{-i\lambda t} - be^{i\lambda t}}{ae^{-i\lambda t} + be^{i\lambda t}} \end{aligned} \tag{6.38}$$

---

[3] I acknowledge E.H. Wichmann for this observation.

Cross-multiplying and identifying terms, one obtains the following set of six consistency relations

$$\begin{aligned} \tfrac{m_y}{2} b &= -\tfrac{m_x}{2} b \\ \tfrac{m_y}{2} a &= \tfrac{m_x}{2} a \\ m_z b &= b \\ m_z a &= -a \\ -\tfrac{m_y}{2} b &= -\tfrac{m_x}{2} b \\ -\tfrac{m_y}{2} a &= \tfrac{m_x}{2} a \end{aligned} \tag{6.39}$$

Moreover, equation (6.9) must also be obeyed.

There are thus only two consistent cases.

<u>case 1</u> a $\equiv$ 0 and $m_z = M_z = 1$

<u>case 2</u> b $\equiv$ 0 and $m_z = M_z = -1$

We deal with each of these cases in turn.

Case 1 corresponds to a "super-radiant" potential in the scattering problem above (see (6.16)), physically allowed when V is complex. Yet we can eliminate this possibility quite easily without having to consider such complex V. Recall that in the rotating frame Bloch equations (2.24), the motion of the magnetization is a precession about the effective applied field. In case 1, the initial condition M_z=-1 evolves into M_z=+1 (infinite population inversion bandwidth). However, this is inadmissable for very large values of $\Delta\omega$, since both

the effective magnetic field and the magnetization **M** point along the z direction, and so the precession is trivial. We can therefore dismiss case 1 as unphysical.

For case 2, we have exactly the $\underline{2\pi N}$ pulses previously considered. Miraculous as this case is, it is now even more so, given that this entire formulation can only work in this case.

This computation serves to close the book on this inverse scattering approach to inverting $\mathcal{B}$. One is simply unable to invert $\mathcal{B}$ in general this way. However, it still does not destroy the author's, and many other people's, conviction that an inverse for $\mathcal{B}$ exists somewhere. Yet these soliton reflectionless potentials have cleared up the special behavior observed in self-induced transparency, and in providing an infinite number (the N of 2πN) of an infinite number ($| \bar{t} | \leq \epsilon$) of pulse profiles, have demonstrated that, at least in one case, albeit perhaps a useless one for medical imaging purposes, one can indeed invert $\mathcal{B}$. Specifically, if one asks that the spins return to equilibrium after the pulse independent of resonance offset, one can invert $\mathcal{B}$ in this particular case to find the 2πN pulses developed here.

7. Conclusion

> *"The miracle of the appropriateness of the language of mathematics for the formulation of the laws of physics is a wonderful gift we neither understand nor deserve."*
>
> E.P. Wigner

The theoretical analysis in the preceeding chapters has been confirmed experimentally on the 0.5 Tesla IBM/Oxford Imaging Spectrometer at the LBL NMR Imaging Facility. As the true worth of a theorist's ideas (at least in physics) is in their experimental reality, we have been fortunate indeed to have considered a simple physical system, namely that of isolated spins in applied magnetic fields. Nevertheless, the quatum nature of these spins is a nonlinear one, and so the problem is difficult. We have further been fortunate to have had a series of (divine?) inspirations conspire to demonsrate the feasibility of reaching our goal of localized NMR measurements. But a difficult problem still remains, that of taking the demonstrated principles here and implementing them in a concrete medical imaging situation.

On another level, Wigner's words above well describe the findings in this thesis. We

began by asking the question:

1. What are the nuclear spins doing?

In answer to that question, we found that the Bloch equations are the fundamental laws governing the behavior of nuclear spins in applied magnetic fields. But we are particularly interested in a prescribed set of magnetic fields (namely those in current NMR biomedical imagers), and wish to achieve sharply localized spin excitation.

However, the Bloch equations, when viewed as a transformation from rf input to magnetization response, are a nonlinear mapping. One manifestation of this nonlinearity is easily visualized as follows, by considering the following four experiments:

(a) Perform a simple one pulse experiment, calibrating the pulse duration to yield the maximum signal output (a 90° pulse).

(b) Double the energy in the pulse (a 180° pulse). No signal!!

(c) Triple the energy in (a) (a 270° pulse). Again a maximum signal, but 180° degrees out of phase with the signal detected in (a).

(d) Quadruple the energy in (a) (a 2π pulse). No signal again!

The quantum-mechanical explanation is in terms of coherence[54], and in hindsight our problem really concerns a basic question in quantum mechanics. This question is the one of preparation of desired excited spin states. It is a happy accident that we are able to visualize this problem in terms of the trajectory of a classical vector **M** on the sphere

S^2; and so in trying to find the nonlinear modes of (localized) rf excitation in biomedical NMR, it is no accident that we arrived at a set of linear modes with connections to the Uncertainty Principle[14] and nonlinear modes having many physical manifestations[48].

By formulating the Bloch transform, and hueristically solving by finding two sets of rf field temporal modulations (prolate spheroidal wave functions) that did the job so well, we arrived at a second, deeper question:

2. Given that the Bloch Transform is a nonlinear transformation, why did the linear theory (i.e., pswf) work so well?

An exploration of the invertibility of the Bloch Transform yielded even more spectacular results. At this step, we attempted to find an inverse for the Bloch Transform by reformulating the problem as a inverse scattering problem in one-dimensional quantum mechanics. The special solution found here, the N-soliton pulses, have some remarkable properties as rf temporal modulations, and given their amazing behavior in a similar problem in coherent optics[41,55], one is tempted to say that we have reached a deeper level. Yet an inverse for the Bloch Transform still does not exist!

The analogy here to the stumbling drunk - who drops his key on the way home in the dark and searches under the lamppost to find it (it is the only possible place to look!) - is unavoidable. Indeed, in stumbling upon this miracle, I am still in awe. Inspired by recent results[56] showing a connection between the pswf and the KdV soliton family, we are left with a final question:

3. What is the connection between KdV, pswf, and the Bloch equations (BE)?,

   or what is the nature of the commutativity of the diagram below?

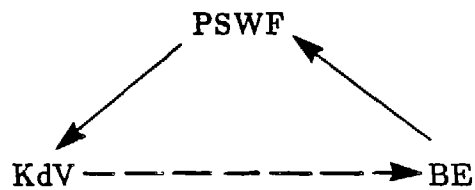

Simultaneous to these theoretical developments, we have had the pleasure of experimentally realizing some of these results (in collaboration with M. Robin Bendall at Oxford Research Systems, Mirko Hrovat at M.I.T./ Francis Bitter Magnet Lab, and at the LBL NMR Imaging Facility). NMR is an experimental science, and it has been quite an education getting the spectrometer to behave like the equations in my books. It would not have been possible without the able assistance of Mark Roos.

I cannot close without a tribute to my advisor, Alberto Grünbaum. He is truly a giant of computation, capable of finding "good" mathematics almost anywhere. It is a credit to his practical genius that he chose medical imaging in which to find prolate spheroidal wave functions, KdV solitons, and other such miraculous creatures.

References

1. F. Bloch, *Phys. Rev.* **70**, 460 (1948).

2. L.E. Crooks, *IEEE Trans. Nucl. Sci.* **NS-27** (5), 1239 (1980).

3. D.I. Hoult, *J. Magn. Reson.* **35**, 69 (1979).

4. D. Slepian, *SIAM Review* **25**, 379 (1983).

5. A. Abragam, The Principles of Nuclear Magnetism, (Oxford University Press, London, 1961).

6. C.P. Slichter, Principles of Magnetic Resonance, second ed., (Springer-Verlag, New York, 1980).

7. L.D. Landau and E.M. Lifshitz, Mechanics, third ed., (Pergamon Press, New York, 1976).

8. P. Mansfield and P.G. Morris, NMR Imaging in Biomedicine, (Academic Press, New York, 1982).

9. I.I. Rabi, N.F. Ramsey, and J. Schwinger, *Rev. Mod. Phys.* **26** (2), 167 (1954).

10. W. Hinshaw and A. Lent, *Proc. IEEE* **71** (3), 175 (1983).

11. R. Gilmore, Lie Groups, Lie Algebras, and Some of Their Applications, (John Wiley, New York, 1974).

12. H.J. Landau, "An Overview of Time and Frequency Limiting", presented at Conference on Fourier Techniques and Applications, (University of New South Wales, Sydney, Australia, September, 1983).

13. D. Slepian and H.O. Pollak, *Bell Sys. Tech. J.* **40**, 43 (1961).

14. H.J. Landau and H.O. Pollak, *Bell Sys. Tech. J.* **40**, 65 (1961).

15. ___, *Bell Sys. Tech. J.* **41**, 1295 (1962).

16. D. Slepian, *Bell Sys. Tech. J.* **43**, 3009 (1964).

17. H. Bowdler, R.S. Martin, C. Reinsch, and J.H. Wilkinson, *Numer. Math.* **11**, 293 (1968).

18. F.A. Grünbaum, *Inverse Problems* **1** (3), L25 (1985).

19. D. Slepian, *Bell Sys. Tech. J.* **57**, 1371 (1978).

20. A. Hasenfeld, "SHARP NMR Biomedical Spatial Localization", *Magnetic Resonance in Medicine* **2** (5), 505 (1985).

21. F.A. Grünbaum, L. Longhi, and M. Perlstadt, *SIAM J. Appl. Math.* **42** (5), 941 (1982).

22. H. Dym and H.P. McKean, Fourier Series and Integrals, (Academic Press, New York, 1972).

23. C. Bauer, R. Freeman, T. Frenkiel, J. Keeler, and A.J. Shaka, *J. Magn. Reson.* **58**, 442 (1984).

24. D.W. Marquardt, *J. Soc. Indust. Appl. Math.* **11** (2), 431 (1963).

25. D.I. Hoult and R.E. Richards, *J. Magn. Reson.* **24**, 71 (1976).

26. J.D. Jackson, Classical Electrodynamics, second ed., (John Wiley, New York, 1975).

27. E.M. Purcell, Electricity and Magnetism, Berkeley Physics Course - Vol. 2, (McGraw-Hill, New York, 1963).

28. I. Stakgold, Green's Functions and Boundary Value Problems, (John Wiley, New York, 1979).

29. W.R. Smythe, Static and Dynamic Electricity, (McGraw-Hill, New York, 1939), p. 267.

30. J.L. Evelhoch, M.C. Crowley, and J.J.H. Ackerman, *J. Magn. Reson.* **56**, 110 (1984).

31. A. Haase, W. Hänicke, and J. Frahm, *J. Magn. Reson.* **56**, 401 (1984).

32. P. Eberhard, *Group A Physics Note No. 923*, Lawrence Berkeley Laboratory, Berkeley, California (1981).

33. M.R. Bendall and R.E. Gordon, *J. Magn. Reson.* **53**, 365 (1983).

34. R. Tycko and A. Pines, *J. Magn. Reson.* **60**, 156 (1984).

35. M.R. Bendall, *J. Magn. Reson.* **60**, *** (1984).

36. M.S. Roos, A. Hasenfeld, M.R. Bendall, and R.J. Ordidge, "Spatial Sensitivity for Multiple Pulse Sequences in Inhomogeneous B_1 Fields", ongoing collaboration.

37. R.J. Ordidge, M.R. Bendall, R.E. Gordon, and A. Conelly, *Eleventh Biennial International Conference of Magnetic Resonance in Biological Systems*, (Goa, Septembe 1984), Proceedings in press.

38. M.R. Bendall and D.T. Pegg, submitted to *Magn. Reson. in Med.*.

39. M.R. Bendall, in Biomedical Magnetic Resonance, A.R. Margulis and T.L. James, Eds., (Radiology Research and Education Foundation, San Francisco, 1984).

40. S. Novikov, S.V. Manakov, L.P. Pitaevskii, and V.E. Zakharov, Theory of Solitons, (Plenum, New York, 1984).

41. S.L. McCall and E.L. Hahn, *Phys. Rev.* **183**, 457 (1969).

42. G.L. Lamb, *Phys. Rev. A* **9** (1), 422 (1974).

43. F. Calogero and A. Degasperis, Spectral Transform and Solitons I, (Amsterdam, North-Holland, 1982).

44. M.J. Ablowitz and H. Segur, Solitons and the Inverse Scattering Tranform, (SIAM Studies in Applied Mathematics, Philadelphia, 1981).

45. A.C. Newell, Solitons in Mathematics and Physics, (SIAM, Philadelphia, 1985).

46. M.S. Silver, R.I. Joseph, and D.I. Hoult, *Phys. Rev. A* **31** (4), 2753 (1985).

47. G. Darboux, *Comptes Rendus.* **94**, 1456 (1882).

48. G.L. Lamb, Elements of Soliton Theory, (John Wiley, New York, 1980).

49. P. Deift and E. Trubowitz, *Comm. Pure and Appl. Math.* **17**, 121 (1979).

50. V. Bargmann, *Rev. Mod. Phys.* **21**, 488 (1949).

51. F.A. Grünbaum and A. Hasenfeld, "An Exploration of the Invertibility of the Bloch Transform", *Inverse Problems*, in press.

52. T.F. Budinger, *SPIE* **314**, 9 (1981).

53. A. Hasenfeld, "On a Connection Between the Bloch Equations and the KdV Equation", submitted to *J. Magn. Reson.*

54. R.H. Dicke, *Phys. Rev.* **93**, 99 (1954).

55. D.W. Dolfi and E.L. Hahn, *Phys. Rev. A* **21** (4), 1272 (1980).

56. J.J. Duistermaat and F.A. Grünbaum, "Differential Equations in the Spectral Parameter", *Comm. Math. Phys.*, in press.

To my Chinese friends, for providing a much needed diversion.

To Maire McAuliffe, David Johnson, Betsy Wood, and Lu, for keeping me alive.

This work was supported in part by the Director, Office of Energy Research, Office of Health and Environmental Research of the US Department of Energy under contract No DE-AC03-76SF00098 and in part by Public Health Service Grant No HL25840 awarded by the National Heart Lung and Blood Institute, Department of Health and Human Services.